



Dissertation



Beam-Preparation with REXTRAP for the REX-ISOLDE Experiment

ausgeführt zum Zwecke der Erlangung des akademischen Grades eines
Doktors der technischen Wissenschaften unter der Leitung von

Ao. Univ. Prof. Dr. phil. Heinz Oberhummer
Institut Nr. 141
Atominstitut der österreichischen Universitäten

eingereicht an der Technischen Universität Wien
Fakultät für Technische Naturwissenschaften und Informatik

von

Dipl. Ing. Oliver Forstner
Matr. Nr. 9225151
11, ch. Perrault-de-Jotemps, CH-1217 Meyrin

Meyrin, im August 2001

Dipl. Ing. Oliver Forstner

CERN-THESIS-2001-018
10/09/2001



Zusammenfassung

REX-ISOLDE ist ein Nachbeschleuniger für radioaktive Ionen an der ISOLDE Anlage am CERN. Seine Aufgabe besteht darin, die von dem on-line Massenseparator ISOLDE kommenden radioaktiven Ionen von 60 keV auf eine Endenergie von 2,2 MeV/u zu beschleunigen. Um dieses Ziel mit einem möglichst kompakten und kosteneffizienten Aufbau zu erreichen, wurde ein neuartiges Konzept vorgeschlagen. Die Ionen werden zuerst in einer Penningfalle (REXTRAP) gesammelt. Von dort werden sie zu einer EBIS (**E**lectron **B**eam **I**on **S**ource) transportiert, in welcher der Ladungszustand der Ionen erhöht wird. Aufgrund der hohen Ladungszustände der Ionen kann der nachfolgende Linearbeschleuniger vergleichsweise kompakt aufgebaut werden. Im Rahmen dieser Arbeit wird der Aufbau und die Inbetriebnahme von REXTRAP beschrieben. REXTRAP ist eine große, mit Puffergas gefüllte Penningfalle, deren Aufgabe darin besteht, den von ISOLDE kommenden Strahl von radioaktiven Ionen zu speichern und dessen Eigenschaften dahingehend zu verbessern, um ihn danach in die REXEBIS einschließen zu können. Nach einer Auflistung der mit REX-ISOLDE zu erforschenden Gebiete der Kernphysik sowie einer Beschreibung der einzelnen Komponenten von REX-ISOLDE, wird die Theorie der Penningfalle sowie der Aufbau von REXTRAP erläutert. Zum Abschluß werden die Ergebnisse der Tests von REXTRAP präsentiert und erörtert, ob REXTRAP im momentanen Aufbau die Anforderungen erfüllen kann, die für den Betrieb innerhalb von REX-ISOLDE erforderlich sind.

Abstract

REX-ISOLDE is a post-accelerator for radioactive ions located at the ISOLDE facility at CERN. Its task is to accelerate the radioactive ions coming from the on-line mass separator ISOLDE from 60 keV to a final energy of 2.2 MeV/u. To achieve this goal with a compact and cost-efficient setup a new concept was proposed. First the ions are accumulated in a Penning trap (REXTRAP), then the ions are transported to an EBIS (**E**lectron **B**eam **I**on **S**ource), where their charge-state will be increased. Due to the high charge-state of the ions the following linear accelerator can be built comparatively compactly. In the framework of this thesis the construction and commissioning phase of REXTRAP is described. REXTRAP is a large, gas-filled Penning trap whose aim is to store and cool the radioactive ions coming from ISOLDE. After listing the physics motivation for building REX-ISOLDE and describing its elements, the theory of a Penning trap as well as the setup of REXTRAP is explained. Finally test results for REXTRAP are presented followed by a discussion on how REXTRAP in the present setup can fulfill the demands for the operation of REX-ISOLDE.

Table of Contents

List of Figures	v
List of Tables	ix
Introduction	1
1 Physics Motivation	3
1.1 Nuclear Structure Investigation	4
1.1.1 Neutron-Rich Nuclei Close to the Semi-Magic Shells of N=20 and 28	4
1.1.2 Study of Light Neutron-Rich Nuclei	5
1.2 Nuclear Astrophysics	6
1.2.1 Nucleosynthesis and the rp-Process	6
1.2.2 Stellar Burning and the Solar Neutrino Puzzle	7
1.3 Nuclear Solid State Physics	7
1.4 'Low energy' Experiments	8
1.4.1 Weak-Interaction Studies with WITCH	8
1.4.2 Conversion Electron Spectroscopy Inside REXTRAP	9
2 The Elements of REX-ISOLDE	11
2.1 Overview	11
2.2 ISOLDE	13
2.3 REXTRAP	14
2.4 REX-EBIS	15
2.5 Mass-Separator	16
2.6 REX-LINAC	17
2.6.1 4-rod RFQ	17
2.6.2 The Matching Section	19
2.6.3 IH-Structure	20
2.6.4 7-Gap Resonators	22
2.7 Target and Detectors	23
2.7.1 The Parallel Plate Avalanche Counter	24
2.7.2 Miniball	24

2.7.3	CD–Detector	25
3	Penning Trap Theory	27
3.1	Single–Particle Theory	27
3.1.1	Newtonian Formalism	28
3.1.2	Classical Canonical Formalism	30
3.2	Inclusion of Additional Forces in the Model	33
3.2.1	Frictional Damping	33
3.2.2	Excitation with RF–Fields	35
3.2.3	Quadrupole Excitation with Frictional Damping	39
3.3	Multiple–Particle Theory	42
4	REXTRAP Setup	47
4.1	Overview	47
4.2	Off–Line Test Ion Source	49
4.3	High Voltage Platform	50
4.4	Trap Inner Structure	50
4.5	Vacuum System	53
4.5.1	Buffer Gas System	53
4.6	Operational Procedure of REXTRAP	54
4.6.1	Deceleration and Injection	54
4.6.2	Stopping and Trapping	55
4.6.3	Ejection and Acceleration	55
4.7	Operational Cycle of REXTRAP	56
5	The REXTRAP Control System	57
5.1	Overview	57
5.2	Hardware	57
5.2.1	GPIB	58
5.2.2	PROFIBUS	58
5.2.3	Fast Switching of Trap Electrodes	59
5.2.4	Timing of the REXTRAP setup	59
5.3	Software	60
5.3.1	FEC	60
5.3.2	Client PC	62
6	The Transfer Line To The EBIS	67
6.1	Overview	67
6.2	Beam Path	68
6.3	Vacuum System	69
6.4	Beam Observation and Detection	69

7	Experimental Results	73
7.1	REXTRAP	73
7.2	Transfer Beam Line	80
7.3	REX-ISOLDE Beam Time November 2000	81
7.4	Using REXTRAP for Conversion Electron Spectroscopy	83
7.4.1	Setup	83
7.4.2	Results	85
8	Conclusion and Outlook	87
	Appendix	89
A	Coulomb Excitation and Neutron-Transfer Reactions	89
A.1	Coulomb excitation	89
A.2	Neutron Transfer Reactions	91
B	Addendum to the Penning Trap Theory	93
B.1	Shift of the Resonance Frequencies of the Damped Ion Motions	93
B.2	Discussion of the Fourier Transformation of the Excitation	95
	Bibliography	97
	Acknowledgements	103

List of Figures

1.1	Part of the nuclide chart showing the neutron and proton drip-line and the deformed and intruder states	4
1.2	The S–Cl–Ar cycle in the rp-process	6
1.3	The WITCH retardation spectrometer	8
2.1	Schematic overview of REX–ISOLDE	11
2.2	Detailed layout of REX–ISOLDE	12
2.3	Elements available at ISOLDE	13
2.4	Overview of the ISOLDE RNB–facility	14
2.5	A photograph of the REXEBIS residing above the REXTRAP high voltage cage	16
2.6	Nier spectrometer for mass separation	16
2.7	3D–schematic drawing of the REX–RFQ	18
2.8	Deformation of the ion–cloud in radial direction	18
2.9	AG–Focussing of the ion beam	18
2.10	Axial field component of the RFQ–electrodes	19
2.11	A photograph of the REX–RFQ before installation	19
2.12	Schematic drawing of the rebuncher	20
2.13	Schematic drawing of the REX–IH structure	20
2.14	The drift–tube configuration of an IH–structure	21
2.15	Principle of changing the final energy of the IH–structure by adjusting the capacitive plungers	21
2.16	Photograph of one REX–ISOLDE 7–gap resonator	22
2.17	The Miniball detector	24
2.18	CD–Detector	25
3.1	Quadrupole potential	27
3.2	A hyperbolic trap	28
3.3	A cylindrical trap	28
3.4	The motion of a single particle in a Penning Trap	30
3.5	Generating an azimuthal electric dipole or quadrupole field by using a split centre electrode	37

3.6	Conversion from a pure magnetron to a pure cyclotron motion by quadrupole excitation at ω_c	38
3.7	Effect of the frictional damping with and without coupling by an azimuthal quadrupole field	42
3.8a	Shift of the magnetron frequency	44
3.8b	Shift of the reduced cyclotron frequency	44
3.9	Shift of the cooling resonance frequency	44
4.1a	A top view of REXTRAP	47
4.1b	A picture of the REXTRAP–Magnet inside the Faraday–cage	47
4.2	Beam Path from ISOLDE to REXTRAP	48
4.3	The REXTRAP Off–Line Ion Source	49
4.4	The electrode structure of REXTRAP	51
4.5	Buffer gas pressure and electric potential distribution	52
4.6	Overview of the REXTRAP vacuum system	53
4.7	Buffer gas cooling in longitudinal direction	55
4.8	Time structure of the REXTRAP operational cycle	56
5.1	Fast Switching of Electrodes at REXTRAP	59
5.2	Coupling of the REXTRAP timing to the REX–ISOLDE cycle pulse	60
5.3	The interplay of the different processes running on the FEC	61
5.4	DevCon program with dialog box for a High Voltage power supply	63
5.5	DevCon program with a ‘Synoptic’–like desktop	63
5.6	Control of the trap electrodes with DevCon	64
5.7	The input mask of the RexControl program	65
5.8	The RexControl program during operation	66
6.1	The Transfer Beam Line	67
6.2	Calculated beam path through the transfer line	68
6.3	Schematic overview of the vacuum system for the transfer beam line	69
6.4	Principle of the beam observation system	70
6.5	3D–sketch of the beam observation element	70
7.1	TOF–spectra of trapped cesium ions with argon as buffer gas	73
7.2	TOF–spectra of trapped ions coming from ISOLDE	74
7.3	Shifts of the magnetron and the reduced cyclotron frequency	75
7.4	Shift of the cyclotron frequency	76
7.5	Effect of a second excitation after 20 ms cooling at ω_c	77
7.6	Time–of–flight spectrum of trapped ^{26}Na	78
7.7	The number of ejected ions from REXTRAP as a function of the buffer gas pressure for Cs^+ in Ne	79
7.8	Beam profile taken during the REX–ISOLDE beam time Nov. 2000	80
7.9	Beam profile in the transfer beam line	80

7.10 Mass Scan of the residual gas beam out of REXEBIS	81
7.11 Energy spectrum of an accelerated beam	82
7.12 Electrons flying to the detector	84
7.13 Electron Spectrum of trapped ions	86

List of Tables

2.1	Peak charge–state after 20 ms breeding	15
2.2	Measured parameters of the 7–gap resonators	23
4.1	Constants used to calculate the buffer gas pressure for a given control voltage	54
7.1	Trapping efficiencies of selected ion species	78
7.2	Radioactive isotopes used in REXTRAP	79

Introduction

With the introduction of Radioactive Nuclear Beam facilities (RNB) the opportunity to study nuclear matter far from stability arose. Throughout the years the available beams and their intensity have been improved. An overview of radioactive beam facilities around the globe, together with an introduction of the techniques for the production of rare isotopes, can be found in [RNB00].

In the field of nuclear physics the use of radioactive nuclear beams provides an opportunity to probe and extend the nuclear models of nuclei far from stability. Also new phenomena could be revealed including halo nuclei, proton radioactivity and exotic shell effects. All these can help to obtain a better understanding of nuclear matter. Besides this, various other fields of research could benefit from the use of the availability of unstable nuclei. Nuclear astrophysics benefits both from the spectroscopy of rare isotopes which appear in the r - and rp -process and from the possibility to study nuclear reactions with nuclei far from stability, which could up to now only be done using theoretical models like the shell model. Radioactive isotopes are also used in the growing field called nuclear solid state physics. In this field unstable isotopes are used as probes which are implanted into the lattice structure of the sample material. The field of nuclear medicine also benefits from the use of radioactive beam facilities where radioactive samples can be collected on-line.

ISOLDE (Isotope Separator On-Line) is a radioactive nuclear beam facility located at CERN (Geneva/Switzerland) using the so-called ISOL-technique for the production of unstable isotopes. The radioactive isotopes are produced by nuclear reactions in a thick target induced by the impact of highly energetic protons. The produced ions are accelerated to 60 keV and separated by their mass. The other possibility for the production of radioactive nuclear beams is the in-flight method. There an energetic heavy ion beam is fragmented or fissioned while passing through a thin target after which the reaction products are mass, charge and momentum separated in a fragment separator. ISOLDE started its operation in 1967. Since that time there has been a steady development of its technical performance and its physics programme. The experience gained in target technology has lead to a wide range of radioactive isotopes available at ISOLDE. At present about 600 different isotopes from more than 60 elements can be produced.

In order to perform experiments near the Coulomb barrier, post-acceleration of

the produced radioactive ions is required. REX-ISOLDE is a post-accelerator which takes radioactive ions coming from ISOLDE and accelerates them from 60 keV up to 2.2 MeV/u. It uses a new concept of bunching and charge-breeding of the radioactive ions, which results in a compact and cost-effective linear accelerator. The ions are first captured in a Penning trap and afterwards injected into an EBIS (Electron Beam Ion Source), where their charge-state will be increased. The highly charged ion bunch is then accelerated in a short linear accelerator, consisting of a RFQ, an IH-structure and three 7-gap resonators. The system has to meet the following requirements: the final energy has to be sufficiently high to perform physics experiments near the Coulomb barrier and the efficiency has to be high in order not to waste the radioactive ions.

The main topic of this thesis is the construction and commissioning of REXTRAP, a large gas-filled Penning trap. The aim of REXTRAP is to accumulate and bunch the radioactive ions coming from ISOLDE. The ions have to be cooled in order to achieve an emittance small enough for an efficient injection into the EBIS. To achieve this goal buffer gas cooling together with a mass-selective rf-sideband cooling mechanism are applied. The first chapters in this thesis are dedicated to the physics opportunities opening up with REX-ISOLDE followed by an overview of the REX-ISOLDE post-accelerator concept together with a description of its elements. The next chapter is an introduction to the theory of a Penning trap. The general motion of a particle in the field of a Penning trap is derived and a formalism developed, which includes the repulsive force of the buffer gas and the excitation by rf-fields. At the end of the chapter the problems which arise when going from a single particle theory to a multiple interacting particle theory inside a Penning trap are discussed. The results of recent simulations are also presented. The following chapter is dedicated to the setup of REXTRAP. The parameters of REXTRAP and its operational cycle are discussed. The control system of REXTRAP consisting of the hardware and the software part is explained in the following chapter. The transfer beam line between REXTRAP and REXEBIS is a crucial point for the injection of the radioactive ion bunch into the REXEBIS. Its setup is described in Chapter 6. Afterwards the results of the commissioning experiments performed at REXTRAP are presented and discussed. Finally a conclusion of the REXTRAP operation as a beam cooler and buncher device as well as an outlook for its future operation in the REX-ISOLDE system is given.

Chapter 1

Physics Motivation

The original motivation for the construction of REX-ISOLDE was to study the nuclear structure of neutron-rich Na-Mg and K-Ca Isotopes around the neutron shell closures of $N=20$ and $N=28$ with Coulomb excitation and neutron transfer reactions. On top of this various different topics covering a wide range of physics areas should be investigated using the REX-ISOLDE post-accelerator:

- Nuclear structure
 - How are level schemes, $B(E\lambda)$ -values and quadrupole deformations changed in a region close to the drip-line?
 - What is the most appropriate nuclear model far from stability?
 - Do there exist new regions with extreme nuclear deformation?
 - Are there new collective modes to be found with stable octupole, oblate or triaxial nuclear shape?
 - Neutron halo nuclei: how many are there and do more forms exist?
- Nuclear astrophysics
 - The production of matter in the universe by nucleosynthesis: how did the processes proceed through bottlenecks, *e.g.* through the $^{35}\text{Ar}(p,\gamma)$ reaction in the rp-process?
 - Can more accurate measurements of stellar reactions contribute to the solution of the solar neutrino problem?
- Solid state physics
 - How will radioactive implantation, creating point defects and impurities, on a deep level in the semiconductor affect its properties?
- 'Low energy' experiments
 - Does the Standard Model describe the weak interaction correctly?

- Can the results of conversion electron spectroscopy be improved?

In the following sections an overview of the different experiments proposed for REX-ISOLDE as well as their physics background will be given.

1.1 Nuclear Structure Investigation

The main reactions for studying the nuclear structure of unstable, neutron-rich isotopes are Coulomb excitation and neutron transfer reactions. A detailed discussion of these reactions can be found in Appendix A. In the following sections the study of two different regions on the nuclear chart where experiments at REX-ISOLDE are proposed is discussed.

1.1.1 Neutron-Rich Nuclei Close to the Semi-Magic Shells of N=20 and 28

The shell model provides a good description of the nuclear structure of isotopes close to stability. Going from the valley of stability to the neutron rich nuclei quite different predictions are obtained, showing the uncertainty in predicting the nuclear forces, in particular their isospin dependence. For example in [Dob94] a change of the nuclear potential from a Woods-Saxon potential to a more parabolic harmonic potential is predicted, resulting in a lowering of the low- l single-

particle energies and an increase in the energy of the high- l levels. These modifications finally lead to changes in the magic numbers and hence new predictions of the preferred regions of nuclear deformation. On the other hand, relativistic mean-field theories do not confirm these changes. Furthermore, information on semi-magic nuclei is of particular importance for the determination of the monopole component of the nuclear interaction as their simple structure makes realistic calculations possible. Thus it is interesting to study the level structure and the quadrupole deformation in a systematic way near neutron-shell closures for neutron-rich nuclei.

A second phenomenon makes the situation even more complicated. Due to the strong neutron-proton interaction a strong core polarization occurs near closed shells,

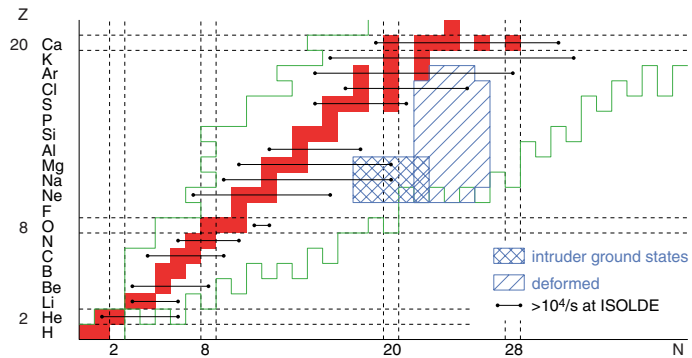


Fig. 1.1: Part of the nuclide chart showing the neutron and proton drip-line and the deformed and intruder states. The isotopes available at ISOLDE with sufficient yields for experiments at REX-ISOLDE are marked [Hab97].

resulting in low-lying intruder states [Woo92]. These are strongly deformed 2p2h-configurations which coexist alongside the more spherical configurations and may even become the ground state. A pioneer experiment using relativistic Coulomb excitation confirmed this neutron 2p2h-intruder structure of the ground state for the case of ^{32}Mg , where a low-lying first excited 2^+ -state (886 keV) with a large $B(E2)$ -value of $(426 \pm 34) \text{ e}^2\text{fm}^4$ has been measured, corresponding to a large deformation of $\beta_2 = 0.5$ [Mot95]. Triggered by this discovery a new region of well-deformed nuclei has been identified in a series of intermediate energy Coulomb excitation experiments at Michigan State University (MSU) [Sch96, Gla97] in the neutron-rich sulfur isotopes at and near the $N=28$ shell closure. The importance of intruder configurations has been shown in a systematic study of the chain of neutron-rich silicon isotopes ($^{32,34,36,38}\text{Si}$ [Ibb98]) as well as for neutron-rich Ne- and Mg-isotopes [Pri99]. However, all these experiments have so far been performed with the limited energy resolution of NaI scintillators. Thus a detailed nuclear level spectroscopy employing the Coulomb excitation and neutron-transfer reactions using MINIBALL as an efficient, high-resolution γ -detection setup to obtain more insight into the complex potential landscape of light neutron-rich nuclei and their single-particle structure will greatly enhance the experimental capabilities. In even-even nuclei, in addition to the excitation energy of the first 2^+ -state and its collectivity, the position of the second 0^+ -levels is of special interest to characterize the potential minima. The second 2^+ -level will give information on the triaxiality, low-lying negative parity states on neutron skin vibrations and octupole shaped vibrations. In the odd nuclei, where so far only sparse information is available, identified Nilsson orbitals will test the extrapolation of the single-particle energies.

1.1.2 Study of Light Neutron-Rich Nuclei

REX-ISOLDE will also provide interesting opportunities to investigate light bound and unbound nuclei in the region of the neutron drip-line. At present there is a large interest in studying the nuclear structure of such nuclei. The reason for this interest is that light drip-line nuclei have shown novel structural features that make them very attractive. One of the most striking discoveries was the observation that drip-line nuclei can develop dilute, spatially very extended nuclear matter distributions referred to as nuclear halo states. The prime example of such a nucleus is ^{11}Li . Its halo belongs to the so-called Borromean halo states, where the three-body system ($^9\text{Li}+n+n$) is bound while the two binary subsystems (^{10}Li and $2n$) are unbound. The Borromean nuclei are of great interest since they are situated at the threshold that separates the discrete and the continuous spectra. They are held together by forces that in neighbouring nuclei give rise to scattering states, which leaves strong imprints on those states in the form of final-state interactions. It is therefore important to obtain basic understanding of the continuum. The following list shows four different experiments which are possible with the energies of REX-ISOLDE and

which will be of importance in gaining insight into the physics of halo states.

- A study of the structure of the unbound nucleus ^{10}Li is of key importance for the theoretical investigation of the halo structure. To study this nucleus a ^9Li -beam is used together with a deuterium- and ^9Be -target.
- The study of the unbound nuclei ^5He and ^7He can help in understanding the structure of the ^6He and ^8He halo nuclei whose composition is under discussion.
- With $^9\text{Li}+p$ reactions the characteristics of the lowest excited states in ^{10}Li can be studied by investigating the isobaric analogue states in ^{10}Be .
- The heaviest known one-neutron halo nucleus is ^{19}C . An important ingredient in the interpretation of the data which results from the systematic study of the momentum distribution of charged fragments after one-neutron breakup of $^{15,17,19}\text{C}$ is the spin of the ground states of these nuclei. At REX-ISOLDE one can extract information about the spin of the ^{17}C ground state. This can be done by studying the reaction $^{16}\text{C}+p$.

1.2 Nuclear Astrophysics

In the field of nuclear astrophysics one is mostly interested in the determination of reaction rates of processes in nucleosynthesis reactions. Experimental results can help to verify the theoretical models. With the help of REX-ISOLDE such reactions can be measured by using inverse kinematics. The energies of REX-ISOLDE are in the region which is necessary to study such reactions in their natural energy regime.

1.2.1 Nucleosynthesis and the rp-Process

One proposed reaction to be studied at REX-ISOLDE is $^{35}\text{Ar}(p,\gamma)^{36}\text{K}$ [Wie94] which is an important step in the rp-process. The rp-process is an explosive nucleosynthesis process where especially neutron deficient isotopes are produced by proton capture reactions. It is considered to occur in novae and X-ray bursts. The proton capture is in competition with the β^+ -decay. In this way sub-cycles resembling hot hydrogen burning cycles are formed. One example is the S-Cl-Ar cycle (Fig. 1.2). The main break-out reaction of this cycle is the former named $^{35}\text{Ar}(p,\gamma)^{36}\text{K}$ reaction which becomes dominant for temperatures above $T = 3 \cdot 10^8$ K. The rp-process flux proceeds then mainly through this bottle-neck reaction. Thus the reaction flow to higher mass numbers

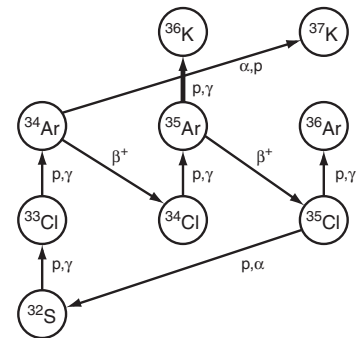


Fig. 1.2: The S-Cl-Ar cycle in the rp-process [Wie94].

through this bottle-neck reaction. Thus the reaction flow to higher mass numbers

can only be understood with accurate information about the rate of this proton-capture. The experimental knowledge of the reaction rates can give hints for the theoretical calculations of the reaction rates in the rp-process.

1.2.2 Stellar Burning and the Solar Neutrino Puzzle

Another important reaction to be studied at REX-ISOLDE is ${}^7\text{Be}(p,\gamma){}^8\text{B}$ [Cam97] which takes part in the pp-chain during the hydrogen burning of a main sequence star. The pp-chain splits into three chains which have a different production rate for solar neutrinos. The magnitude of the astrophysical S-factor for this reaction is of special interest in solving the solar neutrino problem as this reaction determines the branching ratio between the ppII and ppIII chain [Obe93]. Considerable effort has been made in determining the low-energy cross section of this reaction in recent years, but the low-energy results still remain somewhat controversial (from 16 to 45 eVb). Another crucial point is the extrapolation of the S-factor down to the relevant stellar energies around 20 keV. Usually pure s-wave capture dominates at low energies and accordingly, the stellar S-factor is calculated using this assumption. However, as the p-wave part of the cross section decreases with the energy much faster than the s-wave part, the cross section measured at $E > 120$ keV may still contain considerable amount of p-wave admixture at higher energies, thus an extrapolation which only considers s-wave capture will overestimate the S-factor at stellar energies. The important p-wave strength can be determined using a polarized ${}^7\text{Be}$ beam, which enables one to separate different partial wave contributions to the cross section.

To study this reaction an accelerated beam of radioactive ${}^7\text{Be}$ -ions is guided onto a windowless H_2 gas target which allows an investigation in inverse kinematics. The ${}^8\text{B}$ residual nuclei will be implanted together with the ${}^7\text{Be}$ beam in a beam stopper and periodically moved in front of a particle detector to observe the β -delayed α -decay of ${}^8\text{B}$. The corresponding center of mass energy for this reaction ($E_{\text{cm}} = 0.7 - 1.75$ MeV in $\text{H}({}^7\text{Be},\gamma){}^8\text{B}$) will cover the interesting energy region where the direct capture mechanism is dominant and will thus lead to an improved basis for the extrapolation to solar energies.

1.3 Nuclear Solid State Physics

Solid state physics experiments with radioactive ion beams have a long tradition at the ISOLDE on-line isotope separator. The opportunity to provide a wide variety of isotopically and chemically clean radioactive ion beams of rather high intensities and the possibility to implant the isotopes on-line has attracted a continuously increasing number of materials research groups, particularly in the field of semiconductor physics. REX-ISOLDE with its ability to produce ion beams of higher energy will open up a new generation of solid state physics experiments due to the advantage of deeper implantations.

The first solid state physics experiments at REX-ISOLDE will concentrate on the investigation of 'Hydrogen in Semiconductors' with the use of energetic radioactive beams [FW94]. Although previous experiments in this area have so far been very successful, the availability of post-accelerated ion beams will improve the experimental conditions in a unique way by:

- preventing surface problems and enabling experiments inside a diode structure
- monitoring the H-depth profile
- enabling the comparison of PAC with other techniques
- increasing the sensitivity
- improving tracer techniques

1.4 'Low energy' Experiments

Besides the experiments with accelerated radioactive beams a number of experiments have been proposed which use the 'low energy' part of REX-ISOLDE. The low energy side of REX-ISOLDE is able to deliver single- or highly-charged cooled and bunched radioactive ion beams. Two examples for such experiments are presented in the following sections.

1.4.1 Weak-Interaction Studies with WITCH

The WITCH (**W**eak **I**nteraction **T**rap for **C**harged particles) experiment is a retardation spectrometer coupled to a Penning trap system. It will be placed behind REXTRAP [Bec99, Bec00] (see Fig. 1.3). The idea is to measure the beta-neutrino angular correlation via the shape of the recoil energy spectrum of ^{35}Ar and ^{46}V . By this, the coupling constants of the electro-weak interaction can be determined. In its present form the Standard Model describes nuclear weak processes in terms of Vector (V) and axial-vector (A) type interactions. Although all experimental data today shows strong evidence for this V-A form, the limits on possible admixture of scalar (S) and tensor (T) type interactions are still rather poor. The present experimental limit from nuclear beta-decay experiments for the coupling constants C_T and $C_{T'}$ for a

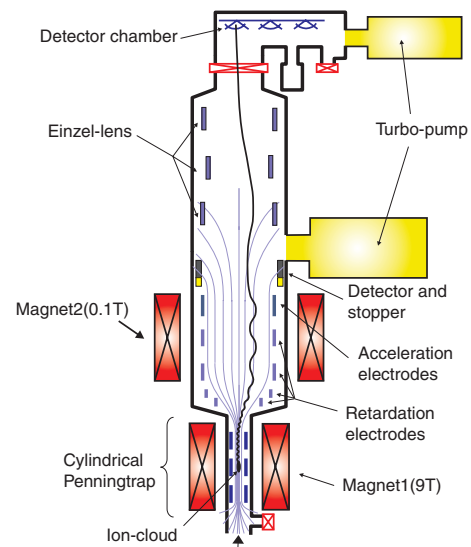


Fig. 1.3: The WITCH retardation spectrometer [Bec00].

tensor–interaction compared to a vector coupling constant is 0.13, while for a scalar–interaction the coupling constants C_S and $C_{S'}$ can be as large as 0.17. The limits are mainly determined by the accuracy of the measurement of the beta–neutrino correlation coefficient and are deduced from the angular correlation between the lepton and the neutrino. Due to the difficulties in detection of the neutrino the determination of the correlation has to be done indirectly. A possible way is the measurement of the recoil energy spectrum of the ions after β –decay, since the energy of the ion is influenced by the relative emission angle of the lepton and the neutrino. One of the major sources for systematic uncertainties in most nuclear beta–decay experiments is scattering of the particle in the source and the intermediate medium between the source and the detectors. The reduction of this limiting factor will be one of the main advantages of the WITCH retardation spectrometer. The ion trap permits the storage and cooling of ions for an extended period of time, providing very well localised sources of radioactive ions with almost zero thickness. The recoil particles after beta–decay can leave the source with virtually no loss of energy. REXTRAP will be used there as a beam cooler and buncher.

1.4.2 Conversion Electron Spectroscopy Inside REXTRAP

Another interesting application is the use of REXTRAP as a source for precision conversion electron spectroscopy. The limiting factor for high–resolution spectroscopy of low–energy electrons emitted by radioactive nuclei is the scattering of the electrons in the source material, where the ions are implanted. The detection of conversion electrons from the decay of trapped ions provides new opportunities for such experiments since the trapped ions form a source of nearly zero thickness where the electrons can escape without energy loss due to scattering. The results of such a measurement will be presented in Chapter 7.4.

Chapter 2

The Elements of REX-ISOLDE

2.1 Overview

The Radioactive beam EXperiment (REX) at ISOLDE is described in detail in [Hab97], [Hab00] and in the Proposal [REX94]. A schematic overview of the REX-ISOLDE experiment is given in Fig. 2.1. REX-ISOLDE can be divided into two parts — a 'low energy' and a 'high energy' section. The low energy section consists of two elements. REXTRAP, a large, gas-filled Penning trap which has to prepare the beam coming from ISOLDE, and REXEBIS, whose aim is to increase the charge-state of the radioactive ions. The second part of REX-ISOLDE is a linear accelerator which increases the velocity of the radioactive ions to a final energy of 0.8 to 2.2 MeV/nucleon. A detailed drawing of the REX-ISOLDE setup, including an indication of the important parts, can be found in Fig. 2.2. In the following sections all the elements of REX-ISOLDE are described in detail.

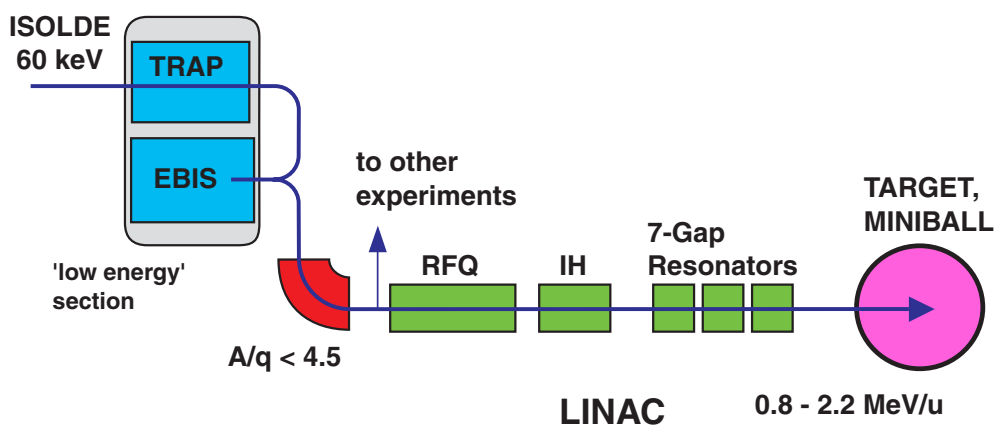


Fig. 2.1: Schematic overview of REX-ISOLDE.

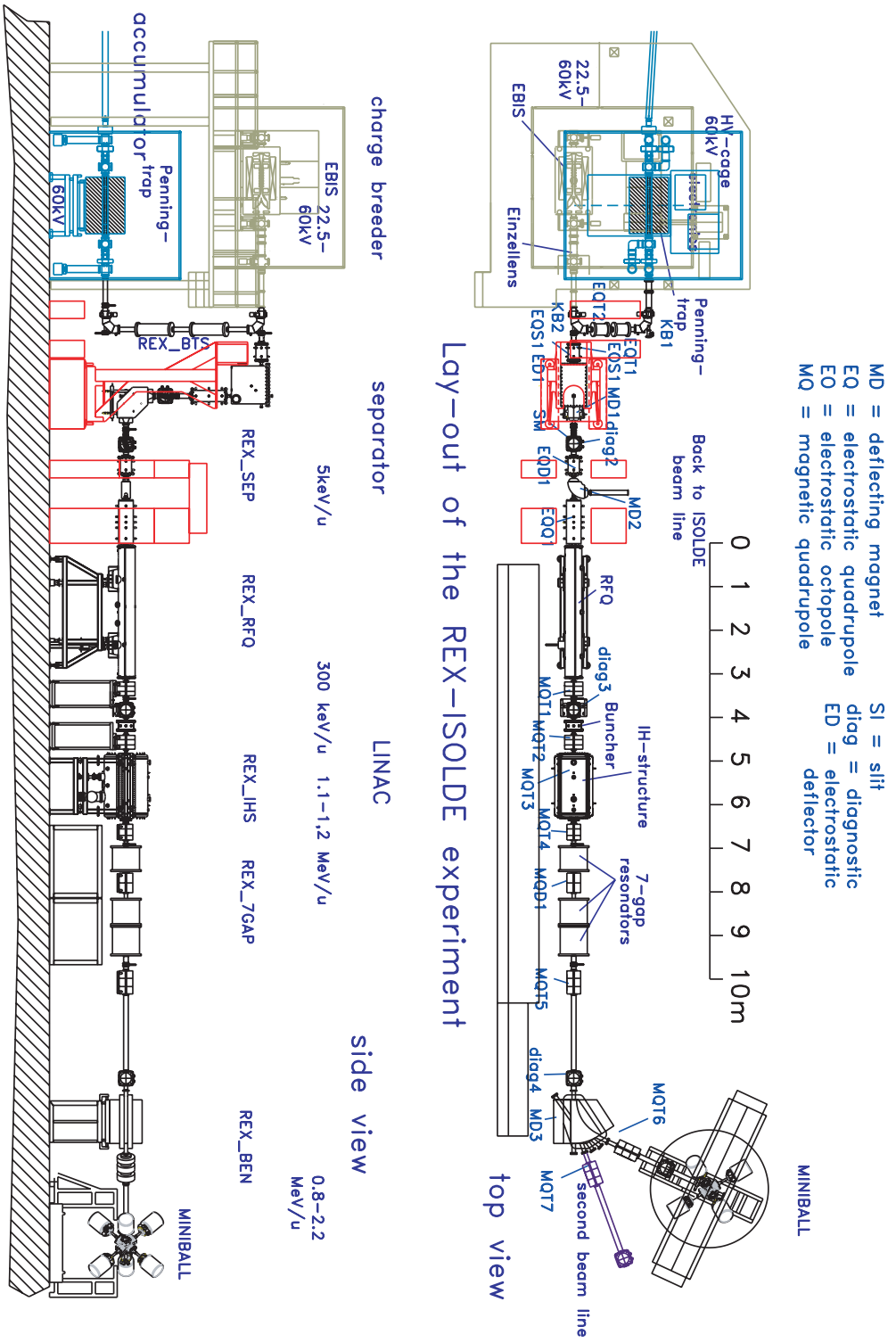


Fig. 2.2: Detailed layout of REX-ISOLDE [Hab00].

2.2 ISOLDE

The ISOLDE facility [Kug00] is a radioactive ion–beam facility situated at CERN. It produces pure low energy radioactive ion beams by use of the on–line isotope separation (ISOL) technique. This method makes use of spallation, fission and fragmentation reactions in suitable thick targets bombarded with high–energetic light particles from accelerators or thermal neutrons in high flux reactors. In the case of ISOLDE, the target is bombarded with 1...1.4 GeV protons from the PS Booster complex. The reaction products are stopped in the bulk of the target material, thereafter transported to an ion source, ionized and then accelerated again to an energy of 60 keV. The ions produced at ISOLDE are singly charged with an energy of 60 keV. The emittance of the ISOLDE beam is around $30 \pi \cdot \text{mm} \cdot \text{mrad}$. After thirty years of extensive research and development work in this field, methods are available to selectively and efficiently extract the stopped nuclear reaction products from the target and transform them into ion beams. These radiochemical methods take advantage of the physical and chemical properties of the individual elements and have been optimized for the majority of the elements. Today about 600 isotopes of more than 60 elements are available at ISOLDE (Fig. 2.3). These radioactive ion beams with half–lives as low as a few milliseconds can be delivered with intensities ranging from 10^{11} to 10^{-1} ions per second. More than 300 physicists are using these beams for a vast experimental program in nuclear, surface and solid state physics, nuclear medicine and astrophysics.

The layout of the ISOLDE facility is shown in Fig. 2.4. The protons coming from the PS Booster hit one of the two ISOLDE targets. Different target / ion–source units can be coupled to the ISOLDE front–ends for the production of the various radioactive ion beams. After extraction and acceleration to 60 keV the ions are sent to the magnetic mass separators. ISOLDE uses two different systems, the so–called General Purpose Separator (GPS) and the High Resolution Separator (HRS). The main difference between these is their mass resolving power. The GPS uses one 70° magnet and is able to achieve a mass resolving power of 2400 ($M/\Delta M$). The HRS consists of two magnets; one 90° and one 60° . With this setup a total mass resolving power of 7000 (without higher order correction elements) and 15000 (with higher order correction elements) can be achieved. The two isotope separators are connected to a so–called merging switch–yard which allows beams from either machine to be fed into a common beam distribution system; to which almost all the experiments in

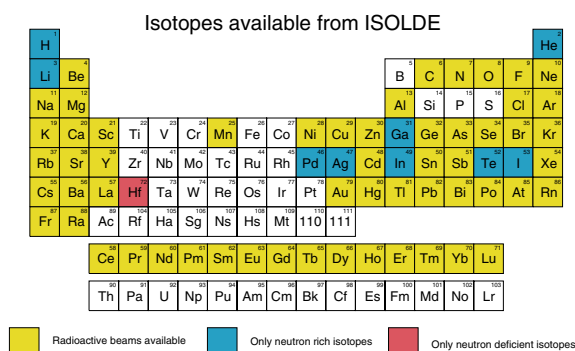


Fig. 2.3: Elements available at ISOLDE.

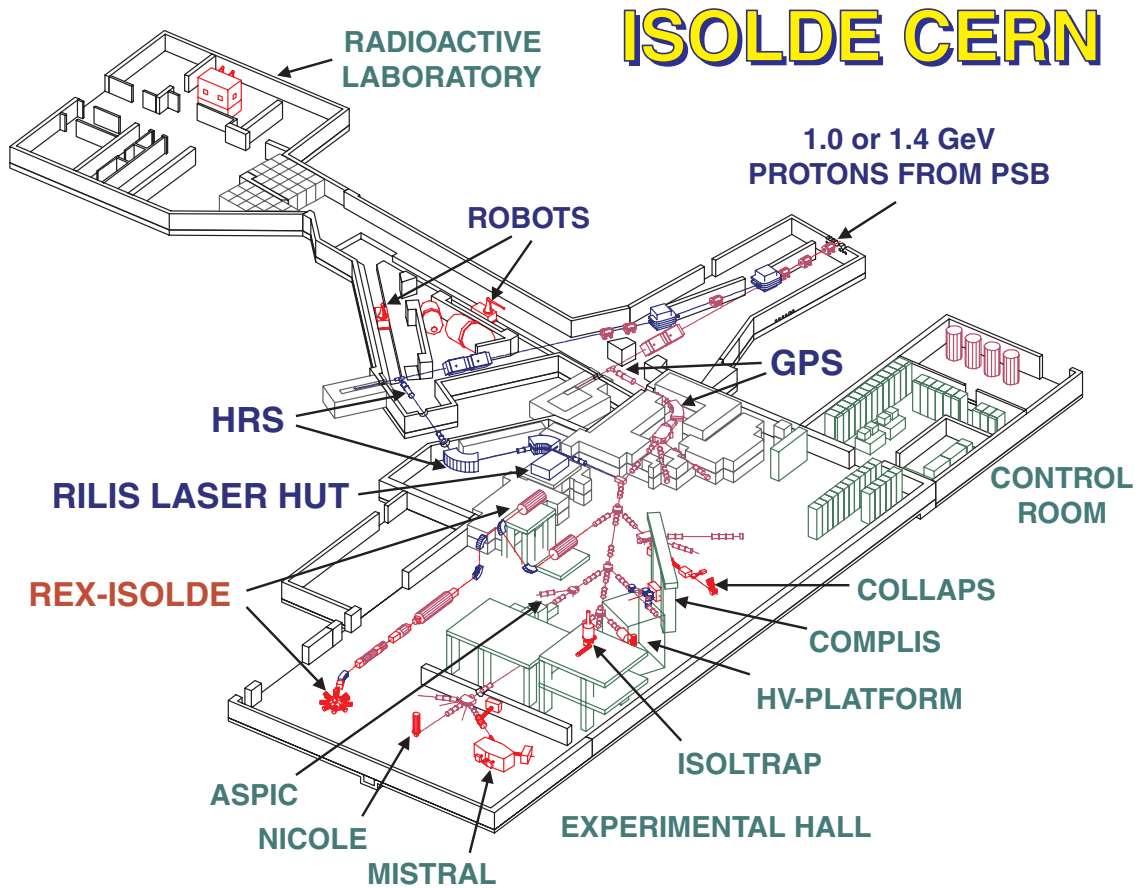


Fig. 2.4: Overview of the ISOLDE RNB-facility. The main parts and experiments are labeled. The protons coming from the PS-Booster (PSB) bombard either one of the two targets (GPS or HRS). After ionization the radioactive isotopes are mass-separated and distributed to the different experiments via the central beam line [Kug00].

the experimental hall are connected. Fig. 2.4 also shows the main experiments which are permanently installed at ISOLDE.

2.3 REXTRAP

The beam produced by ISOLDE is not suitable for injection into the EBIS. The acceptance of the EBIS is due to the small electron beam around $3 \pi \cdot \text{mm} \cdot \text{mrad}$. Therefore the ISOLDE beam needs to be cooled before injection. A second problem is the pulsed operation of the EBIS. For its operation a bunch of ions should be injected, however, ISOLDE produces a continuous beam of radioactive ions. To fulfil the necessary preparation of the ISOLDE beam the REXTRAP device is used. REXTRAP is a large, gas-filled Penning trap, the aim of which is to accumulate and cool the beam coming from ISOLDE and deliver a bunch of ions to the EBIS. The development and the

operation of REXTRAP is the main topic of this work and will be discussed in more detail in the following chapters.

2.4 REX-EBIS

To achieve a more efficient acceleration by the LINAC, the ions are charge bred from 1^+ to n^+ . For this purpose an EBIS (**E**lectron **B**eam **I**on **S**ource) is used.

An EBIS is an efficient charge breeding device with the following capabilities:

- Possibility to inject and trap ions,
- Confine the trapped ions in the electron beam for a period of time sufficient to reach the desired charge-state,
- Extract the highly charged ions from the EBIS along the electron beam axis and simultaneously prepare for the next cycle.

The EBIS uses a dense mono-energetic electron beam from an electron gun to further ionize the singly charged ions by electron impact ionization. The electron beam has a current of 0.5 A and 5 keV beam energy. It is focused and compressed by a strong magnetic field created by a surrounding super-conducting solenoid. This results in a current density of more than 200 A/cm². The injected ions are confined radially by the negative electron beam space charge and the magnetic field as well as longitudinally by potential barriers established by cylindric electrodes surrounding the beam. Inside the trapping region the high energetic electrons collide with the stored ions which are stepwise ionized until they are extracted by rising the trapping potential and lowering the extraction barrier simultaneously.

Inside REXTRAP the buffer gas pressure is of the order 10^{-3} mbar, while the REXEBIS requires an extremely good residual gas pressure (10^{-11} mbar) to avoid a complete outnumbering of the radioactive ions by residual gas ions. A four-stage differential pumping system in the transfer beam line and a differential pumping for the REXEBIS will provide an argon pressure of $\approx 10^{-14}$ mbar inside the REXEBIS, which yields an argon ion production of the same magnitude as 5000 injected sodium ions.

The ions coming from REXTRAP have an energy of 60 keV. To be able to trap the ions the REXEBIS operates on a high-voltage platform with 60 kV. The first part of the linac requires a beam with an energy of 5 keV/u with a charge-to-mass

Element	Charge-state
${}_8\text{O}$	7^+
${}_{11}\text{Na}$	9^+
${}_{12}\text{Mg}$	9^+
${}_{18}\text{Ar}$	11^+
${}_{19}\text{K}$	11^+
${}_{20}\text{Ca}$	12^+
${}_{36}\text{Kr}$	16^+
${}_{37}\text{Rb}$	18^+
${}_{51}\text{Sb}$	19^+
${}_{54}\text{Xe}$	21^+
${}_{82}\text{Pb}$	22^+
${}_{92}\text{U}$	22^+

Tab. 2.1: Peak charge-state after 20 ms breeding.

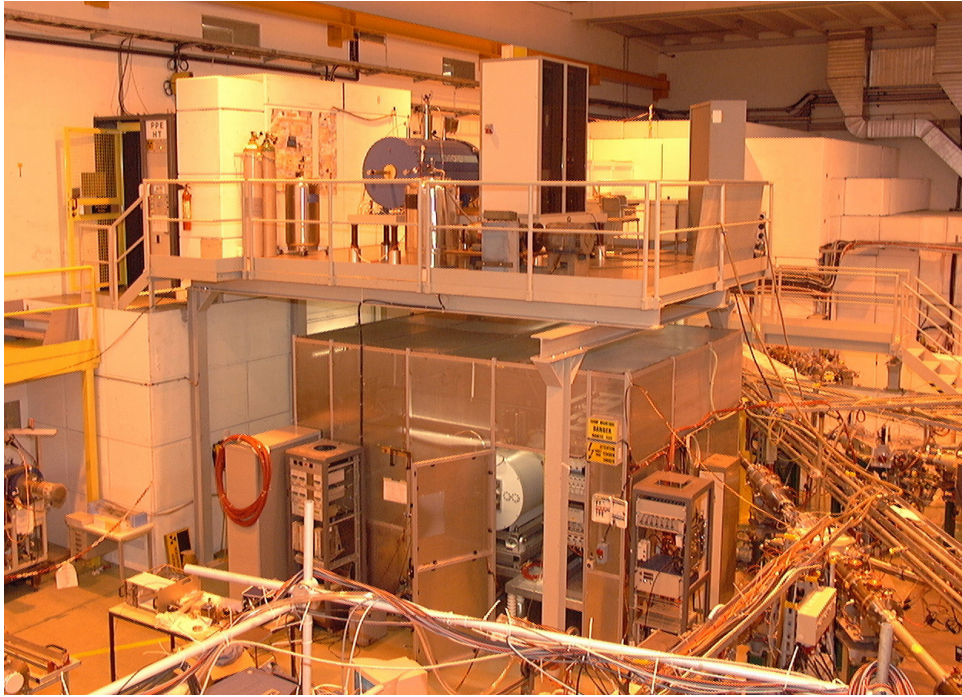


Fig. 2.5: A photograph of the REXEBIS residing above the REXTRAP high voltage cage.

ratio of 1:4.5. To achieve this, the platform has to be switched from 60 kV down to 15...22.5 kV. This switching has to be fulfilled between the injection and the ejection of the ions from the REXEBIS, *i.e.* the switching time must be less than 20 ms.

A detailed description of the REXEBIS can be found in [Wen01]. Fig. 2.5 shows the low energy section of REX-ISOLDE consisting of REXTRAP and REXEBIS during the construction phase in the ISOLDE hall.

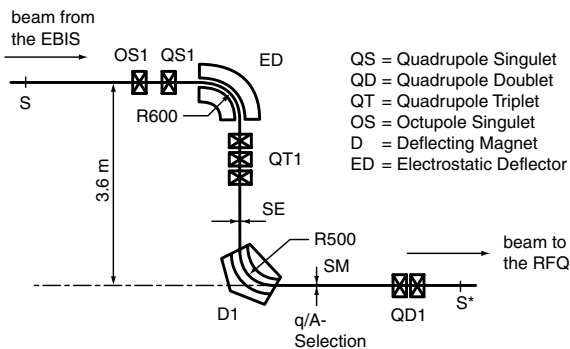


Fig. 2.6: Nier spectrometer for mass separation.

2.5 Mass-Separator

The EBIS produces not only highly charged ions of the desired isotope in the desired charge state. Due to residual gas contamination inside the EBIS, a wide variety of highly charged residual gas ions emerge. The intensity of the radioactive ions can be much smaller than the residual gas intensity. Also the charge state of the injected radioactive ions after charge breeding is distributed around the desired charge state. There-

fore a mass separator behind the EBIS is required.

Due to the energy spread of the ions ejected from the EBIS (<100 eV/q) and the required q/A -Resolution of about 150 a mass-separator based on a Nier-Spectrometer [Nie49] is used. Such a spectrometer consists of an electrostatic 90° cylinder deflector and a 90° magnetic bender arranged in a vertical S-shape (Fig. 2.6). The electrostatic deflector separates the ions according to their energy to a focal plane (SE). The desired charge-to-mass ratio is selected in the focal plane of the bending magnet (SM) independent of the energy. Assuming an emittance of $10 \pi \cdot \text{mm} \cdot \text{mrad}$ a resolution of 150 is expected.

2.6 REX-LINAC

After mass-separation the highly-charged radioactive ions are accelerated in a linear accelerator (REX-LINAC) to their final energy of 2.2 MeV/u. To achieve an efficient acceleration of ions a stepwise increase of the energy is required. Therefore the linac used for REX-ISOLDE consists of three different parts:

- 4-rod Radio Frequency Quadrupole (RFQ)
- Interdigital-H-type-(IH)-Structure
- Three 7-Gap Resonators.

All structures operate at 101.28 MHz and with 10% duty cycle. The linac can be operated with repetition rates of up to 50 Hz. The RFQ accelerates ions with a charge-to-mass ratio larger than 1:4.5 from 5 keV/u to 300 keV/u. Behind the RFQ the beam is longitudinally and transversely matched with two quadrupole doublet lenses and a rebuncher to achieve a good injection into the IH-structure. The IH-structure has 20 gaps and an inner tank triplet. It accelerates the ions up to 1.2 MeV/u. Afterwards the ions pass three 7-gap resonators which allow a final beam energy between 0.8 MeV/u and 2.2 MeV/u.

The overall transmission of the linac is expected to be better than 90% neglecting charge exchange and assuming a rather large emittance of the EBIS-beam of $60 \pi \cdot \text{mm} \cdot \text{mrad}$. The output current will have a micro-structure with pulses every 10 ns and a pulse-width of <1 ns (FWHM). The macro-structure has bunches with a typical pulse width of $50 \mu\text{s}$ and a pulse distance of 20 ms.

2.6.1 4-rod RFQ

In the first stage the ions are accelerated from 5 keV/u to 300 keV/u by a four-rod RFQ. The rf-quadrupole field provides transverse focusing for the low energy ions while an aperture modulation of the four rods performs smooth bunching and acceleration of the injected dc-beam. The REX-ISOLDE RFQ is derived from the

HLI-RFQ [Fri91] used at GSI and from the RFQ of the high-current injector at Heidelberg [Kle92]. The RFQ tank used at REX-ISOLDE is 3 m long and has a diameter of 0.32 m. The modulation of the four electrodes had to be optimized for a specific charge-to-mass ratio and for a specific input and output velocity. In order to gain efficient adiabatic bunching and optimum output emittances of the RFQ a rather low injection energy of 5 keV/u was chosen. The layout of the RFQ is conservative and therefore it is expected that for the maximum voltages between the rods even charge-to-mass ratios larger than 1:6.5 can be accelerated. This fact is important for the acceleration of heavier ions in future experiments. In Fig. 2.7 a schematic drawing of the RFQ used at REX-ISOLDE is shown.

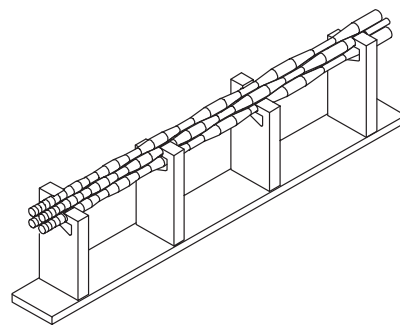


Fig. 2.7: 3D-schematic drawing of a 4-rod RFQ with plane stems and cylindrical electrodes [Sie01].

The quadrupole field formed by the four rods acts on the beam in a radial direction, both focussing and defocussing simultaneously as shown in Fig. 2.8. The rf-wave fed into the cavity continuously changes the polarity of the rods. Therefore it is possible to achieve a focussing in both radial directions as shown in Fig. 2.9.

Because of the special shape of the rods the electric field has not only a radial but also an axial component. By a suitable modulation of the four electrodes the electric field distribution changes in a way that the axial field component for the ions always points in the same direction (see Fig. 2.10). This results in an acceleration of the particles inside the RFQ.

The REX-RFQ consists of four sections: a radial matcher, the shaper, a gentle buncher and the acceleration section. These sections differ in the aperture modulation of the RFQ-electrodes and in the synchronous phase of each acceleration cell. The design value for the electrode voltage is 42 kV. The R_p value is 146 k Ω m with

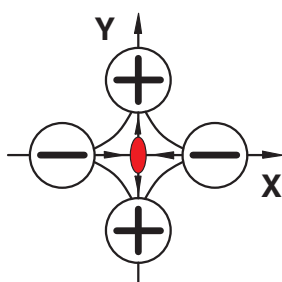


Fig. 2.8: Deformation of the ion-cloud in radial direction [Sie01].

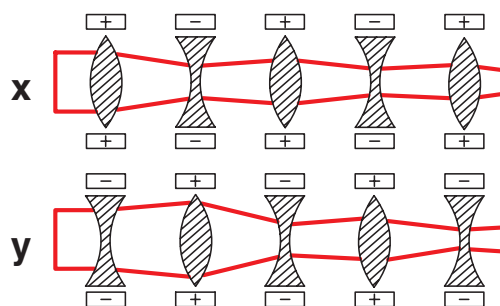


Fig. 2.9: Alternating gradient (AG) focussing of the ion beam by continuous changes of the rod polarity [Sie01].

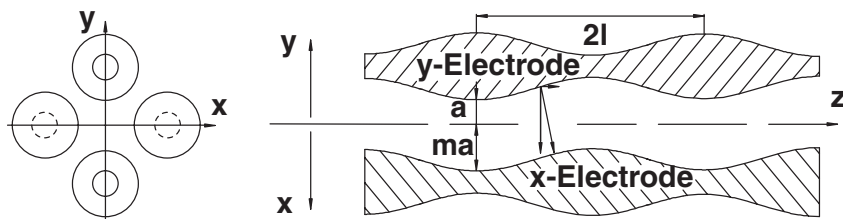


Fig. 2.10: Modulation of the electrodes to get an axial field component pointing always in the same direction [Sie01].

a quality factor of 4150. The total peak power consumption will be 36.5 kW. Beam tests carried out so far have shown almost no emittance growth for typical EBIS emittances ($10 \dots 30 \pi \cdot \text{mm} \cdot \text{mrad}$, 5 keV/u). The concept of a matching out section could be applied in order to reduce the beam slope at the exit of the RFQ for further focussing. Fig. 2.11 shows the RFQ resonator before installation. A detailed description of the setup and the operation parameters can be found in [Sie01].

2.6.2 The Matching Section

The very special beam dynamics concept of the IH-structure requires a rather small phase spread of the ion bunches and a converging beam in both transverse directions at the entrance of the IH-resonator. In order to match the beam from the REX-RFQ

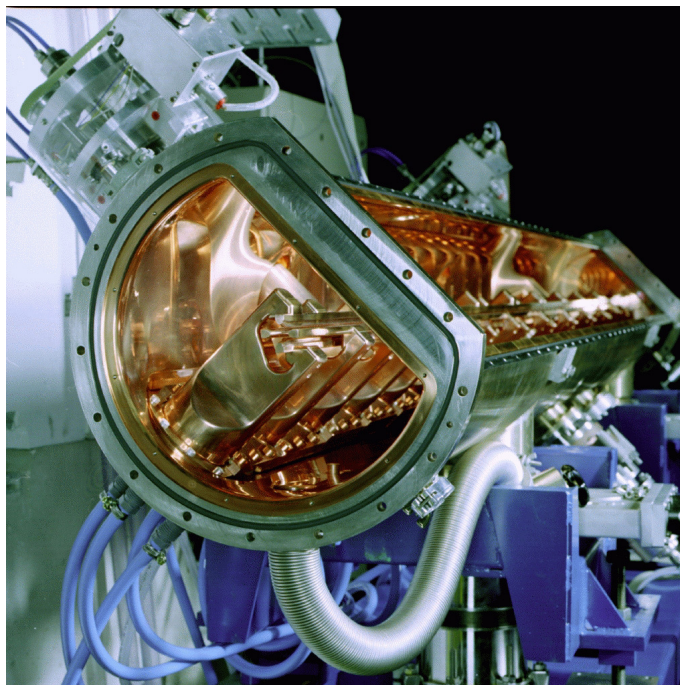


Fig. 2.11: A photograph of the REX-RFQ before installation [Hab00].

into the acceptance of the IH-structure a section consisting of two magnetic quadrupole triplet lenses and a rebuncher is required. The first triplet lens focuses the beam through the rebuncher and produces a waist for diagnostics. The second triplet lens matches the beam to the transverse acceptance of the IH-structure. The aperture of the lenses is 3 cm and the maximum gradient is about 60 T/m. The rebuncher is a three gap split ring resonator with a peak voltage of 70 kV which has to match the phase spread of $\pm 15^\circ$ to the phase spread acceptance of $\pm 10^\circ$ of the IH-structure (Fig. 2.12). Measurements at the power resonator result in a quality factor of 3500 and a shunt impedance of 4.5 M Ω /m. In order to reach the peak voltage a 2 kW rf-power will be required.

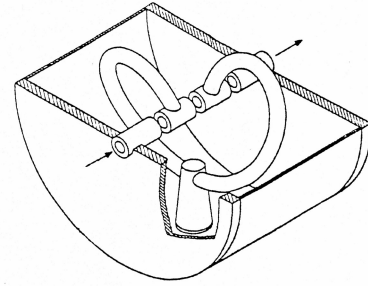


Fig. 2.12: Schematic drawing of the rebuncher [Emh99].

2.6.3 IH-Structure

After the RFQ and the matching section, the Interdigital H-type (IH)-structure [Emh99] follows as a second acceleration stage. An IH-structure is an efficient drift-tube accelerator with a compact setup. The REX-IH structure is 1.5 m long and has 20 gaps. The speciality of an IH-structure is the way in which the field is generated in the drift-tubes. Instead of directly applying the necessary voltage of a few MV, the field in the drift-tubes results from inductive and capacitive coupling of a rf-field inside the resonator. The IH-structure is a cavity resonator with the drift-tube structure mounted inside. The resonator will be operated in the TE₁₁₁- or H₁₁₁-mode, *i.e.* there are only transversal electric and longitudinal magnetic field modes respectively. The drift-tubes are mounted on alternating sides of the resonator. The rf-H₁₁₁-mode induces voltages of opposite polarity in the drift-tubes which accelerate a particle inside the drift-tube structure (Fig. 2.14). The inner structure of the IH is separated into different sections. After an initial acceleration section, with a 0°-synchronous particle structure, the ions drift through a magnetic quadrupole triplet lens for transverse focussing. Next the particles are rebunched using a negative synchronous phase ($\Phi_S \approx -30^\circ$) in the first three gaps behind the quadrupole triplet, followed by a second accelerating section with $\Phi_S \approx 0^\circ$. The triplet lens has an aperture of 22 mm and a length of 299 mm. The required field gradients are approximately 55 T/m. Due

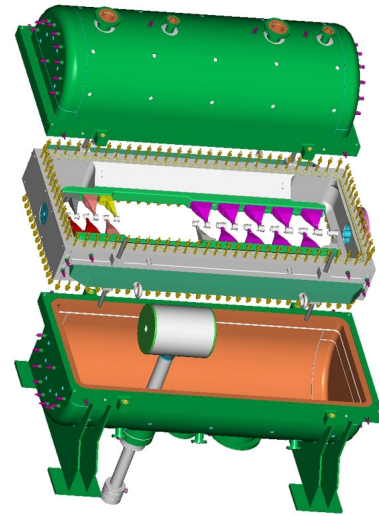


Fig. 2.13: Schematic drawing of the REX-IH structure [Emh99].

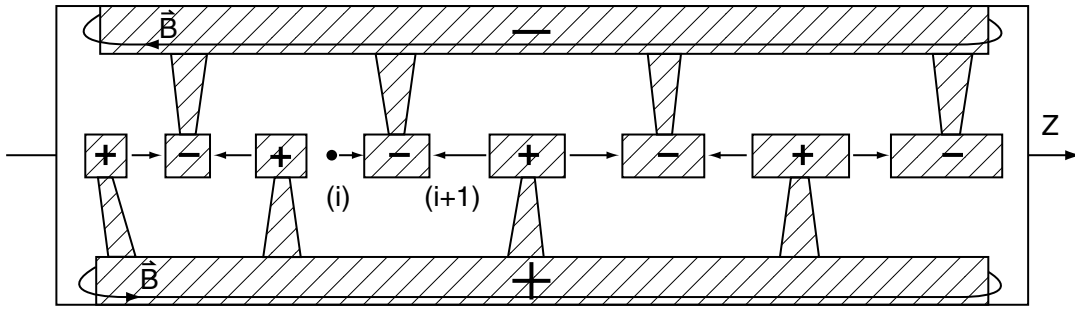


Fig. 2.14: The drift-tube configuration of an IH-structure. The magnetic field induces a voltage of opposite polarity in the opposite drift-tubes [Emh99].

to the small aperture the pole tips are made from normal soft iron. The maximum energy gain of about 0.9 MeV/u which is required corresponds to 4.05 MV effective resonator voltage or, 5.04 MV absolute voltage. With the measured shunt impedance of 300 M Ω /m, the total peak power consumption will be 60 kW.

To be able to achieve a variable final energy at REX-ISOLDE a new feature has been added to the REX-IH resonator. By adjusting the gap voltage distribution via two capacitive plungers and by adjusting the rf-power fed into the resonator, a variation of the final energy between 1.1 and 1.2 MeV/u can be realized. The lower final energy of the IH-structure is important for deceleration of the ions down to 0.8 MeV/u, since a deceleration from 1.2 MeV/u down to 0.8 MeV/u through the 7-gap resonators would produce a non-acceptable phase spread at the target; one which could not be reduced in a rebuncher without losses. This new concept has been examined thoroughly by bead perturbation measurements using a down scaled model (1:2) [Kei97]. Fig. 2.15 shows the principle of the variation of the gap voltage distribution. Moving the plunger at the low energy side towards the drift tubes the capacity and the

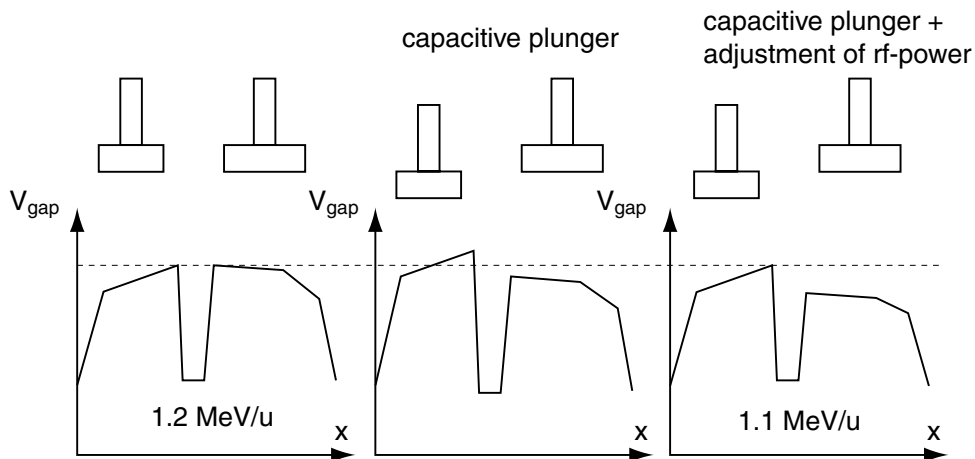


Fig. 2.15: Principle of changing the final energy of the IH-structure by adjusting the capacitive plungers [Hab00].

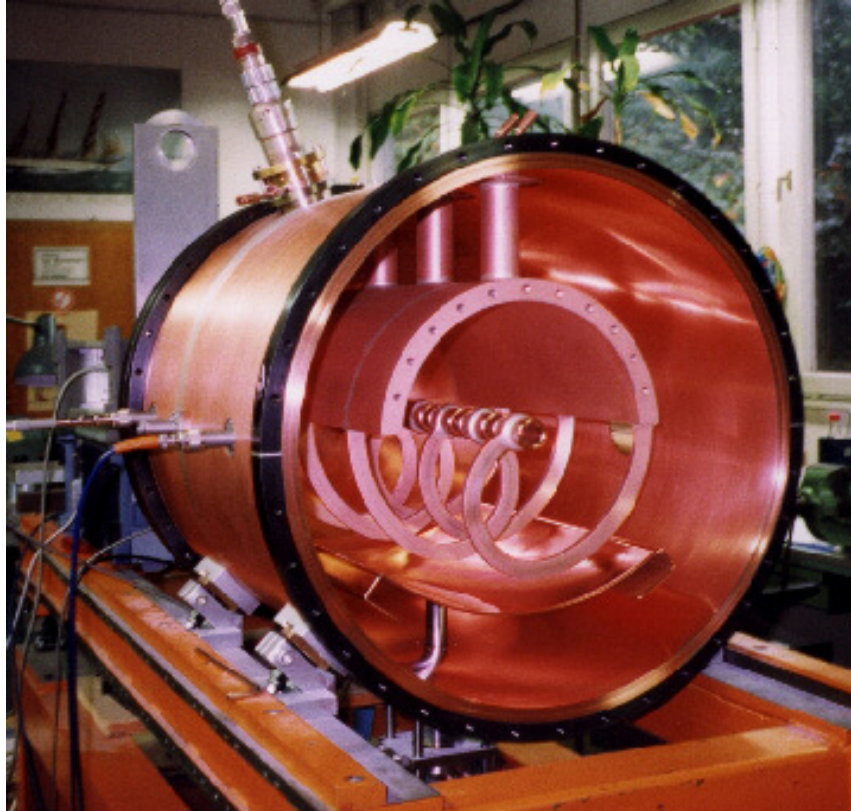


Fig. 2.16: *Photograph of one REX-ISOLDE 7-gap resonator [Hab00].*

gap voltage are increased. Consequently the gap voltages at the high energy side decrease relative to the voltages at the low energy side. A simultaneous reduction of the rf-power will lead to the correct gap voltage distribution for the final energy of 1.1 MeV/u.

A comparison between the reference gap voltage distribution as given by particle dynamics calculations, the measured distribution at the model and at the power resonator, have shown significant discrepancies in the calculated values to 2%. Thus for the power resonator, slight changes of the undercut geometry and of the drift tube structure had to be made in order to increase the resonator frequency which was too low for operation in the 1.1 MeV/u mode.

2.6.4 7-Gap Resonators

The high energy section of the REX-ISOLDE linac consists of three 7-gap resonators [Pod98, Pod99a, Pod99b]. These special types of spiral resonators are designed and optimized for synchronous velocities of $\beta_S = 5.4\%$, 6.0% and 6.6% . The 7-gap resonator is a compromise between the maximum reachable accelerating voltage and the maximum flexibility in the transit time factor. Each resonator has a single reso-

nance structure which consists of a copper half shell and three arms attached to both sides of the shell. Each arm consists of two hollow profiles, surrounding the drift tubes and carrying the cooling water (see Fig. 2.16). Copper segments on both sides of the half shell allow one to tune the resonator to the required resonance frequency of 101.28 MHz. The tuning plate, visible at the bottom of the resonator, corrects detuning effects due to temperature changes of the resonator or the half shell during operation. An additional quadrupole doublet lens between the first and the second resonator allows transverse focusing of the beam. The final ion beam energy can easily be adjusted between 0.8 and 2.2 MeV/u by tuning the rf power and the phase of the three active resonators.

The design voltage between the gaps is 1.74 MV at 90 kW rf power. Trials performed at the Max Planck Institute at Heidelberg with a test beam show a gap voltage between 1.77 and 1.88 MV. This corresponds to a shunt impedance between 59.5 and 62.5 M Ω /m. Table 2.2 shows the measured parameters of the three power type resonators.

Parameter	5.4 %	6.0 %	6.6 %
f [MHz]	101.28	101.28	101.28
Q-Value	5620 \pm 110	5420 \pm 110	5580 \pm 110
Z [M Ω /m]	62.5 \pm 4.0	59.7 \pm 3.6	59.5 \pm 3.5
U ₀ [MV]	1.77 \pm 0.05	1.81 \pm 0.05	1.88 \pm 0.05

Tab. 2.2: *Measured parameters of the 7-gap resonators, f...frequency, Z...shunt impedance, U₀...voltage. The shunt impedance and the resonator voltage are determined by beam tests.*

2.7 Target and Detectors

After the linac the beam is momentum separated in a dipole magnet and guided to a target station. It is surrounded by an efficient γ -spectrometer called "Miniball". This detector measures the γ -rays emitted after a Coulomb excitation or a neutron transfer reaction takes place. According to the geometrical requirements of the Miniball setup, a target chamber with its associate equipment has been built. It is a compromise between the minimum volume necessary to house the particle detectors and beam controls and the maximum volume that can easily be surrounded with Ge-detectors. A thin spherical aluminium structure has been chosen to minimize γ -absorption and scattering. A removable top lid provides easy access to the interior of the chamber which houses a turnable wheel with target holders, a Faraday cup and a beam collimator.

2.7.1 The Parallel Plate Avalanche Counter

The Parallel Plate Avalanche Counter (PPAC) [Cub00] was developed to serve as an efficient and spatially sensitive forward angle detector to monitor the radioactive ion beam behind the target. It has a compact design with a low effective thickness to prevent the radioactive ions from being stopped and to avoid large scattering angles. This reduces the background of other detectors in the target area. The detector is operated with a small gas flow of 4 to 10 mbar of isobutane and with voltages of about 600 V. The spatial resolution of ~ 1.6 mm is mainly determined by the width of the aluminium coated mylar strips inside the detector. To cover a large dynamic range of counting rates the PPAC supports two modes of operation. At low count-rates ($< 10^6$ s $^{-1}$ per strip) the signals can be read out from the end of the delay lines event-by-event, whereas at higher intensities, the current measured on all anode strips is recorded. With a rise time of the detector signals approximately 5 ns in the event-by-event read-out mode, the PPAC may even serve as a fast trigger.

2.7.2 Miniball

Due to the low intensity of produced exotic nuclei, the detection of γ -rays has to be very efficient. The total full-energy peak efficiency and not the resolving power has to be optimized. The γ -ray multiplicity is low, typically less than three. Although the bombarding energy of ~ 2 MeV/u is rather small, the reaction products have typical velocities of $v/c = 0.05 - 0.1$ which results in significant Doppler shifts of the de-excitation γ -rays. A high detector array granularity is therefore absolutely necessary to reduce the Doppler broadening of the γ -rays. Also, a coincidence measurement with a particle detector has to be fulfilled. As a detector the presently developed Miniball (Fig. 2.17) will be employed.

It is a cubic shaped Ge-array detector made of six clusters according to the design of the Euroball [Ebe96].

The individual modules have a length of 78 mm and a front diameter of 68 mm. In its final implementation the array will consist of 42 sixfold segmented Ge-detectors. Subgroups of 3 and 4 detectors in one common cryostat will allow flexible geometrical arrangements to accommodate specific experimental requirements. Prototype tests have resulted in an energy resolution of 2.1 keV (central contact) and 2.45 keV (individual segments) at $E_\gamma = 1.33$ MeV.

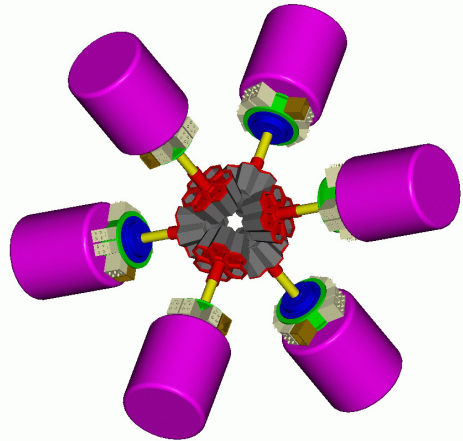


Fig. 2.17: The “Miniball” Ge-detector array. The six cryostats are included in the illustration.

Improved position resolution for γ -ray detection will be gained from radial position detection. Flash ADC measurements enable a detailed pulse shape analysis, and a radial position resolution of the first γ -interaction of about 5 mm is achieved. In order to combine this feature with a modern concept of electronic signal processing, Miniball will be instrumented only with digital electronics based on flash ADC's and DSP's. Moreover, the digital electronics preserve the energy resolution of conventional analogue high resolution spectroscopy electronics at substantially higher count rates.

A new data acquisition and analysis system has been developed on the basis of the GSI front-end system MBS [Ess] combined with the ROOT framework from CERN [Bru] for the back-end visualization. This will provide a high-performance data acquisition and analysis system for the users of REX-ISOLDE.

2.7.3 CD-Detector

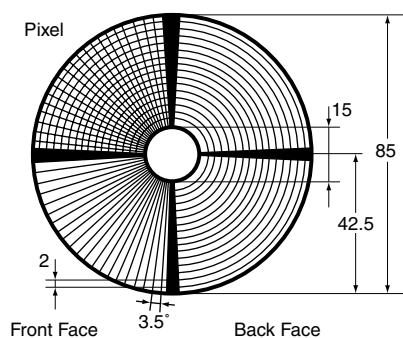


Fig. 2.18: *Double Sided Silicon Strip Detector (DSSSD) with CD geometry [Sel91].*

To measure coincidences of the detected γ -rays with a collision event and to further allow Doppler shift correction of the measured γ -rays a position-sensitive silicon detector based on the Double-Sided Silicon Strip Detector technology (DSSSD) detects scattered ions or the recoiling target nuclei in a relevant solid angle. The shape of the detector is similar to a Compact Disc, divided into four quadrants (see Fig. 2.18). The front side is segmented into 16 annular p+ strips per quadrant at 2 mm pitch, while the back side consists of 24 sectors of n+ strips at 3.5° pitch. This results in a total of 160 discrete detector elements and 93% effective area of the total 5000 mm². The silicon wafer thickness will be between 35 and 1000 μ m, depending on the application (as energy loss or total kinetic energy detector) [Sel91].

Chapter 3

Penning Trap Theory

3.1 Single-Particle Theory

In the following sections the motion of a single particle in a Penning trap is derived. In the first section this is done by solving the equations of motion for a charged particle in the electromagnetic field of a Penning trap. In the following section this information is then used to describe the behaviour of a stored particle in the classical canonical formalism. This description allows one to derive a general formalism for the inclusion of additional forces such as damping with buffer gas or excitation with rf-fields.

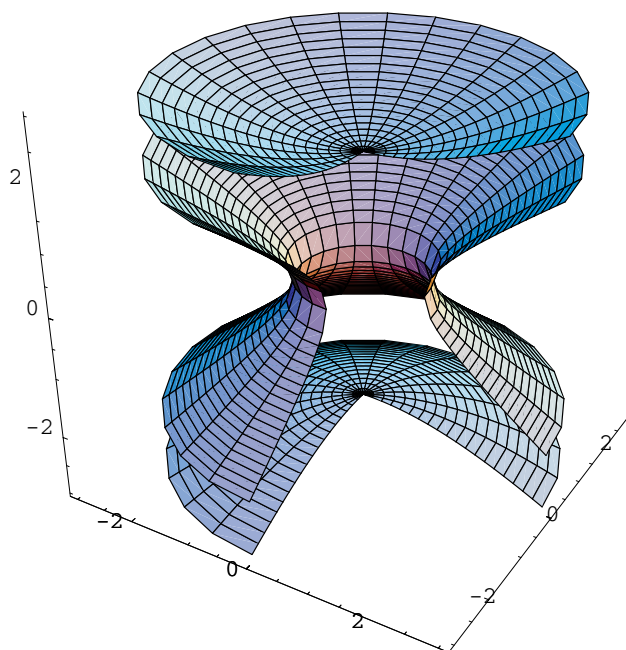


Fig. 3.1: *Quadrupole potential.*

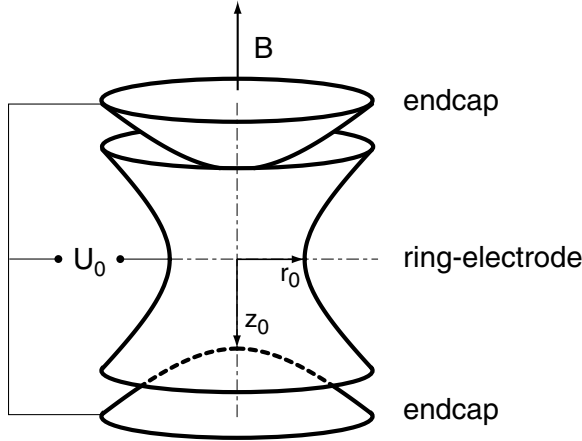


Fig. 3.2: A hyperbolic trap.

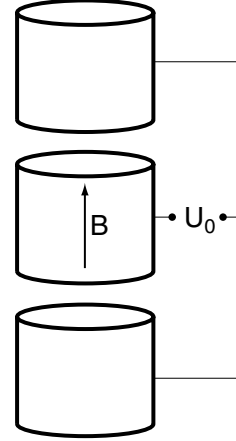


Fig. 3.3: A cylindrical trap.

3.1.1 Newtonian Formalism

The ideal Penning trap is a superposition of an electric quadrupole and a magnetic dipole field. The electric potential can be described via the following formula [Bau93], [Kre92b].

$$\Phi(r, z) = \frac{U_0}{2z_0^2 + r_0^2} (2z^2 - r^2) \quad . \quad (3.1)$$

A surface plot of the quadrupole potential can be seen in Fig. 3.1. There are two common approaches for reproducing such a potential. Fig. 3.2 shows a hyperbolic trap, where the shape of the electrodes follows the equipotential surfaces. Fig. 3.3 shows an alternative approach; if the voltages on the cylindric electrodes are properly chosen, the resulting field on axis reproduces a quadrupole potential quite well. Calculations have shown in the case of REXTRAP a deviation from the quadrupole field of the order 10^{-6} . But for precision experiments like mass-measurements a hyperbolic trap is indispensable. Nevertheless the cylindric electrodes are cheaper and easier to produce than hyperbolic electrodes. For REXTRAP a cylindric Penning trap is used.

The electric field can be calculated from the potential:

$$\vec{E}(r, z) = -\vec{\nabla}\Phi = \frac{2U_0}{2z_0^2 + r_0^2} (r\hat{e}_r - 2z\hat{e}_z) \quad , \quad (3.2)$$

and the equation of motion for a single particle in a Penning trap can be written as:

$$m\ddot{\vec{x}} = \vec{F}_{\text{Lorentz}} = q \cdot (\vec{E} + \vec{v} \times \vec{B}) \quad . \quad (3.3)$$

Since the magnetic field in a Penning Trap is parallel to the z -axis, its field strength is therefore:

$$\vec{B} = B_0 \cdot \hat{z} \quad . \quad (3.4)$$

Introducing the following definitions

$$\omega_z^2 = \frac{4U_0q}{m(2z_0^2 + r_0^2)} \quad (3.5a)$$

$$\omega_c = \frac{q}{m} \cdot B_0 \quad , \quad (3.5b)$$

where the value ω_z is the frequency of the axial motion and ω_c is the cyclotron frequency of a charged particle around a magnetic field line, then using these definitions we are now able to rewrite the equation of motion in Cartesian coordinates:

$$\ddot{x} - \frac{\omega_z^2}{2}x - \omega_c \dot{y} = 0 \quad (3.6a)$$

$$\ddot{y} - \frac{\omega_z^2}{2}y + \omega_c \dot{x} = 0 \quad (3.6b)$$

$$\ddot{z} + \omega_z^2 z = 0 \quad . \quad (3.6c)$$

The motion in the z-direction is a simple harmonic oscillation which is decoupled from the motion in the x-y plane. It has the following solution:

$$z = A_z e^{i\omega_z t} \quad . \quad (3.7)$$

To solve the other two equations we combine them into a complex equation using $u = x + iy$, giving

$$\ddot{u} - \frac{\omega_z^2}{2}u + i\omega_c \dot{u} = 0 \quad . \quad (3.8)$$

As we are interested in bound states we try the ansatz $u = e^{i\omega t}$. This gives us the following quadratic equation:

$$\omega^2 + \omega_c \omega + \frac{\omega_z^2}{2} = 0 \quad (3.9)$$

with the two solutions

$$\begin{aligned} \omega_{\pm} &= \frac{1}{2} \cdot \left(\omega_c \pm \sqrt{\omega_c^2 - 2\omega_z^2} \right) \\ &= \frac{1}{2} \cdot (\omega_c \pm \omega_1) \quad \text{with} \quad \omega_1 = \sqrt{\omega_c^2 - 2\omega_z^2} \quad . \end{aligned} \quad (3.10)$$

Bound states require the square root to be real. This leads to the following boundary condition:

$$\frac{\omega_c^2}{2} - \omega_z^2 > 0 \quad . \quad (3.11)$$

The general solution of (3.8) is:

$$u(t) = A_+ e^{-i\omega_+ t} + A_- e^{-i\omega_- t} \quad (3.12)$$

with the arbitrary complex constants $A_{\pm} = |A_{\pm}| e^{-i\alpha_{\pm}}$. We define $R_{\pm} = |A_{\pm}|$.

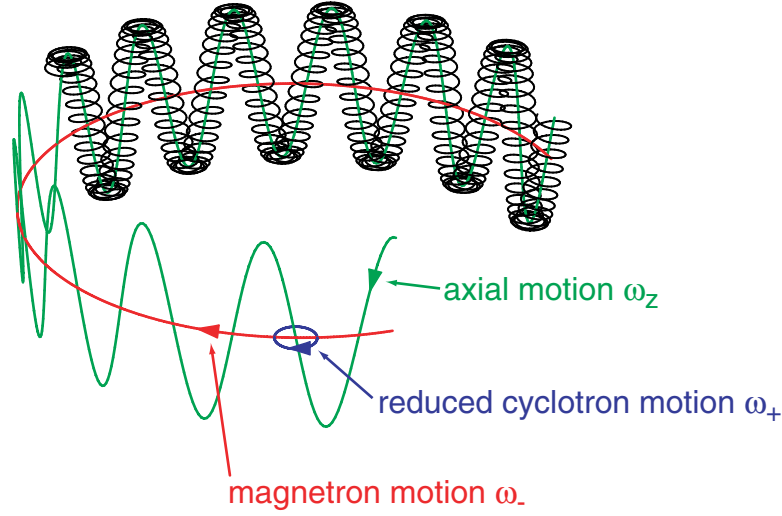


Fig. 3.4: The motion of a single particle in a Penning Trap.

Equation (3.12) represents a superposition of two circular motions with the frequencies ω_+ and ω_- . The frequency ω_+ is known as the *reduced cyclotron frequency* whereas ω_- is called the *magnetron frequency*. Under the usual operating conditions for a Penning trap the frequencies ω_+ , ω_- and ω_z differ by several orders of magnitude. One can assume

$$\omega_+ \approx \omega_c \gg \omega_z \gg \omega_- \quad . \quad (3.13)$$

3.1.2 Classical Canonical Formalism

In the previous section we derived the motion of a charged particle in a ideal Penning trap. Using this information we can now rewrite the theory of the Penning trap in the classical canonical formalism. In the following section the formalism is derived in the same way as done by M. Kretschmar [Kre92a].

To obtain the Lagrangian for the particle in the trap we need a generalized potential $V_0(x, \dot{x})$ which incorporates the electric and the magnetic potential. The vector potential for the magnetic field of the trap can be written as

$$\vec{A}_0(x, y, z) = \frac{1}{2} B_0 (-y \hat{e}_x + x \hat{e}_y) \quad , \quad (3.14)$$

so the generalized potential is now

$$V_0(\vec{x}, \dot{\vec{x}}) = q\Phi(\vec{x}) - \frac{q}{c} \dot{\vec{x}} \cdot \vec{A}_0(\vec{x}) \quad , \quad (3.15)$$

resulting in the Lagrangian,

$$L(\vec{x}, \dot{\vec{x}}) = T - V_0 = \frac{1}{2} m (\dot{x}^2 + \dot{y}^2 + \dot{z}^2) - \frac{1}{4} m \omega_z^2 (2z^2 - x^2 - y^2) - \frac{1}{2} m \omega_c (\dot{x}y - \dot{y}x) \quad . \quad (3.16)$$

For the canonical momenta one obtains

$$p_x = m\dot{x} - \frac{1}{2}m\omega_c y, \quad p_y = m\dot{y} + \frac{1}{2}m\omega_c x, \quad p_z = m\dot{z} \quad . \quad (3.17)$$

Using these momenta one can derive the Hamiltonian

$$H(\vec{x}, \vec{p}) = \vec{p} \cdot \vec{v} - L(\vec{x}, \vec{v}) = \frac{1}{2m} \left(\vec{p} - \frac{q}{c} \vec{A}_0(\vec{x}) \right)^2 + q\Phi(\vec{x}) \quad , \quad (3.18)$$

which can be rewritten using the corresponding expressions for the scalar and vector potential:

$$H(\vec{x}, \vec{p}) = \frac{1}{2m} \vec{p}^2 - \frac{\omega_c}{2} (xp_y - yp_x) + \frac{m\omega_1}{8} (x^2 + y^2) + \frac{m\omega_z}{2} z^2 \quad . \quad (3.19)$$

This equation consists of three harmonic oscillators with a coupling term, which is proportional to the canonical angular momentum in the z-direction. However, with a canonical transformation the equations of motion can be decoupled. Defining new generalized coordinates and momenta by

$$\begin{aligned} q_+ &= \frac{1}{\sqrt{2}} \left(\sqrt{\frac{m\omega_1}{2}} x - \sqrt{\frac{2}{m\omega_1}} p_y \right) \\ p_+ &= \frac{1}{\sqrt{2}} \left(\sqrt{\frac{m\omega_1}{2}} y + \sqrt{\frac{2}{m\omega_1}} p_x \right) \\ q_- &= \frac{1}{\sqrt{2}} \left(\sqrt{\frac{m\omega_1}{2}} x + \sqrt{\frac{2}{m\omega_1}} p_y \right) \\ p_- &= \frac{1}{\sqrt{2}} \left(-\sqrt{\frac{m\omega_1}{2}} y + \sqrt{\frac{2}{m\omega_1}} p_x \right) \\ q_3 &= \sqrt{m\omega_z} z \\ p_3 &= \frac{1}{\sqrt{m\omega_z}} p_z \quad , \end{aligned} \quad (3.20)$$

The Hamiltonian can be rewritten as

$$H = \frac{1}{2} \omega_+ (q_+^2 + p_+^2) - \frac{1}{2} \omega_- (q_-^2 + p_-^2) + \frac{1}{2} \omega_z (q_3^2 + p_3^2) \quad , \quad (3.21)$$

and is now fully decoupled in all three generalized coordinates (+, -, z). The harmonic oscillators for the motion in (+)- and z-directions have positive energy. The oscillator in the (-)-direction (magnetron motion) has negative energy, *i.e.* this motion is unstable such that the radius of the magnetron motion increases when it loses energy, *e.g.* after collisions with the buffer gas atoms. From the Hamiltonian the following equations of motion can be deduced:

$$\dot{q}_+ = +\omega_+ p_+ \quad \dot{p}_+ = -\omega_+ q_+ \quad (3.22a)$$

$$\dot{q}_- = -\omega_- p_- \quad \dot{p}_- = +\omega_- q_- \quad (3.22b)$$

$$\dot{q}_3 = +\omega_z p_3 \quad \dot{p}_3 = -\omega_z q_3 \quad . \quad (3.22c)$$

These equations can easily be solved and lead to the following solutions

$$q_+(t) = +\sqrt{m\omega_1}R_+ \cos \phi_+(t) \quad p_+(t) = -\sqrt{m\omega_1}R_+ \sin \phi_+(t) \quad (3.23a)$$

$$q_-(t) = +\sqrt{m\omega_1}R_- \cos \phi_-(t) \quad p_-(t) = +\sqrt{m\omega_1}R_- \sin \phi_-(t) \quad (3.23b)$$

$$q_3(t) = +\sqrt{m\omega_z}Z \cos \phi_z(t) \quad p_3(t) = -\sqrt{m\omega_z}Z \sin \phi_z(t) \quad (3.23c)$$

with the “angle variables” given by

$$\begin{aligned} \phi_+(t) &= \omega_+ t + \alpha_+ \\ \phi_-(t) &= \omega_- t + \alpha_- \\ \phi_z(t) &= \omega_z t + \alpha_z \quad . \end{aligned} \quad (3.24)$$

The solution of the equations of motion given by equations (3.23) shows, via the “angle variables” $\phi_k(t)$, that we are dealing with a multiply periodic system. Considering the $\phi_k(t)$ as new canonical coordinates, their canonically conjugate momenta are the so-called “action variables”. These are constants of the motion defined by

$$J_+ = \frac{1}{2\pi} \oint p_+ dq_+ \quad (3.25a)$$

$$J_- = \frac{1}{2\pi} \oint p_- dq_- \quad (3.25b)$$

$$J_z = J_3 = \frac{1}{2\pi} \oint p_3 dq_3 \quad , \quad (3.25c)$$

with the integral extended over one period of the respective oscillator. The contour integration must be performed in the same sense in which the system follows its phase space trajectory (anticlockwise for the magnetron oscillator, clockwise for the two other oscillators). The equations of motion imply

$$J_+ \geq 0, \quad J_- \leq 0, \quad J_z \geq 0 \quad . \quad (3.26)$$

Using eqs. (3.23), the integrals in eqs. (3.25) can be evaluated providing a connection between the action variables and the orbital amplitudes R_+ , R_- and Z ,

$$J_+ = \frac{1}{2} m \omega_1 \cdot R_+^2 \quad J_- = -\frac{1}{2} m \omega_1 \cdot R_-^2 \quad J_z = \frac{1}{2} m \omega_z \cdot Z^2 \quad . \quad (3.27)$$

This allows us to rewrite the Hamiltonian in terms of the new variables

$$H = \omega_+ J_+ + \omega_- J_- + \omega_z J_z \quad , \quad (3.28)$$

which leads to the following equations of motion ($k = +, -, z$)

$$\frac{d}{dt} \phi_k = \dot{\phi}_k = \frac{\partial H}{\partial J_k} = \omega_k \quad (3.29)$$

$$\frac{d}{dt} J_k = \dot{J}_k = -\frac{\partial H}{\partial \phi_k} = 0 \quad . \quad (3.30)$$

3.2 Inclusion of Additional Forces in the Model

Inside REXTRAP the stored ions are cooled via collisions with the buffer gas atoms. As mentioned in the previous section the magnetron motion of the particles is unstable. Therefore in addition an excitation of the particles via an external rf-field is necessary to reduce the radii of the stored particles. In the following sections a mathematical prescription for these effects is given which is afterwards included in our description of the Penning trap. The formalism was developed by M. Kretzschmar [Kre92b] and applied to the buffer gas cooling process by A. Kohl [Koh99].

In general we are interested in the time development of the Hamiltonian. The undisturbed Hamiltonian is given by

$$H = \vec{\omega} \cdot \vec{J} \quad \text{with} \quad \vec{\omega} = (\omega_+, \omega_-, \omega_z) \quad \text{and} \quad \vec{J} = (J_+, J_-, J_z) \quad . \quad (3.31)$$

When the potential for excitation or damping is “switched on” for a certain time, the Hamiltonian no longer remains constant in time. It has to be extended to include an additional time-dependent part, *i.e.* the energy of the system changes with the time. After the potential is switched off one immediately gets the Hamiltonian of an unperturbed system. The Hamiltonian before and after the perturbation consists only of eigenfrequencies ω and action variables J . The eigenfrequencies must remain the same before and after the perturbation, hence the action variables change from J (before perturbation) to J' (after perturbation). The time-dependence of J' (during perturbation) is directly related to the time-dependence of the potential energy:¹

$$\vec{\omega} \cdot \dot{\vec{J}}' = \frac{d}{dt'} V(x', y', z', t') = \frac{d}{dt'} V(\phi', J', t') \quad . \quad (3.32)$$

This relation is used in the following sections to include the effect of additional forces.

3.2.1 Frictional Damping

The damping of the ion motion is realized by a buffer gas introduced into the Penning trap. The damping can be described to a good approximation by a velocity dependent ansatz

$$\vec{F} = -\delta \vec{v} \quad . \quad (3.33)$$

The damping coefficient can be deduced from the theory of ion mobility in gases as:

$$\delta = \frac{q}{M_{ion}} \cdot \frac{p/p_N}{T/T_N} \quad . \quad (3.34)$$

The value M_{ion} is the reduced ion mobility coefficient which is tabulated for different ion species and gases in [Ell76], [Ell78], [Ell84], [Vie95]. The value p is the buffer gas

¹To simplify the notation the following has been used: $\Phi(J, \phi, \omega) = \Phi(J_+, J_-, J_z, \phi_+, \phi_-, \phi_z, \omega_+, \omega_-, \omega_z)$.

pressure in units of the standard pressure $p_N = 1013.25$ mbar and T is the temperature of the gas in units of the standard temperature $T_N = 273.16$ K. The dissipated power of an ion in a gas is

$$P_d = \frac{d}{dt} \left(-\delta \int \vec{v} \cdot d\vec{s} \right) = -\delta \dot{v}^2 \quad . \quad (3.35)$$

The damping of the buffer gas leads to a change in the action variables:

$$\vec{\omega} \cdot \dot{\vec{J}} = -\delta \dot{v}^2 \quad , \quad (3.36)$$

in which the square of the velocity can be deduced from the equations of motion. Neglecting high frequency terms one obtains

$$\dot{v}^2 \approx \dot{R}_+^2 + \dot{R}_-^2 + \dot{Z}^2 \cos^2 \omega_z t + \omega_+^2 R_+^2 + \omega_-^2 R_-^2 + \omega_z^2 Z^2 \sin^2 \omega_z t \quad . \quad (3.37)$$

For low damping, *i.e.* for low buffer gas pressure, the time dependent change of the radii can be neglected compared to the radial velocities. The square of the velocity can now be expressed in terms of these action variables (eq. 3.27)

$$\dot{v}^2 \approx \omega_+^2 R_+^2 + \omega_-^2 R_-^2 + \omega_z^2 Z^2 \sin^2 \omega_z t = \frac{2\omega_+^2}{m\omega_1} J_+ - \frac{2\omega_-^2}{m\omega_1} J_- - \frac{2\omega_z}{m} J_z \sin^2 \omega_z t \quad , \quad (3.38)$$

thus insertion of eq. (3.38) into eq. (3.36) yields

$$\vec{\omega} \cdot \dot{\vec{J}} = -\frac{2\delta\vec{\omega}}{m} \cdot \begin{pmatrix} \frac{\omega_+}{\omega_1} J_+ \\ -\frac{\omega_-}{\omega_1} J_- \\ J_z \sin^2 \omega_z t \end{pmatrix} \quad . \quad (3.39)$$

Using variable separation one obtains the following solution:

$$J_+(t) = J_+(0) \cdot e^{-\frac{2\delta}{m} \frac{\omega_+}{\omega_1} t} \quad (3.40a)$$

$$J_-(t) = J_-(0) \cdot e^{+\frac{2\delta}{m} \frac{\omega_-}{\omega_1} t} \quad (3.40b)$$

$$J_z(t) = J_z(0) \cdot e^{-\frac{\delta}{m} t + \frac{\delta}{2m} \frac{1}{\omega_z} \sin 2\omega_z t} \quad . \quad (3.40c)$$

Since $\omega_+ \gg \omega_z \gg \omega_-$ the cyclotron motion experiences the strongest damping. The damping of the axial motion is weaker. The magnetron motion on the other hand is not damped, its radius increases instead. The time constant of this increase is much smaller than for the other two motions.

One detail which has to be mentioned is the decrease of the resonance frequency for a damped oscillator. With the inclusion of additional forces we made the assumption that these forces are “switched on” for only a certain time. Afterwards we have again the unperturbed motion with the original eigenfrequencies but with different values of the action variables. In the case of damping by buffer gas the perturbation remains active at all times, *i.e.* the eigenfrequencies differ from the unperturbed

case. An exact calculation in the case of damping shows, that for realistic values for a Penning trap with buffer gas cooling, the shift of the eigenfrequencies is very small and can be neglected (see Appendix B.1).

Consideration of eq. (3.40) shows, that the cyclotron motion will be cooled down to radius zero in the limit of endless time. If the magnetron and the cyclotron motions are coupled by rf-fields (see Section 3.2.3), both motions can be cooled down to zero radius. This problem arises due to the use of the speed dependent ansatz, which neglects the finite temperature of the gas. Under real conditions the particle motion can only be cooled down to the gas temperature. The correct behaviour can be achieved by using collisions with the buffer gas atoms instead of the speed dependent ansatz.

3.2.2 Excitation with RF-Fields

Excitation of the ion motion in a Penning trap is achieved by applying dipole or quadrupole rf-fields to the trap electrodes. In the following the inclusion of an explicit time-dependent potential in our model is discussed. As a starting point the potential has to be re-written in terms of the action variables. It can then be separated into an explicit time-dependent term and a part which depends on the coordinates. This part can then be represented in terms of its Fourier components:

$$V(\phi, \mathbf{J}, t) = \mathbf{F}(t) \cdot V(\phi, \mathbf{J}) = \mathbf{F}(t) \cdot \sum_n A_n(\mathbf{J}) e^{i\vec{n} \cdot \vec{\phi}} \quad , \quad (3.41)$$

with the time-dependent part of the potential expressed as

$$\mathbf{F}(t) = \cos(\omega_{\text{rf}} t) = \frac{1}{2} \cdot \left(e^{i\omega_{\text{rf}} t} + e^{-i\omega_{\text{rf}} t} \right) \quad . \quad (3.42)$$

The value $n = (n_+, n_-, n_z)$ is the n -tuple of the vector \vec{n} , which arranges the Fourier representation in order of increasing harmonics of the angle variables. Together with eq. (3.32) one obtains the following equation:

$$\begin{aligned} \vec{\omega} \cdot \dot{\vec{J}}' &= \frac{d}{dt'} V(\phi', \mathbf{J}', t') = V(\phi', \mathbf{J}') \cdot \frac{d}{dt'} \mathbf{F}(t') \\ &= \omega_{\text{rf}} \cdot V(\phi', \mathbf{J}') \cdot f(t') = \vec{\omega} \cdot \vec{a} \cdot V(\phi', \mathbf{J}') \cdot f(t') \quad , \end{aligned} \quad (3.43)$$

where we have used the simplifications $\omega_{\text{rf}} \cdot f(t') = \frac{d}{dt'} \mathbf{F}(t')$ and $\vec{\omega} \cdot \vec{a} = \omega_{\text{rf}}$. This differential equation has no explicit solution. We look for an approximate solution by using the Taylor expansion of the coordinate-dependent part of the excitation potential:

$$\begin{aligned} V(\phi', \mathbf{J}') &= V(\phi', \mathbf{J}) + (\vec{J}' - \vec{J}) \cdot \vec{\nabla}_{\mathbf{J}} V(\phi', \mathbf{J}) + \dots \\ &= \sum_n (A_n(\mathbf{J}) + \Delta \vec{J}' \cdot \vec{\nabla}_{\mathbf{J}} A_n(\mathbf{J}) + \dots) \cdot e^{i\vec{n} \cdot \vec{\phi}'} \quad . \end{aligned} \quad (3.44)$$

One starts by integrating the equation (3.43) over the excitation time T :

$$\Delta \vec{J}' = \int_0^T \vec{a} \cdot V(\phi', \mathbf{J}') \cdot f(t') dt' \quad . \quad (3.45)$$

Insertation of the first two terms of the Taylor expansion into (3.45) results in the following equation:

$$\Delta\vec{J}' = \int_0^T \vec{a} \cdot \sum_n (A_n(\mathcal{J}) + \Delta\vec{J}' \cdot \vec{\nabla}_{\mathcal{J}} A_n(\mathcal{J})) \cdot e^{i\vec{n} \cdot \vec{\phi}'} \cdot f(t') dt' \quad . \quad (3.46)$$

Recursive insertation of $\Delta\vec{J}'$ and calculation of the average over all phases of ϕ' leads to the following surviving term:

$$\langle \Delta\vec{J}' \rangle_{\text{phases}} = \left\langle \int_0^T \vec{a} \cdot \sum_n \left(\int_0^T \vec{a} \cdot \sum_m A_m(\mathcal{J}) e^{i\vec{m} \cdot \vec{\phi}'} \cdot f(t') dt' \right) \cdot \vec{\nabla}_{\mathcal{J}} A_n(\mathcal{J}) e^{i\vec{n} \cdot \vec{\phi}'} \cdot f(t') dt' \right\rangle \quad , \quad (3.47)$$

because the angle variables in the exponent cancel themselves for $\vec{m} + \vec{n} = 0$. Taking into account the relation $A_{-n} = A_n^*$ one obtains

$$\begin{aligned} \langle \Delta\vec{J}' \rangle_{\text{phases}} &= \frac{1}{2} \sum_n \vec{a} \cdot (\vec{a} \cdot \vec{\nabla}_{\mathcal{J}}) \cdot |A_n(\mathcal{J})|^2 \cdot \left| \int_0^T f(t') \cdot e^{i\vec{n} \cdot \vec{\phi}'} dt' \right|^2 \\ &= \frac{1}{2} \sum_n \vec{a} \cdot (\vec{a} \cdot \vec{\nabla}_{\mathcal{J}}) \cdot |A_n(\mathcal{J})|^2 \cdot \tilde{F}^2(\vec{n} \cdot \vec{\omega}) \quad . \end{aligned} \quad (3.48)$$

The change of the action variable consists of a product of two terms, one which depends on the coordinates, and another which depends on the time dependency of the potential. The time-dependent part is the square of the Fourier transformation of the time-dependent part of the excitation potential. The excitation influences the action variables only if its frequency represents a linear combination of the eigenfrequencies $\vec{\omega} = (\omega_+, \omega_-, \omega_z)$. The value \vec{a} can then be replaced by \vec{n} . In the following sections the effect of a dipole and a quadrupole excitation will be discussed using the above results.

Excitation with an Azimuthal Dipole Field

Excitation with a dipole field can be used to excite an eigenmotion of an ion independent from the other eigenmotions. The excitation with an azimuthal dipole field can be used to excite the magnetron motion of the stored particle to increase its magnetron radius. This process is used for the mass-selective buffer gas cooling.

An azimuthal dipole field can be achieved by connecting a frequency generator to two parts of a split ring-electrode (see Fig. 3.5). The potential describing the dipole excitation can be expressed as:

$$\begin{aligned} V(x) &= k \cdot q \cdot U_d \cdot \frac{x}{\rho_0} \cdot \cos(\omega_{\text{rf}} t) \\ &= \frac{kqU_d}{2\rho_0} \sqrt{\frac{2}{m\omega_1}} \left(\sqrt{J_+} \cos(\phi_+) + \sqrt{|J_-|} \cos(\phi_-) \right) \cdot \left(e^{i\omega_{\text{rf}} t} + e^{-i\omega_{\text{rf}} t} \right) \\ &= \left(A_{1,0,0} e^{i\phi_+} + A_{-1,0,0} e^{-i\phi_+} + A_{0,1,0} e^{i\phi_-} + A_{0,-1,0} e^{-i\phi_-} \right) \cdot \left(e^{i\omega_{\text{rf}} t} + e^{-i\omega_{\text{rf}} t} \right) \quad , \end{aligned} \quad (3.49)$$

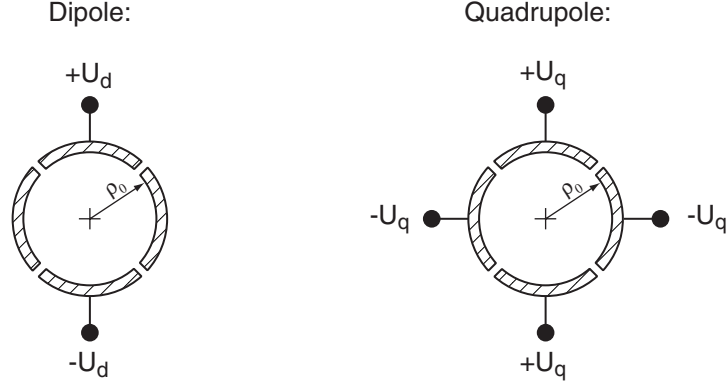


Fig. 3.5: Generating an azimuthal electric dipole (left diagram) or quadrupole (right diagram) field in the center part of a Penning trap by using a four-fold split centre electrode.

where U_d is the amplitude of the dipole excitation, ρ_0 is the radius of the ring-electrode and k is a parameter which corrects the deviation from the ideal dipole potential. The potential was rewritten in terms of the action variables which led to the coefficients

$$A_{\pm 1,0,0} = \frac{kqU_d}{4\rho_0} \cdot \sqrt{\frac{2}{m\omega_1}} \cdot \sqrt{J_+} \quad \text{and} \quad A_{0,\pm 1,0} = \frac{kqU_d}{4\rho_0} \cdot \sqrt{\frac{2}{m\omega_1}} \cdot \sqrt{|J_-|} \quad . \quad (3.50)$$

These coefficients can be used to calculate the change of the action variables together with eq. (3.48). Only $A_{0,\pm 1,0}$ has to be taken into account because of $\vec{n} \cdot \vec{\omega}$ in the Fourier transformed factor. The result of eq. (3.48) is

$$\begin{aligned} \langle \Delta J_- \rangle &= \frac{1}{2} q^2 \frac{\partial}{\partial J_-} \left(A_{0,1,0}^2(J_-) + A_{0,-1,0}^2(J_-) \right) \cdot \tilde{F}^2(\omega_-) \\ &= \frac{2}{m\omega_1} \left(\frac{kqU_d}{4\rho_0} \right)^2 \cdot \tilde{F}^2(\omega_-) \\ &= \frac{2}{m\omega_1} \left(\frac{kqU_d}{4\rho_0} \right)^2 \cdot \left(\frac{T}{2} \right)^2 \quad . \end{aligned} \quad (3.51)$$

The Fourier transformed $\tilde{F}(\omega_-)$ is equal to $T/2$ where T is the duration of the excitation (see Section B.2). The result can be rewritten to show the change of the magnetron radius:

$$\langle \Delta R_- \rangle = \frac{1}{m\omega_1} \cdot \frac{kq}{4\rho_0} \cdot U_d \cdot T \quad . \quad (3.52)$$

The increase of the magnetron motion is linearly dependent of the dipole amplitude and the duration of the excitation.

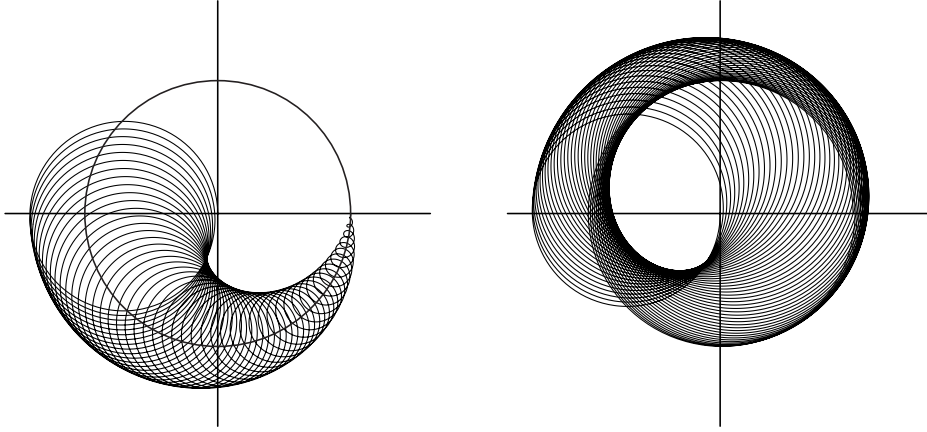


Fig. 3.6: Conversion from a pure magnetron to a pure cyclotron motion by quadrupole excitation at ω_c . The initial pure magnetron motion is shown as a circle in the left diagram. The right diagram shows the continuation of the left diagram which ends in a complete conversion to a pure cyclotron motion.

Excitation with an Azimuthal Quadrupole Field

An azimuthal quadrupole field can be achieved by connecting a periodic voltage to the parts of a four split ring–electrode (see Fig. 3.5). The potential describing the quadrupole excitation can be expressed as:

$$\begin{aligned}
 V(x,y,t) &= k \cdot q \cdot U_q \cdot \frac{x^2 - y^2}{\rho_0^2} \cdot \cos(\omega_{rf}t) \\
 &= \frac{kqU_q}{\rho_0 m \omega_1} \omega_{rf} \left(J_+ \cos(2\phi_+) - J_- \cos(2\phi_-) \right. \\
 &\quad \left. + 2\sqrt{J_+ |J_-|} \cos(\phi_+ + \phi_-) \right) \cdot \cos(\omega_{rf}t) \quad ,
 \end{aligned} \tag{3.53}$$

where U_q is the amplitude of the quadrupole excitation, ρ_0 is the radius of the ring–electrode and k is a parameter which takes the geometry of the electrode into account. Using this potential leads to the following differential equation:

$$\vec{\omega} \cdot \dot{\vec{J}} = - \frac{kqU_q}{\rho_0 m \omega_1} \omega_{rf} \left(J_+ \cos(2\phi_+) - J_- \cos(2\phi_-) + 2\sqrt{J_+ |J_-|} \cos(\phi_+ + \phi_-) \right) \cdot \sin(\omega_{rf}t) \quad . \tag{3.54}$$

In the following section the general solution in the case of azimuthal quadrupole excitation and frictional damping is given. The solution for quadrupole excitation can be deduced from the general solution in the case of damping \ll coupling ($\gamma \ll K$).

In the case of $\omega_{rf} = \omega_c = \omega_+ + \omega_-$ the field couples both radial plane eigenmotions. The coupling of these motions leads to a periodical conversion of energy between the corresponding harmonic oscillators, *i.e.* an initially pure magnetron motion with the amplitude $R_{-,0}$ is completely converted into a pure cyclotron motion with a radius $R_+ = R_{-,0}$ (Fig. 3.6). This conversion is a periodic process. It is similar to the motion

of two coupled pendula and can be compared to the so-called Rabi flipping in a two-level system. The conversion frequency is given by

$$\omega_{\text{conv.}} = \frac{kqU_q}{\rho_0^2 m \omega_1} . \quad (3.55)$$

A comprehensive discussion of the case of quadrupole excitation of stored ions can be found in the publication of M. König [Kön95]. The conversion of a pure magnetron into a pure cyclotron motion is used at precision mass spectrometers like ISOLTRAP [Bol96, Koh99] to determine the true cyclotron frequency $\omega_c = B \cdot q/m$. Due to the simple relation between the mass and the true cyclotron frequency a precise measurement of the latter leads to a precise determination of the mass. With the current setup of ISOLTRAP a precision of $\approx 10^{-7}$ for the mass determination can be achieved.

3.2.3 Quadrupole Excitation with Frictional Damping

To solve the problem of quadrupole excitation together with frictional damping one has to find a solution for the combined differential equation:

$$\begin{aligned} \vec{\omega} \cdot \dot{\vec{J}} &= -\delta \vec{v}^2 + \frac{d}{dt} V_{\text{quadr.}}(\phi, \mathbf{J}, t) \\ &= -\frac{2\delta \vec{\omega}}{m} \cdot \begin{pmatrix} \frac{\omega_+}{\omega_1} J_+ \\ -\frac{\omega_-}{\omega_1} J_- \\ J_z \sin^2 \omega_z t \end{pmatrix} - \frac{kqU_q}{\rho_0 m \omega_1} \cdot \omega_{\text{rf}} \cdot \left(J_+ \cos(2\phi_+) \right. \\ &\quad \left. - J_- \cos(2\phi_-) + 2\sqrt{J_+ |J_-|} \cos(\phi_+ + \phi_-) \right) \cdot \sin(\omega_{\text{rf}} t) . \end{aligned} \quad (3.56)$$

With the assumption that ω_{rf} is near the cyclotron frequency ω_c and neglecting terms of the order $\omega_{\text{rf}} + \omega_c$, ω_{rf} and ω_c (rotating wave approximation) the potential of the quadrupole excitation can be simplified to the following form:

$$\frac{d}{dt} V_{\text{quadr.}}(\phi, \mathbf{J}, t) = -\frac{kqU_q}{\rho_0 m \omega_1} \cdot \omega_{\text{rf}} \cdot \sqrt{J_+ |J_-|} \sin((\omega_{\text{rf}} - \omega_c) \cdot t + \alpha) , \quad (3.57)$$

with $\alpha = \alpha_+ + \alpha_-$ the sum of the phase shifts of the magnetron and the cyclotron motion against the quadrupole field. The axial motion is independent from the excitation, which means the solution given in eq. (3.40) for the z-motion is still valid. In the following only the two motions in the azimuthal plane will be discussed:

$$\begin{aligned} \dot{J}_+ &= -\gamma_+ \cdot J_+ - K \sin(\Delta\omega t + \alpha) \cdot \sqrt{J_+ |J_-|} \\ \dot{J}_- &= \gamma_- \cdot J_- - K \sin(\Delta\omega t + \alpha) \cdot \sqrt{J_+ |J_-|} , \end{aligned} \quad (3.58)$$

in which the definitions

$$\gamma_+ = \frac{2\delta}{m} \frac{\omega_+}{\omega_1} , \quad \gamma_- = \frac{2\delta}{m} \frac{\omega_-}{\omega_1} , \quad \Delta\omega = \omega_{\text{rf}} - \omega_c \quad \text{and} \quad K = \frac{\omega_{\text{rf}}}{\omega_c} \cdot \frac{kqU_q}{\rho_0^2 m \omega_1} , \quad (3.59)$$

were used. Rewriting the equations for the action variables in terms of the radii shows the time evolution of the magnetron and the cyclotron radius:

$$\begin{aligned}\dot{R}_+ &= -\gamma_+ \cdot R_+ - K \sin(\Delta\omega t + \alpha) \cdot R_- \\ \dot{R}_- &= \gamma_- \cdot R_- - K \sin(\Delta\omega t + \alpha) \cdot R_+ \quad .\end{aligned}\quad (3.60)$$

Using the definitions $R_+ = e^{-\gamma_+ t} A_+$, $R_- = e^{\gamma_- t} A_-$ and $\gamma = \gamma_+ + \gamma_-$ leads to the following equations:

$$\begin{aligned}\dot{A}_+ &= K \cdot e^{\gamma t} \cdot \sin(\Delta\omega t + \alpha) \cdot A_- \\ \dot{A}_- &= K \cdot e^{-\gamma t} \cdot \sin(\Delta\omega t + \alpha) \cdot A_+ \quad .\end{aligned}\quad (3.61)$$

A solution to this differential equation system can be found by extending the formula to complex functions and taking the imaginary part of the solution:

$$\begin{aligned}\dot{A}_+ &= -\Im \left\{ K \cdot e^{\gamma t} \cdot e^{-i(\Delta\omega t + \alpha)} \cdot A_- \right\} \\ \dot{A}_- &= \Im \left\{ K \cdot e^{-\gamma t} \cdot e^{i(\Delta\omega t + \alpha)} \cdot A_+ \right\} \quad .\end{aligned}\quad (3.62)$$

By forming the derivative the two coupled equations eq. (3.62) can be combined to one differential equation:

$$\ddot{A}_+ = -K^2 \cdot A_+ + (\gamma - i\Delta\omega) \cdot \dot{A}_+ \quad .\quad (3.63)$$

A solution to this equation can be found using the ansatz $A_+ = pe^{\eta t}$. It turns out, that this equation has four eigenvalues η , but for the case of resonance ($\Delta\omega = 0$) only two eigenvalues are of importance. These two values are:

$$\eta_{\pm} = \frac{1}{2}\gamma \pm \sqrt{\frac{1}{4}\gamma^2 - K^2} = \frac{1}{2}\gamma \pm \omega_r \quad .\quad (3.64)$$

One obtains the two solutions for resonance:

$$\begin{aligned}A_+ &= \Im \{ pe^{\eta_+ t} + qe^{\eta_- t} \} \\ A_- &= \Im \left\{ \frac{1}{K} e^{i\alpha - \gamma t} (p\eta_+ e^{\eta_+ t} + q\eta_- e^{\eta_- t}) \right\} \quad ,\end{aligned}\quad (3.65)$$

in which the parameters p and q can be varied to match the initial conditions of $R_+(0)$ and $R_-(0)$.

In the following the time evolution of the solution for an initial pure magnetron motion ($R_+(0) = 0$ and $R_-(0) = R$) with their dependence on the strength of the damping is discussed. The general solution for this initial condition is

$$\begin{aligned}A_+ &= \Im \left\{ \frac{RK}{\Im\{\omega_r e^{i\alpha}\}} \cdot e^{\frac{1}{2}\gamma t} \cdot \sinh(\omega_r t) \right\} \\ A_- &= \Im \left\{ \frac{R}{\Im\{\omega_r e^{i\alpha}\}} \cdot e^{\frac{1}{2}\gamma t + i\alpha} \cdot \left(\frac{1}{2}\gamma \cdot \sinh(\omega_r t) + \omega_r \cdot \cosh(\omega_r t) \right) \right\} \quad .\end{aligned}\quad (3.66)$$

Damping > Coupling:

In the case of $\frac{1}{2}\gamma > K$ the general solution for the radii is:

$$\begin{aligned} R_+ &= 0 \\ R_- &= e^{\gamma_- t} \cdot A_- = \frac{R}{\omega_r} \cdot e^{\gamma_- t} \cdot e^{-\frac{1}{2}\gamma t} \cdot \left(\frac{1}{2}\gamma \cdot \sinh(\omega_r t) + \omega_r \cdot \cosh(\omega_r t) \right) . \end{aligned}$$

The motion will stay a pure magnetron motion without any cyclotron motion. The radius of the magnetron motion can increase or decrease as well as remain constant depending on the ratio of damping to coupling.

Damping = Coupling:

In this case the strength of the damping is equal to the coupling ($\frac{1}{2}\gamma = K$) and the solutions for the radii are:

$$\begin{aligned} R_+ &= e^{-\gamma_+ t} \cdot A_+ = R \cdot e^{-\gamma_+ t} \cdot \sinh\left(\frac{1}{2}\gamma t\right) \\ R_- &= e^{\gamma_- t} \cdot A_- = R \cdot e^{-\gamma_+ t} \cdot \cosh\left(\frac{1}{2}\gamma t\right) \end{aligned}$$

Assuming that $\gamma_+ \gg \gamma_-$ in the limit for $t \rightarrow \infty$ the two radii can be described by

$$R_{\pm} = R \cdot e^{-\frac{1}{2}\gamma_+ t} \Rightarrow 0 . \quad (3.67)$$

This is an aperiodic case where both motions are cooled down to zero in the shortest possible time. This condition should be reached for the mass-selective buffer gas cooling process.

Damping < Coupling:

In the case of $\frac{1}{2}\gamma < K$ the solution for the magnetron and cyclotron radius is:

$$\begin{aligned} R_+ &= e^{-\gamma_+ t} \cdot A_+ = \frac{RK}{\bar{\omega}_r \cos \alpha} \cdot e^{-\gamma_+ t} \cdot e^{\frac{1}{2}\gamma t} \cdot \sin(\bar{\omega}_r t) \\ R_- &= e^{\gamma_- t} \cdot A_- = \frac{R}{\bar{\omega}_r} \cdot e^{\gamma_- t} \cdot e^{-\frac{1}{2}\gamma t} \cdot \left(\frac{1}{2}\gamma \cdot \sin(\bar{\omega}_r t) + \bar{\omega}_r \cdot \cos(\bar{\omega}_r t) \right) , \end{aligned}$$

with

$$\bar{\omega}_r = -i\omega_r = \sqrt{K^2 - \frac{1}{4}\gamma^2} . \quad (3.68)$$

In the limit $t \rightarrow \infty$ the behaviour of the two radii is:

$$R_{\pm} \sim e^{-\gamma_+ t} \Rightarrow 0 . \quad (3.69)$$

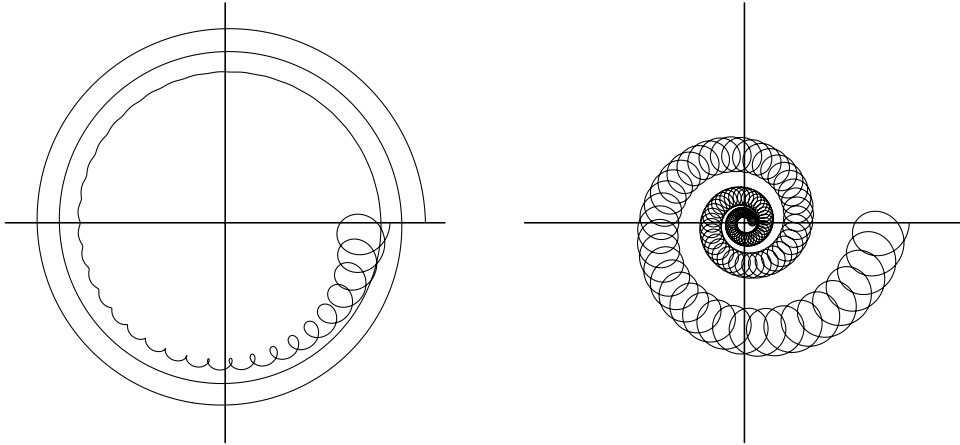


Fig. 3.7: *Effect of the frictional damping with and without coupling by an azimuthal quadrupole field. The left diagram shows the effect of frictional damping without coupling of the motions. An initial cyclotron motion is cooled down while the magnetron radius increases with time. In the right diagram the two motions are coupled via the true cyclotron frequency ω_c . Energy from the magnetron motion is transferred to the cyclotron motion which is cooled down. The net effect is a decrease of both radii which brings the particles to the center.*

In the special case of no damping ($\gamma = 0$) one gets a periodic conversion between the two motions:

$$\begin{aligned} R_+ &= \frac{R}{\cos \alpha} \cdot \sin(\bar{\omega}_r t) \\ R_- &= R \cdot \cos(\bar{\omega}_r t) \quad . \end{aligned}$$

The result expressed in terms of the action variables can be written as:

$$\begin{aligned} J_+ &= \frac{J}{\cos^2 \alpha} \cdot \sin^2(\bar{\omega}_r t) \\ J_- &= J \cdot \cos^2(\bar{\omega}_r t) \quad . \end{aligned}$$

3.3 Multiple-Particle Theory

The results obtained using the formalism in the preceding sections, are strictly speaking only valid in the case of a single ion stored in a Penning trap. In the case of two or more stored ions the Coulomb interaction between these particles has to be taken into account.

The Coulomb interaction of the charged ions shows up with two effects in the description of the behaviour of stored ions in a Penning trap:

- The electric field of the ions changes the electric potential produced by the trap electrodes (space-charge).

- The Coulomb repulsion force between the ions changes the motion of the particles and extends the ion cloud.

An analytic solution for the motion of charged particles in a Penning trap exists only for two particles [Bau93] without buffer gas and rf-excitation. For more than two ions one is forced to use numerical solutions from computer simulations. Under real conditions (10^6 ions and more) the necessary computation time at the given computer power exceeds usable limits. The results of experiments performed at REXTRAP (see Chapter 7) have shown deviations from the single particle theory beginning with 10^4 stored ions. Especially the shifts in the resonance frequencies of the ion motions cannot be understood with the known theory. Therefore it is indispensable to use simulations to find explanations for the observed behaviour.

One attempt to overcome the computational limits was made by D. Beck [Bec01]. He tried to reduce the number of particles included in the calculations by scaling the Coulomb force according to the following relation:

$$F_{C,\text{calc}} = \frac{n_{\text{stored}}}{n_{\text{calc}}} \cdot F_C \quad , \quad (3.70)$$

where F_C is the true Coulomb force, $F_{C,\text{calc}}$ is the scaled Coulomb force used in the calculation, n_{stored} is the number of particles stored in the trap and n_{calc} is the number of particles used in the calculations. The assumption was tested by putting an ion cloud in the trap centre and calculating its extent after 2 ms. The number of stored particles was 10^6 . The Coulomb force was scaled by different values ranging from 500 to 3000. The calculations resulted in nearly the same size of the ion cloud which can be seen as a proof of the used assumption.

After validating the used assumption, the formalism was used to calculate the resonance frequencies for dipole and quadrupole excitations with rf-fields for cesium ions in argon under similar conditions to REXTRAP: magnetic field strength $B = 3$ T, trap potential $U_0 = 100$ V, trap size $d = 41.6$ mm and a buffer gas pressure $p = 10^{-3}$ mbar. The used mobility constant for cesium ions in argon was $k_0 = 2$ cm²/Vs. The calculations were performed on PC clusters using around 40 CPU's. The computation time was around 8 weeks. The calculated resonance frequencies with respect to the ion number for dipole excitation can be seen in Figs. 3.8a and 3.8b. The frequencies were obtained by calculating the mean radius as a function of the excitation frequency. The central frequency results from a Gaussian fit to the calculated points.

As a next step cooling resonances for quadrupole excitations were calculated. The ions were excited for 20 ms. Two series with different initial distributions of the ion cloud were calculated; one with $FWHM_{r,z} = 5$ mm and another one with $FWHM_{r,z} = 15$ mm. The results are shown in Fig. 3.9. The observed resonance frequency shifts to higher values with increasing ion number. The comparison for the two different initial distributions shows an increase of the resonance frequency with increasing ion density. The frequency shifts are the same order of magnitude as observed in the

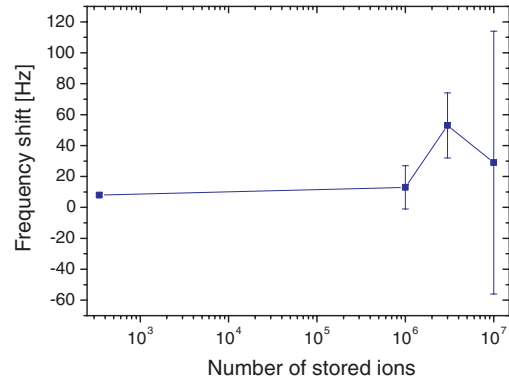
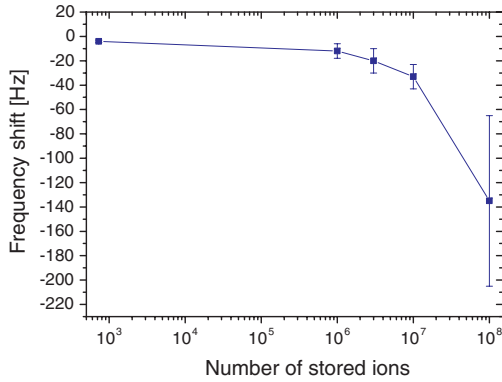


Fig. 3.8a: Shift of the magnetron frequency as a function of the ion number. **Fig. 3.8b:** Shift of the reduced cyclotron frequency as a function of the ion number.

experiments with REXTRAP (see Fig. 7.4). This evidently shows the feasibility of the performed simulations.

For a better understanding of the obtained results more systematic studies on the dependencies of the input parameters are necessary. The problem with these studies is the long computation time required for one single resonance. Different groups at various institutes have tried to adapt the formalism of plasma physics to ion clouds stored in Penning traps. A group at the University of California, San Diego have studied plasmas consisting exclusively of particles with a single charge sign confined in Penning traps. The theoretical prescription of the thermal equilibrium states of such plasmas can be found in [Dub99]. These calculations neither include buffer gas

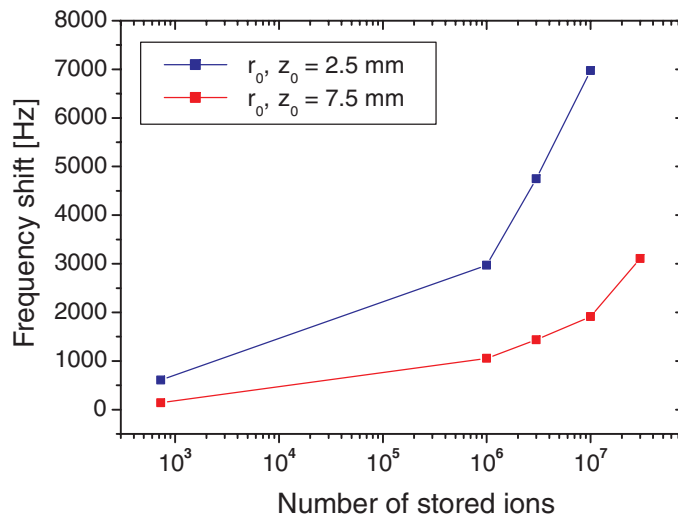


Fig. 3.9: Shift of the cooling resonance frequency as a function of the ion number for two different start distributions.

nor excitation with rf-fields. The results are therefore not directly applicable to the buffer gas cooling process used at REXTRAP. Nevertheless the developed formalism can be used as a starting point to develop a theory of buffer gas cooling in a Penning trap including the Coulomb interaction between the stored particles.

Chapter 4

REXTRAP Setup

4.1 Overview

The design of REXTRAP is defined by the planned performance of the REX-ISOLDE post accelerator together with the limits for the beam properties given by ISOLDE and by REXEBIS. Due to the small number of radioactive ions the efficiency of the device should be close to 100%. The acceptance should be sufficient to inject and capture as many ions from the ISOLDE beam as possible. The emittance of the ISOLDE beam is around $35 \pi \cdot \text{mm} \cdot \text{mrad}$ at 60 keV [Kug01]. The REXEBIS requires ion bunches with a maximum transversal emittance of the order of $10 \pi \cdot \text{mm} \cdot \text{mrad}$

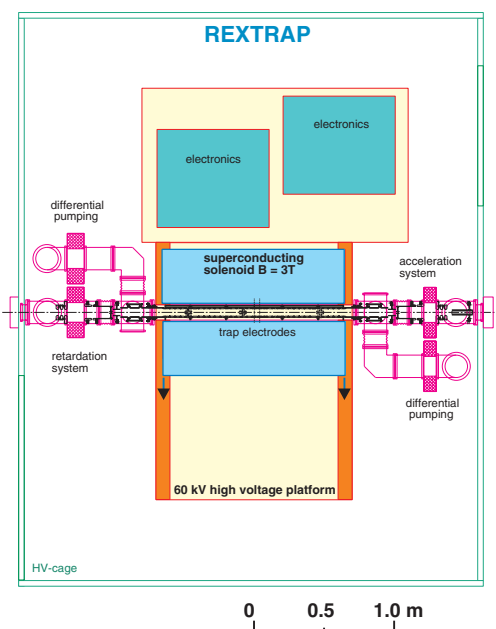


Fig. 4.1a: A top view of REXTRAP.

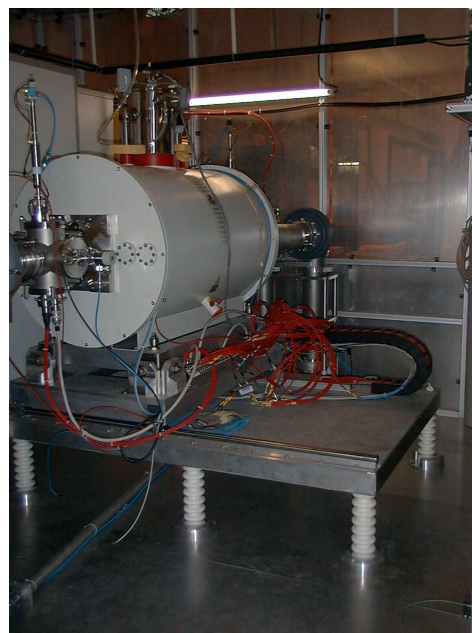


Fig. 4.1b: A picture of the REXTRAP-Magnet inside the Faraday-cage.

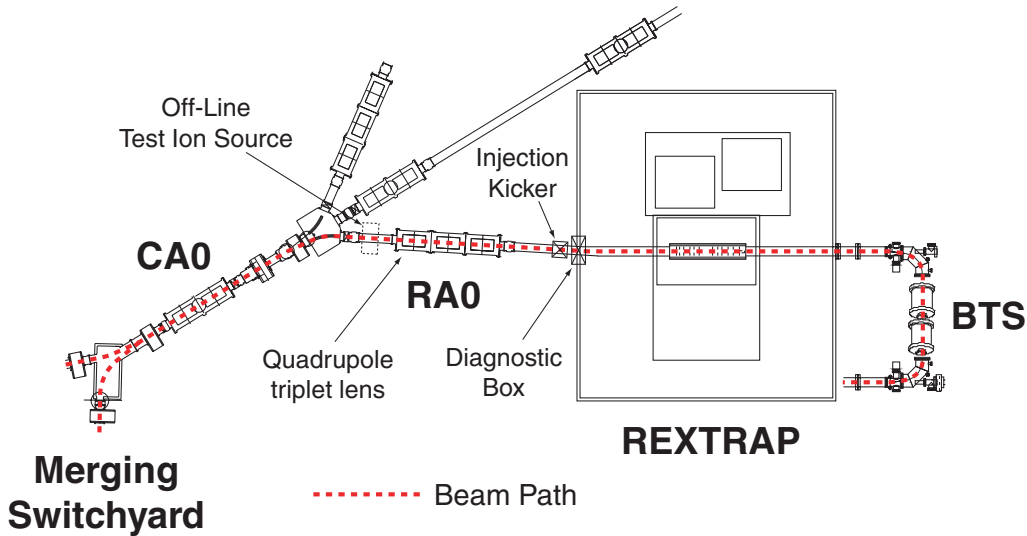


Fig. 4.2: *Beam Path from ISOLDE to REXTRAP. The ISOLDE beam is coming from either the GPS or the HRS through the merging switch yard into the ISOLDE central beam line (CA0). After the switch yard the REX-ISOLDE beam line (RA0) branches off.*

and a longitudinal emittance of $100 \mu\text{s} \cdot \text{eV}$ [Wen01]. To match the cycle time of the REXEBIS and the accelerator a repetition rate of 50 Hz should be reached [Hab00]. Finally a reliable and user-friendly operation has to be guaranteed for a device which is part of a complex accelerator.

In Fig. 4.1a a top view of the REXTRAP setup is shown. The superconducting solenoid together with two racks for the electronics reside on a high voltage platform. During operation the platform is set to 60 kV. Therefore the whole setup is surrounded by a Faraday cage. Fig. 4.1b shows a photograph of the REXTRAP magnet inside the high voltage cage. Ion optical elements in front and behind the magnet can be seen. The purpose of these elements is to retard the beam from 60 keV down to a few hundred eV and to provide focussing elements to prevent the beam from spreading out during the injection into the magnetic field.

The beam line to REXTRAP branches off from the central ISOLDE beam line at the switch yard after the section CA0. The short beam line between the switch yard and REXTRAP is named section RA0. This beam line includes a quadrupole triplet lens, an injection kicker and a standard ISOLDE diagnostic box consisting of a Faraday cup and a scanner. The injection kicker is necessary to correct a 3° missfit between the RA0 beam line and the axis of REX-ISOLDE. The axis of REX-ISOLDE was defined to be parallel to the wall of the ISOLDE hall. The kicker consists of two parallel plates for horizontal and vertical deflection, respectively. The vertical plates are used as a beam gate for REXTRAP. In this way the number of ions to be injected can be controlled. This is achieved by applying a pulsed high voltage to one of the vertical kicker plates. Between the switch yard and the quadrupole triplet

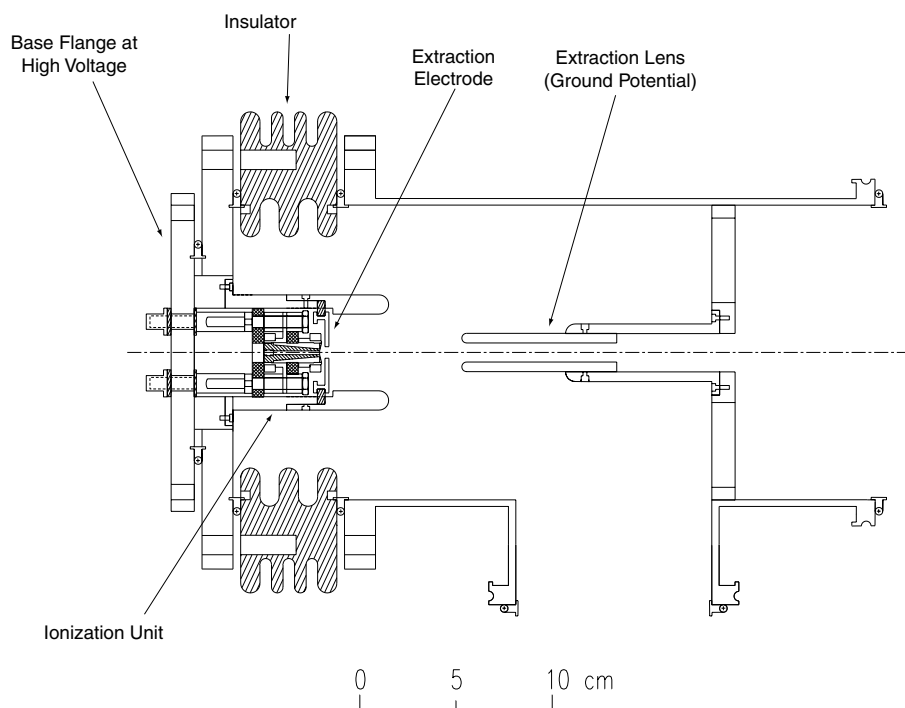


Fig. 4.3: A detailed drawing of the REXTRAP off-line test ion source.

lens an off-line test ion source can be introduced. The beam path from the ISOLDE merging switch yard to REXTRAP and afterwards through the transfer beam line to the REXEBIS is shown in Fig. 4.2.

4.2 Off-Line Test Ion Source

To be able to carry out measurements for testing and commissioning of REXTRAP, without the need to request stable beam from ISOLDE, a compact ion source for alkali ions has been developed. The concept of this surface ionization source is described in [Gha96].

A drawing of the ion source is shown in Fig. 4.3. The central part of this design is a conical graphite cylinder filled with zeolite material. Heating of the ion source is achieved by passing a high current (up to 75 A) along the cylinder. Due to its conical shape the part with the highest temperature is the front of the cylinder which is filled with tungsten wires to aid ionization. The back end is sealed with a removable plug so that the cylinder can easily be recharged. The base flange with the source mounted is isolated from the beam line and can be elevated to 65 kV above ground potential. For security reasons the whole setup is surrounded by a small Faraday cage. The ion source provides a beam with intensities typically of a few nA. The calculated emittance is of the order $10 \pi \cdot \text{mm} \cdot \text{mrad}$.

The size of the Faraday cage for the ion source is limited by the space between the

switch yard and the quadrupole lens of the RA0 section. Because of this restriction only up to 50 kV can be applied without sparking. Most of the experiments with REXTRAP were therefore performed at 30 keV beam energy. The ion source works very reliably and delivers ion beams of $^{133}\text{Cs}^+$, $^{39}\text{K}^+$ and $^{23}\text{Na}^+$ depending on the used zeolithe. Ion currents of a few nA could be produced for several months without refilling the zeolithe.

4.3 High Voltage Platform

REXTRAP resides on a high voltage platform which will be set to 60 kV during operation. On the platform the super-conducting solenoid and two 19"-racks filled with power supplies and electronics to control the trap are mounted. Fig. 4.1a shows the dimensions of the platform residing inside the Faraday cage. The platform is carried by ten insulators made of DELRIN[®] which can be seen in Fig. 4.1b.

The most massive part on the platform is the super-conducting magnet with its liquid helium and liquid nitrogen tanks. The magnet has a field strength of 3 T. It resides on two rails and can be moved perpendicular to the beam axis to allow access to the inner structure of the trap. The liquid helium tank has a capacity of 241 l and needs to be filled every 6 weeks. The liquid nitrogen tank has a capacity of 100 l and needs to be refilled once every week.

The two racks accommodate all the electronics and power supplies to control the voltages of the trap electrodes. Because of their position on the high voltage platform all equipment has to be controlled from outside the Faraday cage. All devices are therefore connected to the computer control system. The control signals are transferred to the platform by optical links. This will be discussed in more detail in Chapter 5. A more detailed description of the construction and installation work of the high voltage platform together with the Faraday cage as well as the security system can be found in [Sch01]. A description of the installation of the superconducting magnet can also be found there.

4.4 Trap Inner Structure

Fig. 4.4 shows the electrode structure of REXTRAP. The deceleration and the acceleration part are symmetric with respect to the trap center. They consist mainly of lenses and steering elements to achieve a reasonable injection and ejection of the ion beam. The beam is retarded from 60 keV down to a few keV in a relatively short distance. Ion optical elements are necessary to focus the beam into the magnetic field. On the ejection part the same effects occur with the abrupt acceleration to 60 keV. All electrodes in this part are made from stainless steel and are fixed inside of vacuum tubes and chambers. Except the kicker and steerer elements all electrodes are cylindrical shaped. The former ones consist of two pairs of parallel plates mounted

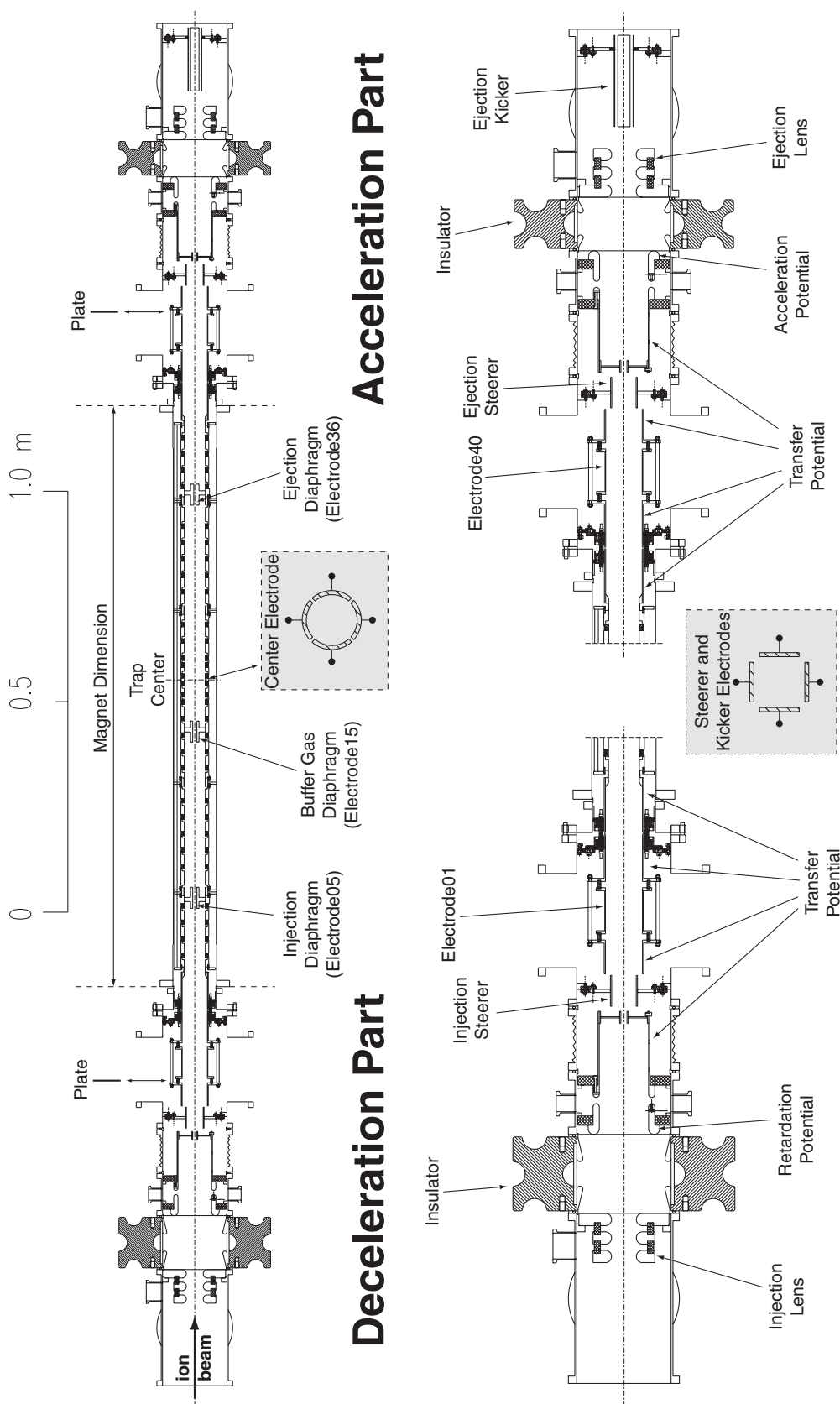


Fig. 4.4: The electrode structure of REXTRAP. The deceleration and the acceleration part with their ion optical elements for beam focusing are magnified. The names of the elements correspond to the device name used in the control system.

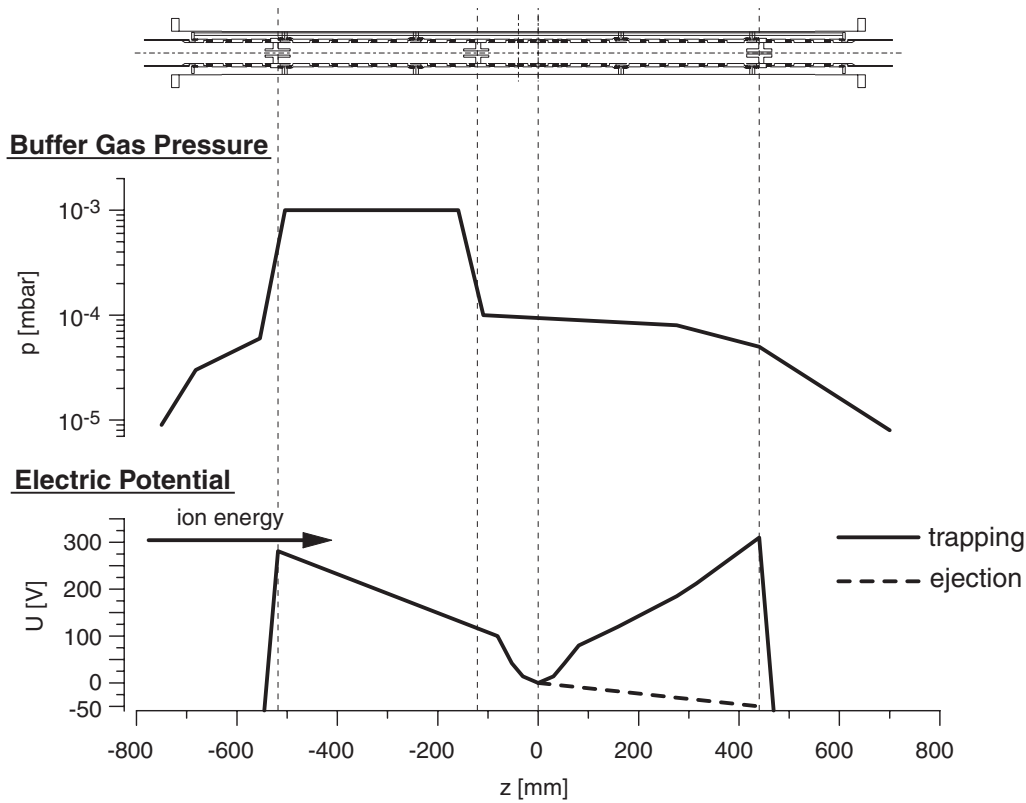


Fig. 4.5: *Distribution of the buffer gas pressure and the electric potential inside REXTRAP. At the top of the image the electrode structure is shown. The electric potential is given relative to the platform potential.*

in horizontal and vertical directions (see lower part of Fig. 4.4). This construction allows beam steering in the transversal direction.

The trap structure itself consists of about 30 electrodes with an inner diameter of 40 mm. The central electrode is split into four parts to be able to apply transversal electric dipole and quadrupole rf-fields to the trap center. The trap electrodes are made from oxygen free copper which is gold-plated to achieve good conductivity. Ceramic spacers (Macor) between the electrodes provide the necessary electrical insulation. The insulators fit into special slots at the front side of the electrodes. At the ends of the trap structure large Macor discs are mounted which carry plugs to provide an electric connection with the trap electrodes. The assembled sandwich-like structure is held together by an outside support structure. The overall length of the trap structure is about 1.3 m. Small aluminium wheels fixed to this support structure allow an easy insertion of the assembled trap into the vacuum tube of the magnet.

By applying voltages to the different trap electrodes a trap potential in the axial direction can be realized. A plot of the voltage profile used at REXTRAP is given in Fig. 4.5. The diagram shows how the extraction of the captured ions can be achieved

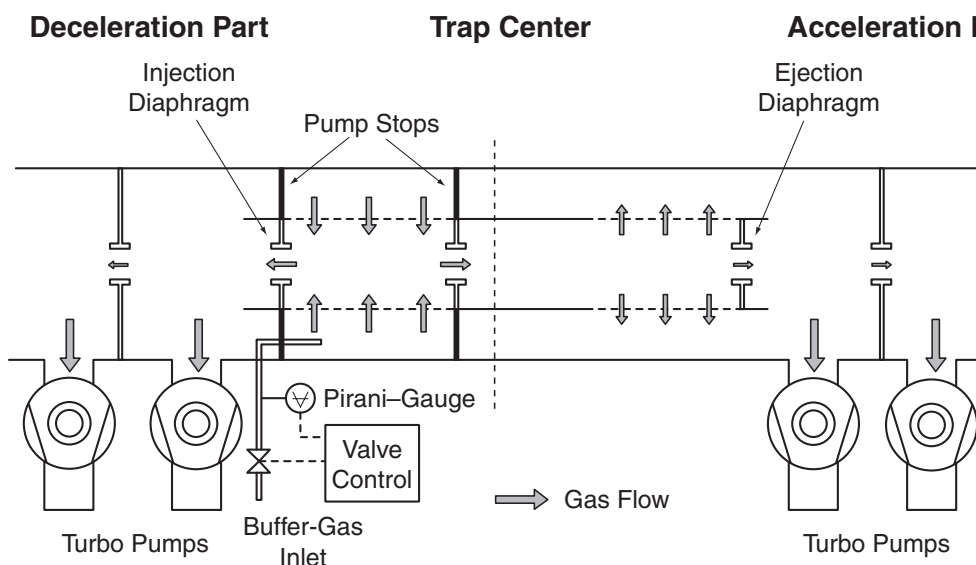


Fig. 4.6: Overview of the REXTRAP vacuum system. The gas flow is indicated by arrows.

by switching the electrodes to lower voltages, *i.e.* removing the potential barrier on the exit of the trap.

Between the Electrode01 and the transfer potential as well as between Electrode40 and the transfer potential, plates can be inserted via pneumatic feedthroughs (see Fig. 4.4). These plates allow to measure the beam current in the corresponding regions of REXTRAP. The plates are connected to pico-amperemeters (Keithley model 485) which can be controlled and read out remotely via the control system.

4.5 Vacuum System

An overview of the REXTRAP vacuum system and the buffer gas flow inside the trap can be seen in Fig. 4.6. Two turbo pumps (Alcatel 400 l/s) are installed on each side of the setup. The inner part of the trap is mainly pumped through the injection and ejection diaphragms. The combination of pump stops, diaphragms and perforated electrodes result in the gas flow shown in Fig. 4.6. In this way it is possible to achieve a buffer gas distribution as shown in Fig. 4.5. Additional diaphragms in the deceleration and acceleration parts allow a differential pumping of REXTRAP to achieve a reasonable vacuum in the connected beam lines.

4.5.1 Buffer Gas System

At REXTRAP noble gases are used as buffer gases. Up to now argon, neon and helium have been used. The gas is provided by a gas bottle which is connected from outside of the trap. The gas inlet is controlled by a needle valve connected to a pres-

sure controller unit (Balzers RME010 + RVG040). The pressure is read back by a Pirani pressure gauge (Alcatel P3C + CA111) which also provides the input for the valve controller unit. The buffer gas is fed into the inner part of the trap via a long teflon hose. The gas diffuses into the stopping region of the trap through perforated electrodes. In this region the buffer gas pressure is about one order of magnitude higher than in the trapping region (see Fig. 4.5). The electrodes at the ejection part of the trapping region are again perforated to achieve a pressure gradient versus the exit of the trap. The lower pressure in the ejection part is necessary to prevent re-heating of the ions during the extraction out of the trap.

The pressure value for the pressure controller unit can be set via an input voltage. It is also possible to read back a voltage corresponding to the actual pressure. The correlation between the voltage and the pressure can be approximated by the following equation

$$p = \exp(U_{\text{control}} \cdot U_0 - p_0) \quad [\text{mbar}] \quad . \quad (4.1)$$

The constants U_0 and p_0 for the different gases can be found in table 4.1. The possibility to control the buffer gas pressure by setting a voltage is used to control the buffer gas pressure remotely from the REXTRAP control system.

	U_0	p_0
He	1.158	13.912
Ne	1.250	14.053
Ar	1.301	14.177

Tab. 4.1: Constants used to calculate the buffer gas pressure for a given control voltage.

4.6 Operational Procedure of REXTRAP

To describe the operational procedures of REXTRAP the setup can be divided into the following three stages:

- Deceleration and Injection
- Stopping and Trapping
- Ejection and Acceleration .

In the following sections the three stages are discussed in detail. The naming of the different electrodes follows the description in Fig. 4.4.

4.6.1 Deceleration and Injection

In this section the incoming beam is retarded from its initial energy of 60 keV and injected into the region of high magnetic field. The beam is focused on a diaphragm by a lens system which is formed by the two gaps between the ground potential and the retardation potential and between the retardation potential and the first electrode of the transfer potential. A Einzel-lens formed by the Electrode01 and two electrodes

of the transfer potential together with the focusing effect of the converging magnetic field reduces the diameter of the incoming beam to be able to pass through the injection diaphragm. After this point the ions follow the parallel magnetic field lines which guide them to the central region of the trap. While entering the magnetic field the ion trajectory is not parallel to the magnetic field lines. Therefore a Lorentz force acts on the ions which results in a transfer of longitudinal energy into radial energy. This effect increases the longitudinal energy spread and has to be taken into account when setting the potential barrier which is applied to the injection diaphragm (referred to as Electrode05 in the control system).

4.6.2 Stopping and Trapping

The inner part of the trap between the injection and ejection diaphragm is divided into two sections separated by the buffer gas diaphragm. In the first part the buffer gas pressure is one order of magnitude higher than in the second part. The high buffer gas pressure ensures a sufficient energy loss to prevent the ions from passing again the potential barrier at the injection diaphragm. The pressure in the trapping region is lower in order to ensure a reasonable cooling performance and prevent a re-heating of the ions by collisions with the buffer gas during ejection out of the trap. The longitudinal motion of the ions is cooled by collisions with the buffer gas atoms (see Fig. 4.7). To cool the ion bunch in the radial direction it is exposed to a radio frequency field which is used for the rf-sideband cooling mechanism described in Chapter 3. After finishing the cooling procedure the potentials of the Electrode24 (trap center) to Electrode36 (ejection diaphragm) are switched to negative values (with respect to the trap center) in order to accelerate the ion bunch out of the trap.

4.6.3 Ejection and Acceleration

The ejection and acceleration section of REXTRAP is similar to the deceleration and injection section, except that the ions pass through in opposite direction. After passing the ejection diaphragm the ion pulse is focused by a Einzel-lens formed by the Electrode40 and two electrodes of the transfer potential. It follows another diaphragm after which the ion bunch is focused by a lens system which is formed by the last electrode of the transfer potential and the acceleration potential. Finally the ions are accelerated to 60 keV.

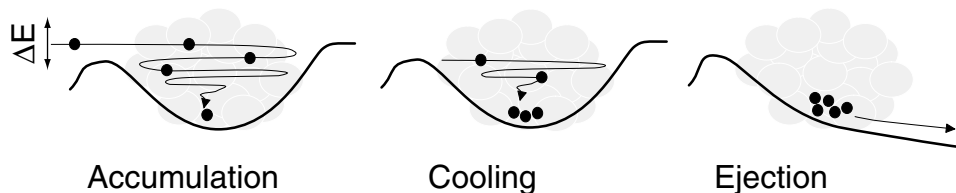


Fig. 4.7: Buffer gas cooling in longitudinal direction.

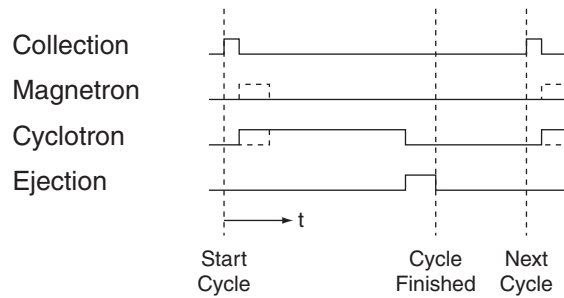


Fig. 4.8: Time structure of the REXTRAP operational cycle.

4.7 Operational Cycle of REXTRAP

The operational cycle of REXTRAP consists of three or four stages. The time structure of the cycle is shown in Fig. 4.8. In the collection stage the beam gate in front of the trap is opened and the ions can enter the trap. The length of the collection stage is determined by the intensity of the incoming beam. For normal operation it varies between a few microseconds and one millisecond. To clean the ion bunch of unwanted contaminations a cleaning step by excitation of the magnetron motion can be applied. By doing so the magnetron radius of all stored ions is increased. Via excitation with the cyclotron frequency only for ions with a certain charge-to-mass ratio the magnetron radius can be reduced (see Chapter 3). This cleaning procedure is rarely used at REXTRAP but can be used to eliminate unwanted contaminations, if necessary. In most cases during the experiments described in Chapter 7 only the cyclotron frequency was applied. This process can take up to 20 ms and more. It mainly determines the length of the REXTRAP operational cycle. After the desired cooling time the ions are ejected by lowering the electrodes of the exit part of the trap. Because of different rise times of the used high voltage amplifiers, different ejection pulses with slight delays ($\approx 10 \mu\text{s}$) in between are used. The time of flight for the ions to arrive at the detector after the trap is mass dependent. For $^{133}\text{Cs}^+$ ions it takes about $100 \mu\text{s}$ until they arrive at the detector (see TOF-spectra in Chapter 7). The time structure discussed in this section is realized at the REXTRAP setup by using the memory module which is explained in Section 5.2.4. The different pulses in Fig. 4.8 correspond to trigger pulses generated by the memory module. These trigger signals are used to control the devices which correspond to the respective step in the operational cycle. These devices are the beam gate for the collection, function generators for producing the magnetron and cyclotron frequency and the trap electrodes which are switched to lower voltages to eject the cooled ions.

Chapter 5

The REXTRAP Control System

5.1 Overview

The REXTRAP control system is based on a system developed at the university of Mainz for the control of the ISOLTRAP experiment (IS302) at CERN/ISOLDE and for the SMILETRAP experiment at the Manne Siegbahn Laboratory (Stockholm/Sweden). The system consists of a front-end computer (FEC) and a client PC which is connected to the FEC via Ethernet. The FEC is a single board computer with VME-interface based on a Motorola[®] 68K family processor. It runs under the real time operating system OS-9[®] from Microware Systems Corporation. The hardware elements (*e.g.* power supplies, frequency generators, MCA's, ...) which are to be controlled via the control system are connected to the FEC via common interfaces. Drivers exist for PROFIBUS[®], GPIB and others. The client programs require a Windows NT[®] (or higher) based standard PC.

The communication between the software on the client PC and the FEC takes place via a TCP/IP communication over an Ethernet connection. A communication protocol has been developed to achieve a fast and reliable communication between the two systems.

5.2 Hardware

As mentioned earlier nearly all parameters of REXTRAP have to be controlled via the control system. Two bus-systems are available at REXTRAP to control the various devices. For "intelligent" devices which need to be programmed or which have a large amount of data to transfer a GPIB (**G**eneral **P**urpose **I**nterface **B**us) is used. Simple devices like power supplies are connected to a fieldbus for which a PROFIBUS[®] system is used.

5.2.1 GPIB

Various “intelligent” devices are connected to the GPIB bus used at REXTRAP. This includes all the measuring devices such as the oscilloscope, the multi-channel scaler and the picoamperemeters. The “Memory” device which produces all the timing signals for REXTRAP and the frequency generators are also controlled via the GPIB bus. A few GPIB devices reside on the HV platform. To connect this bus segment to the other segment at ground potential an optical link interface from National Instruments is used. To connect the GPIB bus to the FEC a VME-bus interface card from Janz Electronic is used.

5.2.2 PROFIBUS

PROFIBUS[®] is a vendor-independent, open-communication fieldbus system used for automation in manufacturing and process control. The PROFIBUS[®] fieldbus technology is a cost-effective and reliable solution to achieve all the requirements for industrial automation and process control tasks [PRO]. It is used by a wide range of companies in various different applications. At CERN PROFIBUS[®] is the recommended fieldbus system for all controlling tasks. At REX-ISOLDE PROFIBUS[®] is not only used at REXTRAP but also for various other tasks. It is used together with a Siemens S7 CPU to control the vacuum system of the different sections. The low-level rf control for the linac resonators as well as the power supplies for the quadrupole magnets at REX-ISOLDE are also controlled via PROFIBUS[®] interfaces.

The topology of the PROFIBUS[®] used at REXTRAP consists of a bus master which determines the communication on the bus and a number of slave units which are equipped with DAC's, ADC's, digital input and output modules as well as serial interfaces. The PROFIBUS[®] communication is based on the RS485 protocol. The bus signals are transported via shielded twisted pair cables between the bus master and the slave units. This technology ensures simple and cost-efficient cabling and allows data transfer rates up to 1.5 MBit/s. The two PROFIBUS[®] slave units which are installed on the HV platform are connected to the bus on ground potential by an optical link system consisting of an optical link module and an optical link plug (both from Siemens) connected via a plastic fibre loop.

The bus is controlled by a VME-PROFI bus master card from Dorsch Mikrosystem. The card has its own CPU which unburdens the VME computer from handling the PROFIBUS[®] protocol. The communication between the VME computer and the VME-PROFI bus master card is achieved by a dual ported memory on the bus master card which is mirrored into the VME-bus memory [Sch01]. Five slave units are connected to the REXTRAP PROFIBUS[®] (one Siemens ET200M and four WAGO I/O system). Two slave units reside on the HV platform.

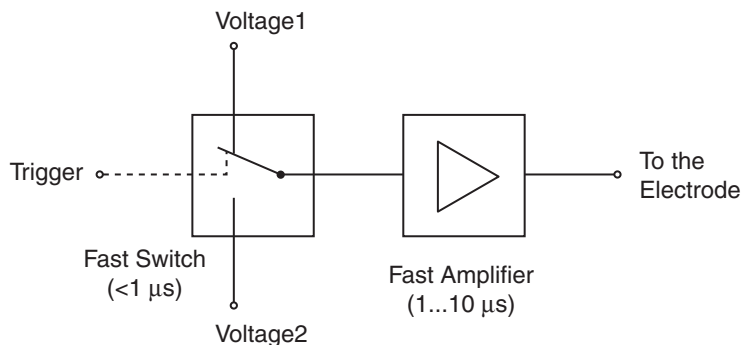


Fig. 5.1: *Fast Switching of Electrodes at REXTRAP.*

5.2.3 Fast Switching of Trap Electrodes

During the operational cycle of REXTRAP a number of potentials need to be switched at short intervals. This includes the trap electrodes at the exit part of the trap (see Chapter 4.4). The control system is not fast enough to achieve a switching time of a few microseconds required for a decent pulse shape. Therefore a different approach had to be found. To achieve the required goal a combination of fast CMOS analogue switches and fast high voltage amplifiers are used at REXTRAP. A block diagram of the used setup is shown in Fig. 5.1. The switch uses a TTL trigger signal to switch between two input voltages which are in the range of -10 to 10 V. The output signal from this switch is amplified by fast amplifiers with rise times of a few 100 V/ μs . As fast amplifiers modules from the Elektronik Labor of the University of Mainz and modules from Trek Inc. are used.

For the beam gate in front of the trap and for the kicker in front of the EBIS a different approach is used. Instead of switching the control voltages the high voltage from two power supplies is switched directly by a fast high voltage transistor switch from Behlke Electronic. This switch uses again a TTL input signal as a trigger pulse for switching.

5.2.4 Timing of the REXTRAP setup

The timing for the trap operation cycle as it is described in Chapter 4.6 is provided by TTL trigger signals. These signals are generated by a programmable logical pattern generator, the so-called memory module built by the Elektronik Labor of the University of Mainz. It has twelve TTL outputs which can be programmed independently. This module is programmed via the GPIB interface. The synchronisation with the processes running on the FEC is ensured via a digital I/O interface card with VME-bus interface from Janz Electronic. The trigger signals from the memory module are used to pulse the beam gate in front of the trap, the switched trap electrodes, the function generators which produce the rf signals applied to the trap electrodes and the various data acquisition devices (e.g. oscilloscope and the multi-channel scaler).

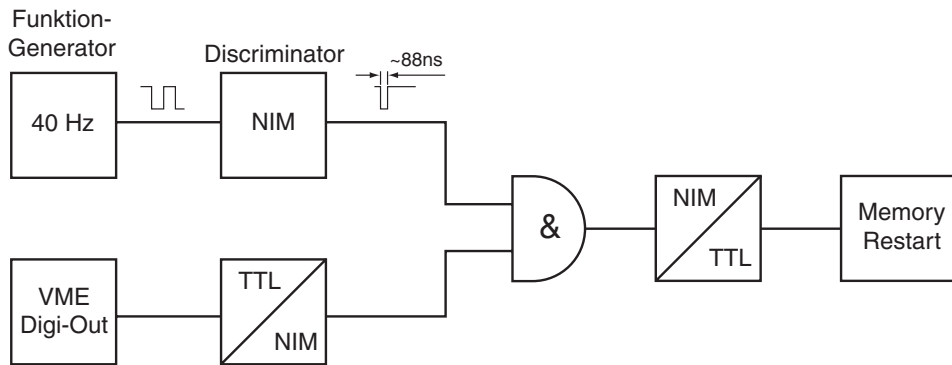


Fig. 5.2: Coupling of the REXTRAP timing to the REX-ISOLDE cycle pulse.

For pulsing devices residing on the HV platform a special optical link system for fast TTL pulses has been developed using optical transmitter and receiver components from Harting Elektronik [Sch01].

Until the REX-ISOLDE beam time in Nov. 2000 the time structure of REXTRAP was independent from the other parts of REX-ISOLDE. At this time the time structures of REXTRAP, REXEBIS and the linac had to be coupled. To achieve this a frequency generator was used to define the cycle time of the whole REX-ISOLDE setup. The time structure of REXTRAP had to be connected to this cycle. Fig. 5.2 shows a block diagram of the setup which is used to connect the REXTRAP time structure to the REX-ISOLDE cycle pulse. The signal coming from the frequency generator (Stanford Research model DS345) is fed into a discriminator which delivers short pulses of around 80 ns length. This pulse is combined with the digital output of the VME computer to start a new cycle of the memory module in coincidence with the REX-ISOLDE trigger. In this way the repetition rate of the ejection pulse of REXTRAP could be fixed to the REX-ISOLDE cycle. This is essential for the linac which has to run within a fixed cycle without interruption. As long as the overall time of the REXTRAP time structure is smaller than the cycle time of the REX-ISOLDE pulse the repetition rate of the REXTRAP ejection pulses is given by the REX-ISOLDE pulse. If the time of the REXTRAP time structure is longer only every second pulse can be used.

5.3 Software

5.3.1 FEC

The front end computer runs under the real time operating system OS-9[®] from Microware Systems corporation. OS-9[®] is a console based operating system with a UNIX-like user environment. The software modules were developed using Microware's Hawk[™] integrated development environment.

To achieve a high modularity and flexibility of the control system a high granu-

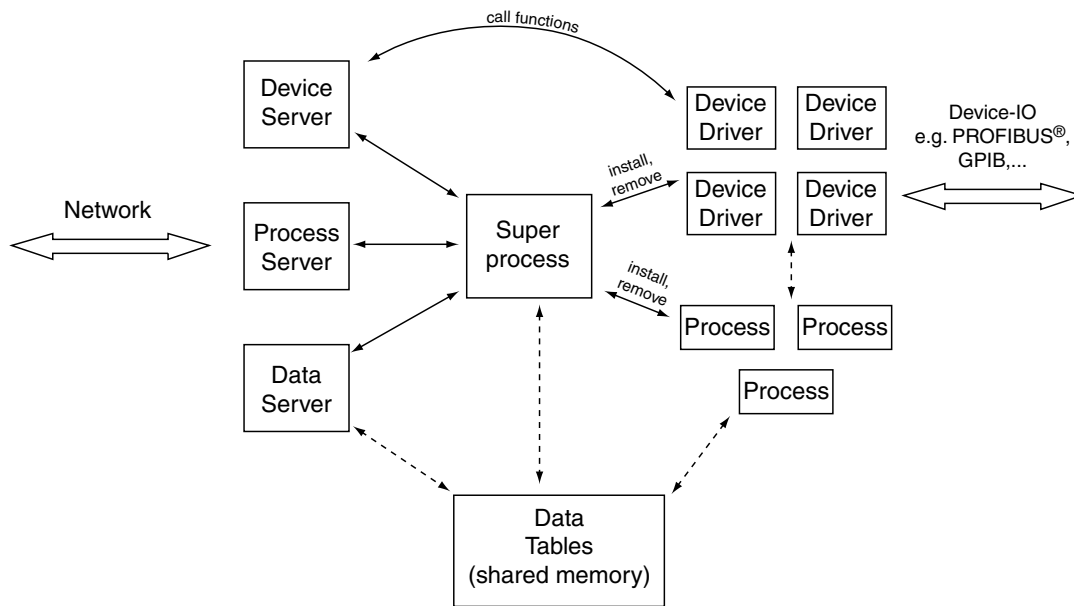


Fig. 5.3: The interplay of the different processes running on the FEC.

larity of the software modules had to be established, *i.e.* instead of one large program the system consists of a number of small software modules which run as separate processes and communicate with each other via a specifically developed IPC (Inter Process Communication). This IPC takes advantage of the features provided by OS-9[®] like the availability of shared memory modules as well as extensive signal and event handling mechanisms.

In Fig. 5.3 the different software modules which are running on the FEC and their relations are shown. The main process of this system is called 'Super'. This process is started after the operating system is loaded and remains running continuously. It creates and initializes the data tables required for the IPC. It provides a number of functions to install and remove device drivers and processes (a process is in this case a module which communicates with different devices to perform operational cycles of the apparatus).

The client side of the control system on the FEC consists of three different software modules which act as a link to the Super process. These three modules are called 'DevServer' (Device Server), 'ProcServer' (Process Server) and 'DataServer'. The Device Server turns over the request to install or remove a device to the Super process. In addition it provides an interface to the devices which enables the client program to execute functions provided by the device driver. Such functions are *e.g.* setting voltages, moving plates in and out or reading the actual beam current from a Faraday cup. The task of the Process Server is to install and remove processes and also to start, pause and stop these processes. The Data Server provides an interface to install and delete data tables (which are shared memory modules under OS-9[®]) as well as fill in or read back data from these tables. The information in these ta-

bles is used to hand over the configuration settings for a process which includes *e.g.* the devices to set for an operational cycle of the apparatus as well as to store the data acquired by a corresponding device driver for a MCA. These server processes are only started on demand by the client. A plug-in for the `inetd`-daemon listens on a reserved TCP/IP port on the FEC. The client program connects to this port and starts the required server process. This process is only valid as long as the network connection persists. In case of an abnormal termination of the connection the server process closes the connection, terminates and writes a message to the error handler (a special data table reserved for error messages).

Besides the control by a client program, a few programs exist on the FEC which allow the control of the functions of the devices from a shell window. It is possible to establish a telnet connection or a serial connection to the FEC and use these programs directly. This feature is mainly established for diagnostics or debugging of the different software modules.

The majority of the FEC software modules is written in C. A number of device drivers require subroutines written in 68K-assembler to directly address the corresponding hardware or to call special API-functions of OS-9[®] for which no C-language function call exists.

5.3.2 Client PC

For a user-friendly operation of the experiment, client programs running under Windows NT[®] have been developed. The programs are true 32-bit applications which are, for easier development, written in C++ using the Microsoft[®] MFC (Microsoft Foundation Classes) C++-Framework. As a development platform Microsoft[®] Visual C++ Version 6.0 was used. At present two client programs for the operation of REXTRAP are available. These programs will be presented in the next sections.

DevCon

One program is called 'DevCon' (Device Console). It communicates with the Device Server on the FEC. It allows the user to install and remove devices on the FEC. After the installation of a device it provides an interface to the functions of the corresponding driver. In this way it is possible to set all the parameters of REXTRAP out of one program. It is organised like a desktop showing all installed devices as small boxes. After double-clicking a device, respectively the box corresponding to the device, a dialog box is shown which allows the user to set and read back the parameters of the device. A screen-shot of the program during operation is shown in Fig. 5.4. All the device-dependent dialog boxes are written as small software components which are loaded on demand. Using this technique a large monolithic program could be avoided and also the development work to include new devices in the system could be reduced. The technique used to achieve this behaviour is the Microsoft[®] COM (Com-

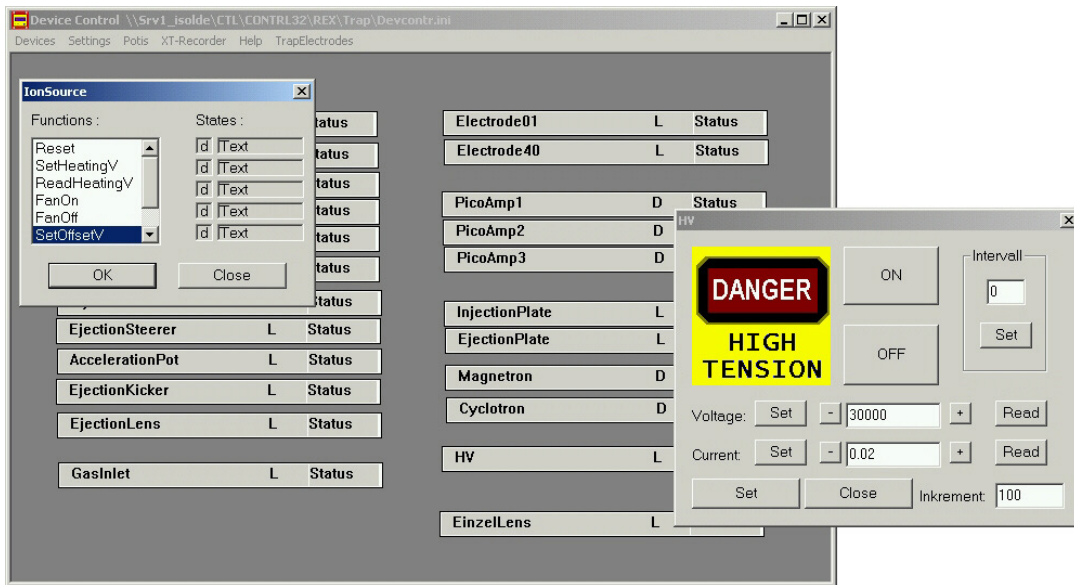


Fig. 5.4: DevCon program with dialog box for a High Voltage power supply.

ponent Object Model) interface, a set of API–functions to ease the development and communication between small software components.

DevCon is also used to control the various ion–optical elements of the transfer beam line. In the style of the 'Synoptic' program from the ISOLDE–control system the background of the DevCon desktop can be filled with a schematic picture of the beam line. The device boxes are degenerated to a simple text–box for the corresponding device. This results in a more intuitive operation for the user. A screenshot of this is shown in Fig. 5.5. In the same way the principle of DevCon could be adapted to control the electrode voltages of the REXTRAP electrodes. The corresponding device boxes are degenerated to circles which are connected with lines to show the trap voltages as a graph (Fig. 5.6).

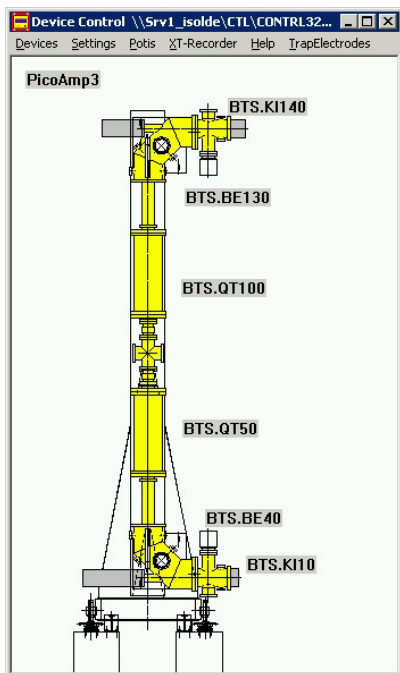


Fig. 5.5: DevCon program with a 'Synoptic'–like desktop.

RexControl

The second program 'RexControl' is based on the program 'MassMeasure' used at the ISOLTRAP experiment. Whereas the program 'DevCon' is mainly used to set static parameters of REXTRAP, the program 'RexControl' is used to control complete measurement or operation cycles of REXTRAP. RexControl does not communicate directly with the

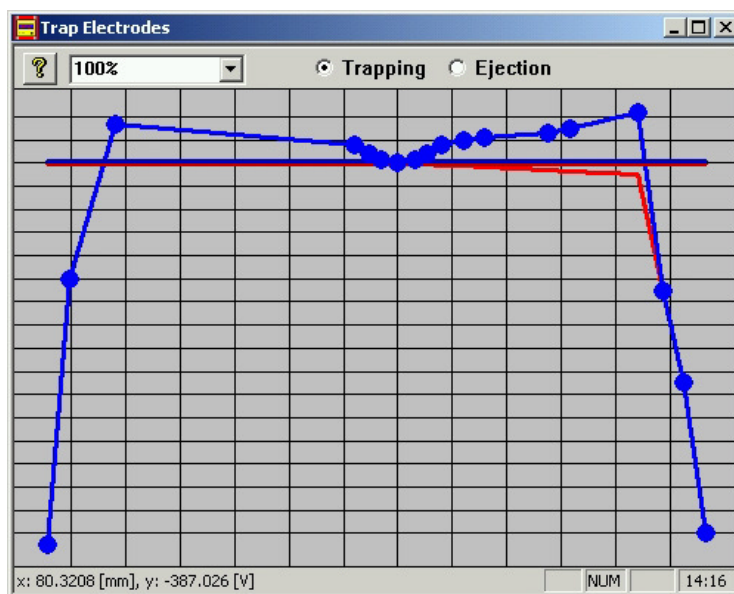


Fig. 5.6: Control of the trap electrodes with DevCon.

devices. Instead all the information necessary to perform an operation cycle (e.g. applied frequency, which MCA is to be used, parameter to be scanned, ...) is sent to the FEC as configuration information. This information is used by a process on the FEC called 'RexTrapControl' to control corresponding devices and read the acquired data after a measurement cycle is finished. This process is started and controlled by the RexControl program. To be able to do this the RexControl program communicates with the 'DataServer' and the 'ProcServer' on the FEC.

The time structure for the operation cycle is controlled via a so called 'Memory' module (see Section 5.2.4). It is connected to the FEC via the GPIB interface. RexControl provides an interface for programming this module. Using this interface the complete operation cycle can be defined via a Windows dialog box. RexControl is also able to read back the acquired data from a MCA as well as process and display this data. Together with the ability to scan certain parameters this feature is the key element performing measurements with REXTRAP.

In Fig. 5.7 the input dialog box for the RexControl program is shown. In this case a scan over the cyclotron frequency is performed. The data will be acquired via the device 'Scaler' (the multi-channel scaler). All the information entered in this form is sent to the FEC. After pressing the 'Start' button the process on the FEC starts controlling the measurement cycle of the trap. The acquired data is transferred to the RexControl program which evaluates and displays it. In Fig. 5.8 a typical view of the RexControl desktop is shown. In the lower part the TOF-spectrum of the ions is displayed (window 'Cnts vs TOF'). This diagram shows the acquired data. In the upper part the evaluated dependency on the scan parameter can be seen (windows 'Cnts vs Scan' and 'Acc. Cnts vs Scan'). This is achieved by summing over the channels in the

Scan

	device	function	center	--	+	step	unit
#1	Cyclotron	SetFrequency	1172000	5000	5000	100	Hz
#2	*EinzelLens	*SetVoltage	17500	500	500	50	*V

MemHandler

Device	Cycles
REXMemHandler	40

MCA

Device	Gate	#Channels	Pipse
Scaler	1	512	0

Memory

Device	PULS1
MemREX1	<input type="checkbox"/>

Specials

	device	function	value	unit
1	*			
2	*			
3	*			
4	*			
5	*			

2D Scan

scan1 FREQU1

scan2 Noscan

specials NOSPEC

CLEAR
LOAD
SAVE
Data Mode
BREAK
OK

Fig. 5.7: The input mask of the RexControl program.

TOF–spectrum. The number of used channels can be limited by setting a gate in the TOF–spectrum. This can be used to take only the relevant peaks out of the TOF–spectrum. The window 'Cnts vs Scan' shows the data from one scan whereas in the window 'Acc. Cnts vs Scan' the sum over all scans is displayed. All the data recorded with RexControl can be saved in ASCII format data files for later evaluation.

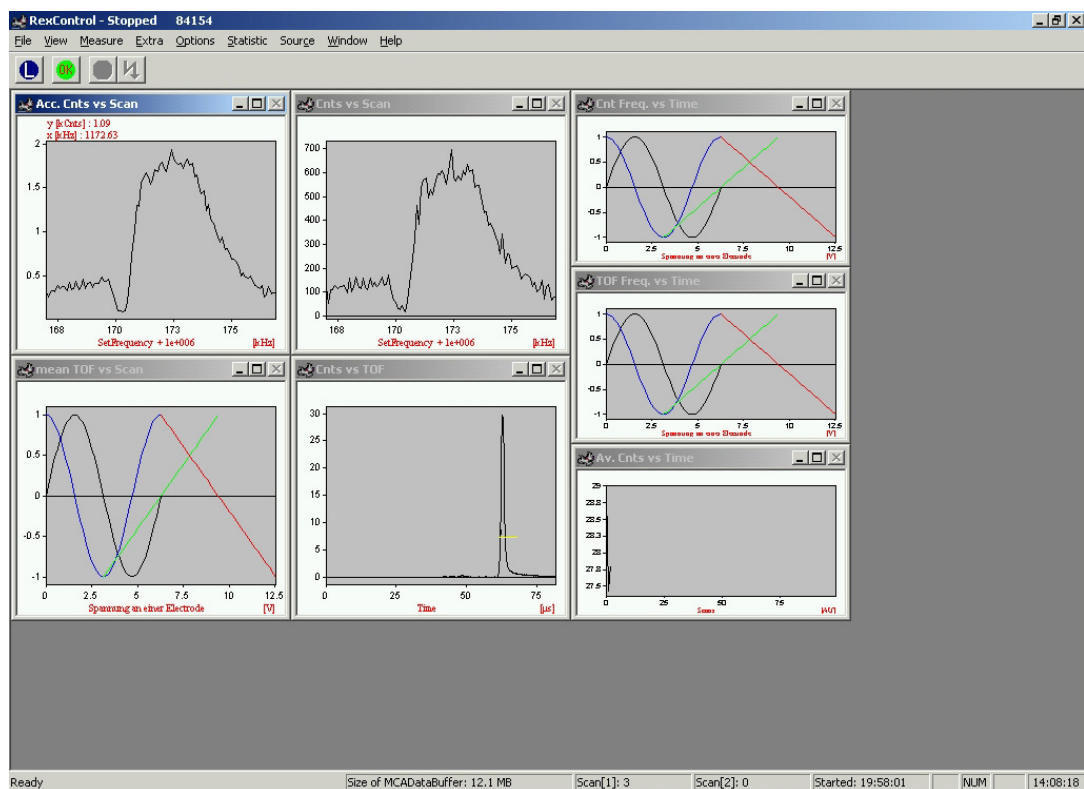


Fig. 5.8: The RexControl program during operation. The graphs show a scan over the applied frequency.

Chapter 6

The Transfer Line To The EBIS

6.1 Overview

The transfer beam line connects REXTRAP with the REXEBIS. It has to transfer the ion bunch extracted from REXTRAP to the REXEBIS without losses whilst bridging the difference in height and position between both parts. Another task of the beam transfer line is to support in achieving the required vacuum in the REXEBIS.

The setup consists of two 82.5° spherical benders and two quadrupole triplet lenses in between. In front of the lower bender a kicker allows one to direct the beam straight out of REXTRAP instead of going up which also allows REXTRAP to deliver beam to other experiments, *e.g.* WITCH (see Chapter 1.4.1). Another kicker in front of the upper bender has to be switched during the operation of REX-ISOLDE. In the kicked position the ion bunch coming from REXTRAP can penetrate into the REXEBIS. After charge-breeding the kicker has to be switched to the straight position allowing the extracted ions to pass on to the mass-separator. This operation requires a special high-voltage switch which is able to switch the required voltages (≈ 1.2 kV for a 30 keV beam) with a repetition rate of up to 100 Hz.

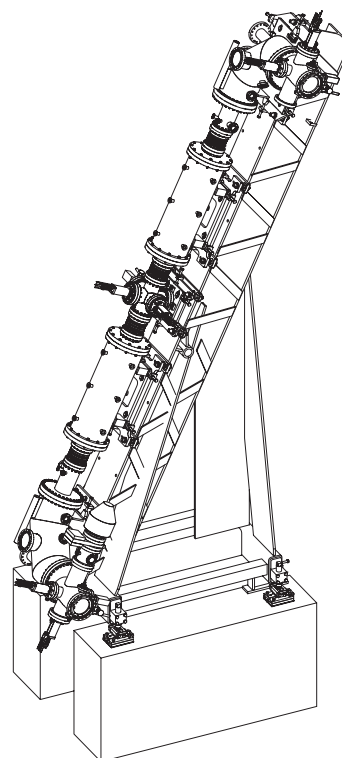


Fig. 6.1: A 3-D schematic sketch of the transfer beam line between REXTRAP and REXEBIS (Drawing by CERN, Div. EP-TA3).

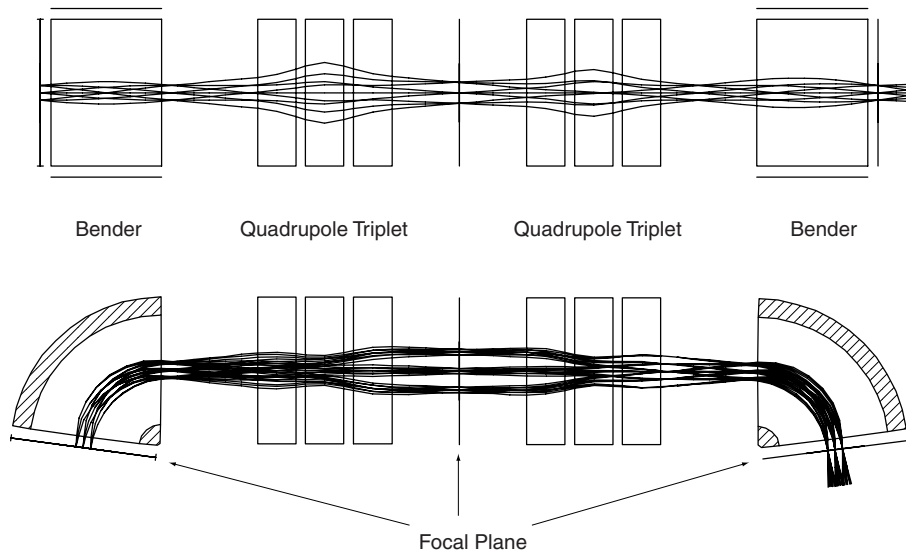


Fig. 6.2: Calculated beam path through the transfer line. The beam passes from left to right.

6.2 Beam Path

The beam coming from REXTRAP is deviated by a 7.5° kicker which consists of two parallel plates. After this the beam enters a 82.5° spherical bender. The shape of the electrodes of a spherical bender are sections of concentric spheres. A spherical bender focusses the beam in both transversal directions whereas a bender made of two parallel plates focusses the beam only in the plane where it deviates the beam. At the end of the bender the beam is bent 90° perpendicular to the REXTRAP axis. The axis of the transfer beam line is tilted through an angle of 22° with respect to the vertical axis. This tilt is necessary because the EBIS is not exactly above REXTRAP. After passing the two quadrupole triplet lenses the beam enters a second 82.5° spherical bender and again a 7.5° kicker. In the beam path there are three focal planes. Two are between the kickers and the benders and one focal plane is in the center of the transfer beam line between the two quadrupole triplet lenses. At these three positions the beam observation boxes are installed. The calculated ion trajectories can be seen in Fig. 6.2. The calculation was performed using the code 'GIOS' [Wol87] using ions of 30 keV energy. The ions were started at the first focal plane between the lower kicker and bender. The transversal phase space emittance was assumed as $10 \pi \cdot \text{mm} \cdot \text{mrad}$. The distance between the starting points on the focal plane is 4 mm with angles of 5 mrad. The assumed energy spread (which is shown only in the lower graph) was 100 eV.

Due to the symmetric setup of the transfer beam line the system is achromatic, *i.e.* particles starting from the same spot in the first focal plane with a slightly different energy will arrive at the same point in the upper focal plane. In the middle focal plane

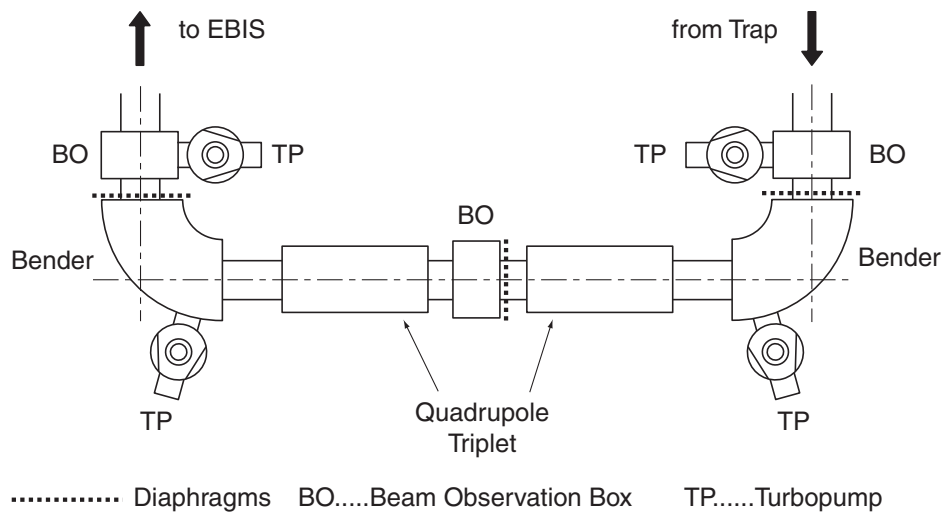


Fig. 6.3: Schematic overview of the vacuum system for the transfer beam line.

the different beam paths are separated by their energy (this behaviour can be seen in Fig. 6.2). The achromatic setup is necessary to transport the beam independently of the energy spread after the trap.

6.3 Vacuum System

Beside transporting the beam from REXTRAP to the REXEBIS one task of the transfer beam line is to prevent the REXEBIS from being flooded with buffer gas coming from REXTRAP. Inside REXTRAP the buffer gas pressure is in the region of 10^{-3} mbar (stopping part) respectively 10^{-4} mbar (trap center) while the EBIS needs a reasonably good vacuum of the order 10^{-11} mbar. To achieve this requirement a four stage differential pumping is realized in the transfer beam line. Therefore several small diaphragms at beam focal planes have been installed. Four turbo-pumps (Pfeiffer TMU 261, one per section) result in a vacuum of the order 10^{-9} mbar after the second bender. This is sufficient to achieve a reasonable vacuum inside the REXEBIS. In Fig. 6.3 a schematic overview of the vacuum system for the transfer beam line is shown. The position of the three diaphragms is marked as dashed lines. Two diaphragms are situated at the entrance of the lower bender and at the exit of the upper bender. The third diaphragm resides shortly before the beam observation box between the two quadrupole triplet lenses.

6.4 Beam Observation and Detection

To monitor the beam going from REXTRAP to the REXEBIS a new beam observation system was developed. This system has to monitor the beam intensity profile and has

to work with a wide range of beam intensities from a few particles per second for the radioactive beams up to a few nA for the stable pilot beams used for tuning and testing. In the beam transfer line between REXTRAP and REXEBIS three beam observation systems have been installed in cross-pieces inside the beam line. Every system consists of a Faraday cup for measuring the beam current and a MCP (Micro Channel Plate) / phosphorus screen combination to monitor the beam profile and to measure the beam with an MCA (Multi Channel Analyzer). Both can be introduced into the beam via a pneumatic feed-through. For the beam monitoring system the incoming beam impinges at an angle of 45° upon the MCP (see Fig. 6.4). The ions hit the MCP where they produce secondary electrons which are multiplied and accelerated inside the channels of the MCP. On the back side the secondary electrons leave the MCP and are accelerated by an electric field towards the phosphorus screen. There the electrons produce an image which is recorded with a CCD-camera. The image is transferred to a PC with a frame-grabber card where it is converted to a bitmap image. This is transferred to the console PC via Ethernet. Alternatively the signal from the MCP can be used with an MCA (e.g. an oscilloscope) to measure the pulses coming from REXTRAP.

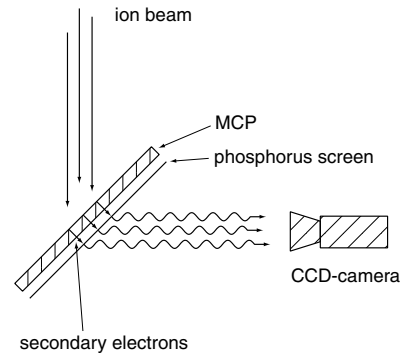


Fig. 6.4: Principle of the beam observation system. The beam hits a micro channel plate and produces secondary electrons. These hit a phosphorus screen on which an image of the beam is produced.

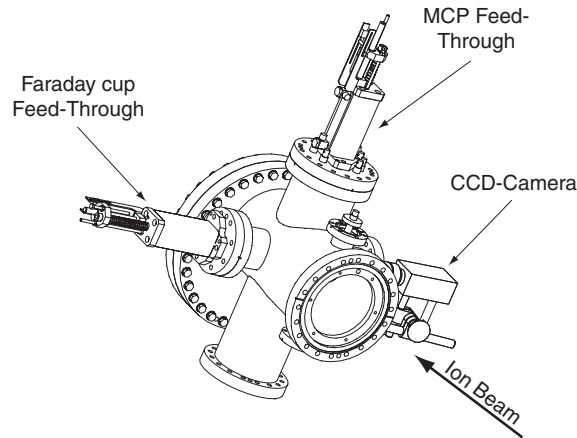


Fig. 6.5: 3D-sketch of the beam observation element (Drawing by CERN, Div. EP-TA3).

The whole setup is installed in a vacuum cross-piece. Fig. 6.5 shows a 3D-sketch of such a cross-piece with the feed-throughs and the CCD-camera attached to it. The camera is mounted outside the cross-piece. It looks at the phosphorus screen through a window on the cross-piece. Images taken with this system are shown in Chapter 7.2.

Chapter 7

Experimental Results

7.1 REXTRAP

In the first half of the year 1999 the first ions could be trapped and extracted with REXTRAP. At this time argon was used as a buffer gas. The off-line ion source was filled with cesium. The spectra of these measurements can be seen in Fig. 7.1. Due to charge exchange with the argon buffer gas atoms and ionization by trapped electrons a relatively large argon peak can be seen. Also a water peak can be seen which exists due to residual gas impurities coming from the buffer gas and from outgasing of the electrodes. These peaks could be reduced by using argon with a higher purity. Another attempt to reduce the background was the use of getter material inside the trap to reduce the residual gas impurities. The four diagrams in Fig. 7.1 represent different numbers of trapped ions. One can see a broadening of the peak with a higher number of ions due to a larger size of the ion cloud inside the trap.

With these first promising results in mind a beam time with stable isotopes from ISOLDE was taken in 1999. The main reason for this was to prove the capability to inject and trap ions coming from ISOLDE. A second reason was to work with different

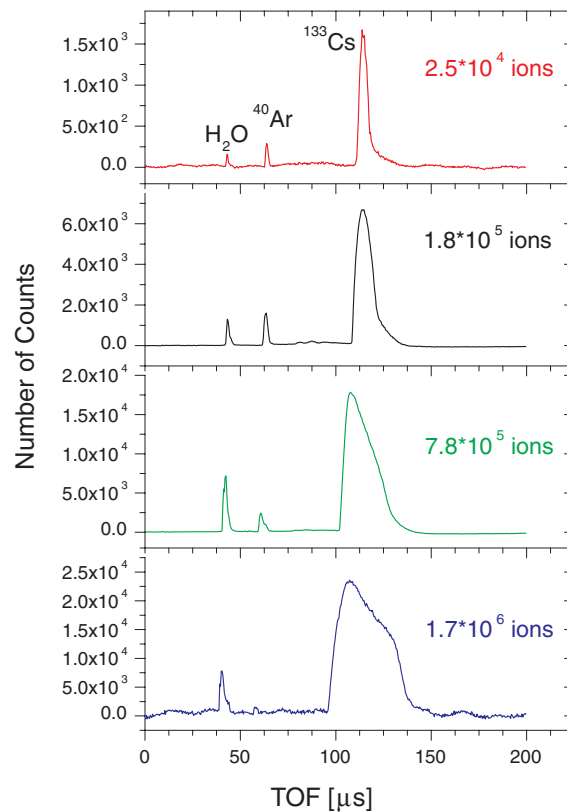


Fig. 7.1: TOF-spectra of trapped cesium ions with argon as buffer gas.

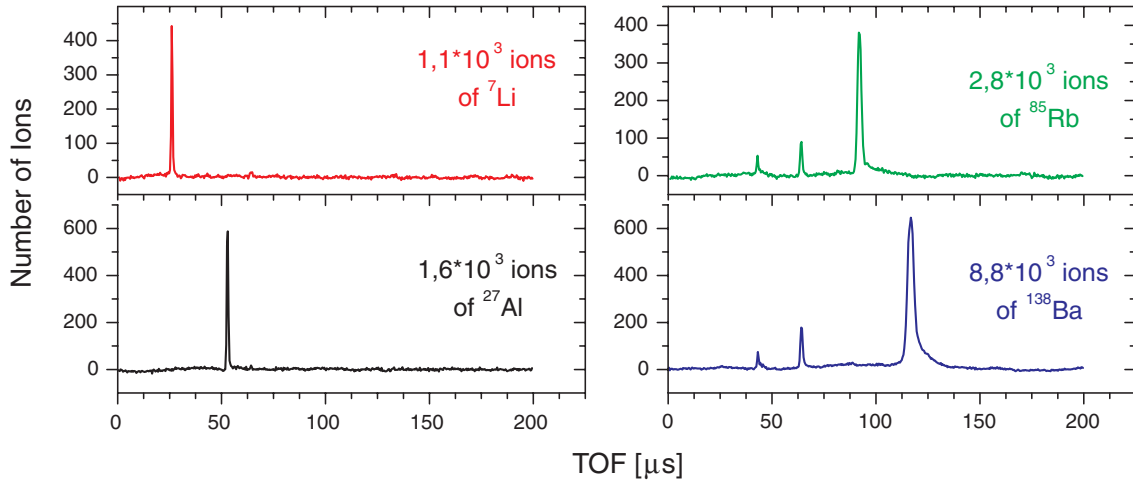


Fig. 7.2: TOF-spectra of trapped ions coming from ISOLDE.

ion species covering a wide mass range from ${}^7\text{Li}$ up to ${}^{181}\text{Ta}$. The measured time-of-flight spectra are shown in Fig. 7.2.

The ability of REXTRAP to work as an accumulation and buncher device could therefore be proven. But the most important task of REXTRAP is its ability to cool the ion bunch. The ejection diaphragm has an inner diameter of 5 mm whereas the injection diaphragm has a diameter of 10 mm. With this setup only the part of the ion cloud smaller than 5 mm can be ejected. This allows one to measure the ability to cool the ions, *i.e.* to bring the ions nearer to the center. As discussed in Chapter 3 this is achieved by a sideband cooling process via excitation of the ions with the cyclotron frequency ω_c . As can be seen in equation (3.5b) this frequency depends only on the mass, the charge and the magnetic field strength. Therefore this value should be constant for a certain ion species (all ions are singly charged). The frequency of the magnetron motion is given by equation (3.10). This equation can be evaluated by an expansion of the square root because of $\omega_c \gg \omega_z$ for the frequency values for REXTRAP. The value of ω_- is therefore approximately constant. The measurements with REXTRAP have now shown a dependency on the number of ions for the two frequencies. In Fig. 7.3 the measured shifts of the magnetron and cyclotron frequency are shown. The cyclotron frequency is not only shifted but also broadens strongly with increasing number of ions. The effects on the cyclotron frequency are combined in the diagram in Fig. 7.4.

These effects cannot be understood within the simple single particle model of the Penning trap. They are more likely connected to space charge and plasma effects. The single particle model does not take the Coulomb interactions between the charged ions into account. For two interacting particles stored in a Penning trap a analytical solution to this problem is possible [Bau93], but for 10^6 ions only numerical solutions are possible. The drawback of this simulation is again the large number of ions. With the available computer power these simulations are not possible in a

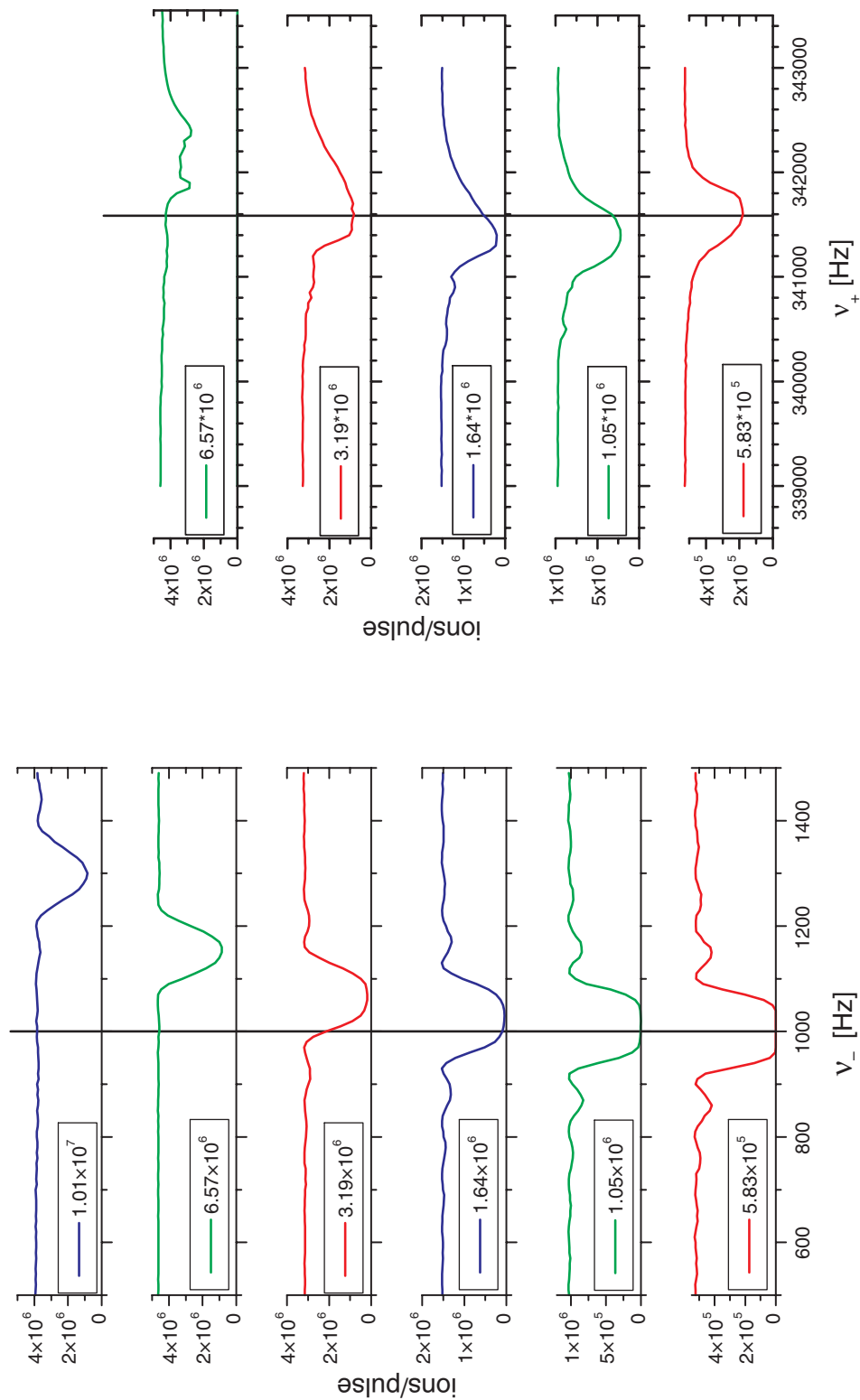


Fig. 7.3: Shifts of the magnetron and the reduced cyclotron frequency. The diagrams on the left show the shift of the magnetron frequency to higher values with higher ion numbers. The diagrams on the right show the shift for the reduced cyclotron frequency. The vertical lines show the calculated values according to the REXTRAP design values. The vertical axes show the number of ejected ions.

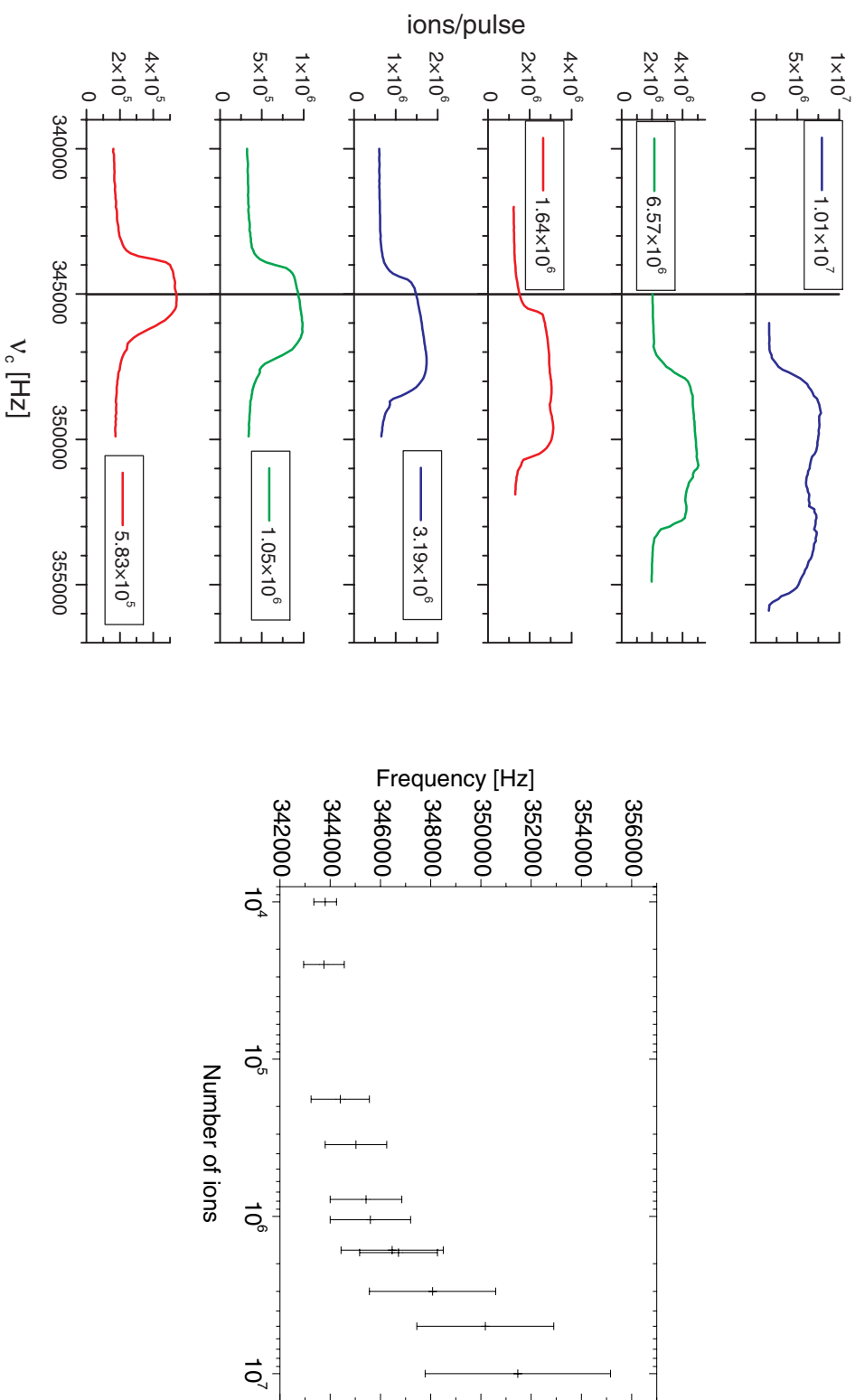


Fig. 7.4: Shifts of the cyclotron frequency. The diagrams on the left show the shift of the cyclotron frequency to higher values with higher ion numbers. The vertical line shows the calculated value according to the REXTRAP design values. The vertical axes show the number of ejected ions. The right hand diagram shows a compilation of the shift and broadening of the cyclotron frequency with subject to the number of trapped ions.

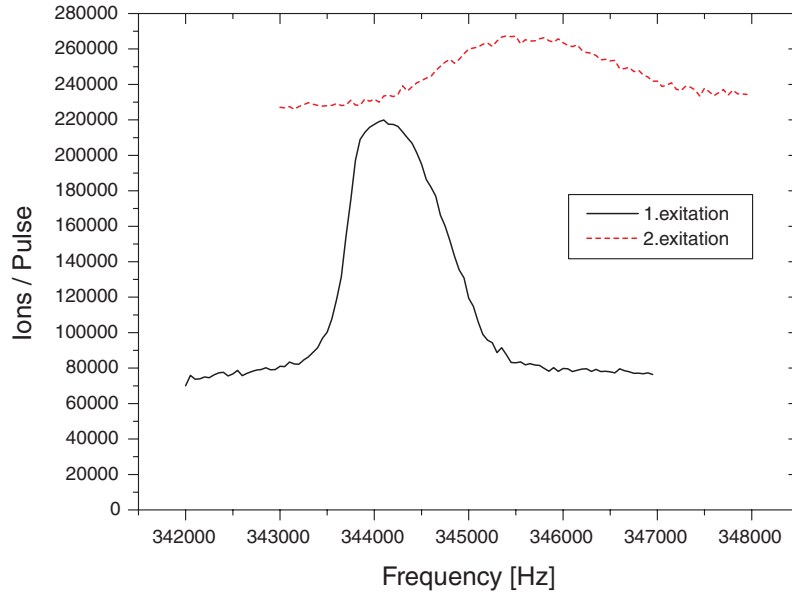


Fig. 7.5: *Effect of a second excitation after 20 ms cooling at ω_c . $1.94 \cdot 10^6$ ions have been injected which results in an efficiency of 13.4% after the second excitation.*

reasonable time. One approach to this problem was made by D. Beck [Bec01] (see also Chapter 3.3). The idea of this work was to scale the strength of the Coulomb interaction together with a reduction of the number of ions used in the calculations. This brought about a drastic reduction in the computation time (around 1 week on a Linux-cluster). These simulations could qualitatively reproduce the effects measured at REXTRAP (*i.e.* shift of ω_c in the right direction as well as a broadening of the ω_c resonance). Even with the promising results from this simulation a physical explanation for these effects in a Penning trap is still missing. Another experiment carried out at REXTRAP shows that the frequency shifts are not dependent on the number of stored ions but on the density of the ion cloud. As mentioned above the effect of the cooling process is a compression of the stored ion cloud. By performing a second excitation after a first cooling stage a shift of the resonance frequency between these two excitations could be seen (see Fig. 7.5). The resonance frequency for the second excitation was shifted again to higher values. The number of ejected ions could also be increased with this second excitation, *i.e.* the density of the ion cloud was increased further. This measurement shows therefore the dependency of the frequency shifts on the density of the ion cloud. For a complete understanding of these space-charge and plasma effects more systematic studies and simulations including the dependencies on the trap parameters (*e.g.* potential depth, magnetic field strength, ...) are essential for the operation of Penning traps with high numbers of stored ions. This is especially valid for the WITCH experiment, where high ion numbers are mandatory to achieve reasonable statistics.

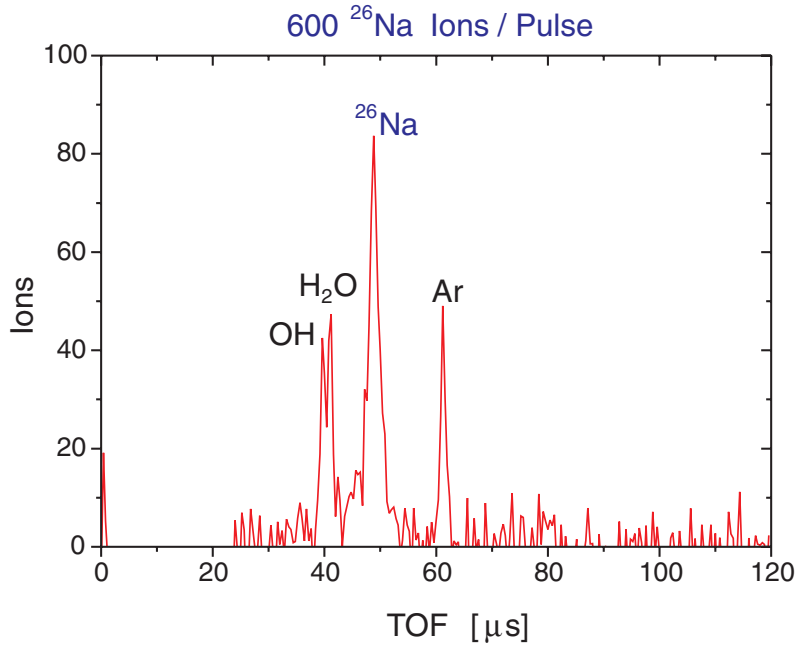


Fig. 7.6: Time-of-flight spectrum of trapped ^{26}Na .

Tab. 7.1 shows a compilation of efficiency values of selected ion species measured at REXTRAP. The measured values show a dependency of the efficiency on the number of ions. One reason for this behaviour is a non-sufficient cooling efficiency for the stored ions which results in a truncation of the ion cloud during extraction. A second reason is an insufficient injection of the ion beam into the trap. One experiment to clarify this was to inject radioactive ions with a half-life of 18 minutes. After injection the trap was dismantled to be able to measure the activity of the implanted ions in different regions of the trap structure. This experiment showed beam losses at the injection diaphragm which gave rise to an insufficient focussing of the incoming ion beam. Nevertheless, the results of the second excitation measurements clearly show that the cooling process is insufficient to cool all ions down to the required radii.

	injected ions	ejected ions	efficiency
^7Li	—	$\approx 10^3$	—
^{23}Na	$1.5 \cdot 10^4$	$3.0 \cdot 10^3$	20%
^{27}Al	$3.4 \cdot 10^8$	$1.2 \cdot 10^7$	4%
^{27}Al	$2.7 \cdot 10^4$	$7.0 \cdot 10^3$	27%
^{39}K	$3.7 \cdot 10^3$	$9.6 \cdot 10^2$	26%
^{85}Rb	$2.0 \cdot 10^4$	$2.8 \cdot 10^3$	14%
^{181}Ta	$4.4 \cdot 10^6$	$2.5 \cdot 10^5$	6%

Tab. 7.1: Trapping efficiencies of selected ion species. For ^7Li the beam intensity was too low to be measured in front of REXTRAP. The table shows the dependency of the efficiency on the number of ions.

In May 2000 experiments with radioactive beams from ISOLDE were carried out.

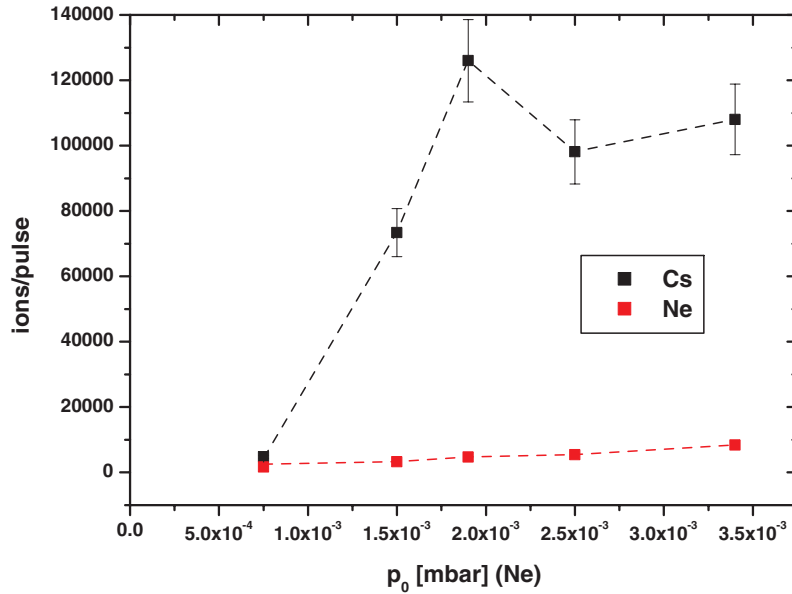


Fig. 7.7: The number of ejected ions from REXTRAP as a function of the buffer gas pressure for Cs^+ in Ne.

During this beam time β^- -unstable sodium and rubidium isotopes were used (see Tab. 7.2). One issue of this test was to detect the losses of the ions as described in the previous paragraph. Another issue was to test the influence of the electrons produced by radioactive decays of the trapped ions. The potential barriers of the trap can act as electron traps which can lead to discharges if a large number of electrons is trapped there. The stored electrons can also ionize residual gas atoms or buffer gas atoms which are then trapped in the centre, thus lowering the overall efficiency of the trap. A spectrum of the short lived ^{26}Na isotope is shown in Fig. 7.6. With the accuracy of our measurement no increase of the background due to the decay products could be detected.

Isotope	$t_{1/2}$
^{25}Na	59.6 s
^{26}Na	1.07 s
^{88}Rb	17.8 s

Tab. 7.2: Radioactive isotopes used in REXTRAP.

In October 2000 the type of the used buffer gas was switched from argon to neon. This reduced the background because of the higher ionization energy of neon compared to argon. As the mobility of cesium in neon differs from cesium in argon, the first experiment was to find out the required buffer gas pressure. The calculated ion mobility values gave rise to a 2 to 3 times higher buffer gas pressure. Fig. 7.7 shows the number of ejected $^{133}\text{Cs}^+$ ions as a function of the neon gas pressure. A comparison of this graph to the one for Cs ions in argon as given in [Sch01] shows that the required buffer gas pressure for neon is about a factor two higher than for argon. This shows that the description of the cooling process via collisions with buffer gas atoms is accurate.

7.2 Transfer Beam Line

The installation of the transfer beam line between REXTRAP and REXEBIS was finished in April 2000. This gave the opportunity to view the profile of the beam coming out of REXTRAP. The first tests resulted in a transmission of 30% to the upper part of the beam line. Putting the ion source at the beginning of the beam line gave us the awareness that transmissions of up to 100% are possible. The problem with the beam coming from REXTRAP is the low intensity. Finding the correct voltages for the benders and lenses is very tricky with ion currents less than 1 pA.

In Fig. 7.8 an image of the beam profile taken with the beam observation system of the transfer beam line during the REX–ISOLDE beam time in November 2000 is shown. It was taken with the diagnostic box between the lower kicker and bender (Element BTS.BO30). The strange looking beam spot resulted from a wire which was put in the ejection lens to remove electrons which can be stored in this region. This wire was slightly magnetic and split the beam in two. This wire was replaced after the beam time by a non–magnetic one. The left image of Fig. 7.9 shows a clear improvement of the beam shape. The right image shows the beam between the upper bender and kicker (Element BTS.BO160). The circles mark the calculated position for the beam axis (both kicked and straight direction). The smaller spot on the right side of the right image is the reflection of the beam image on the second phosphorus screen which is used for the outgoing beam of the EBIS.

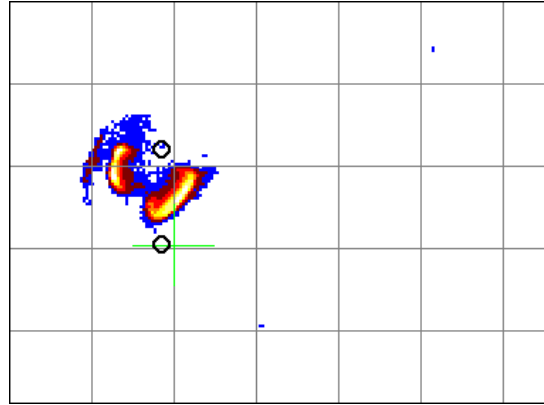


Fig. 7.8: *Beam profile taken during the REX–ISOLDE beam time Nov. 2000 (between lower kicker and bender).*

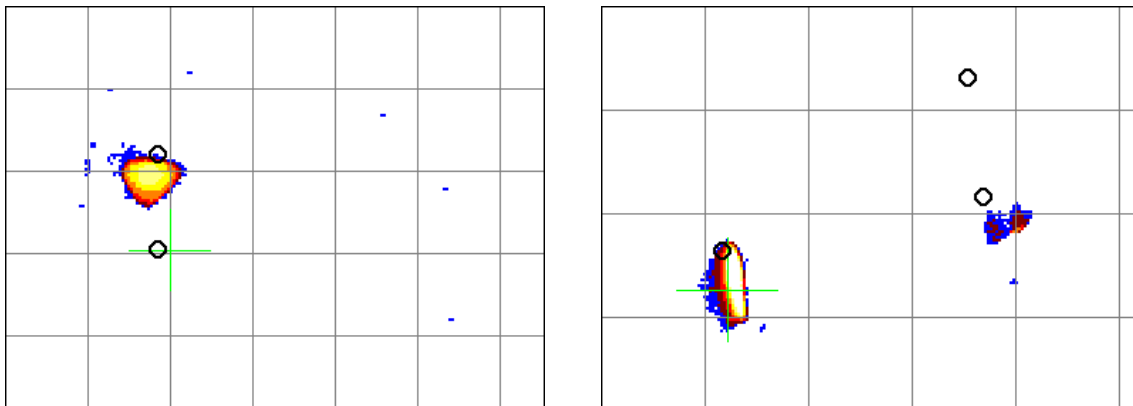


Fig. 7.9: *Beam profile in the lower (left) and upper (right) part of the transfer beam line.*

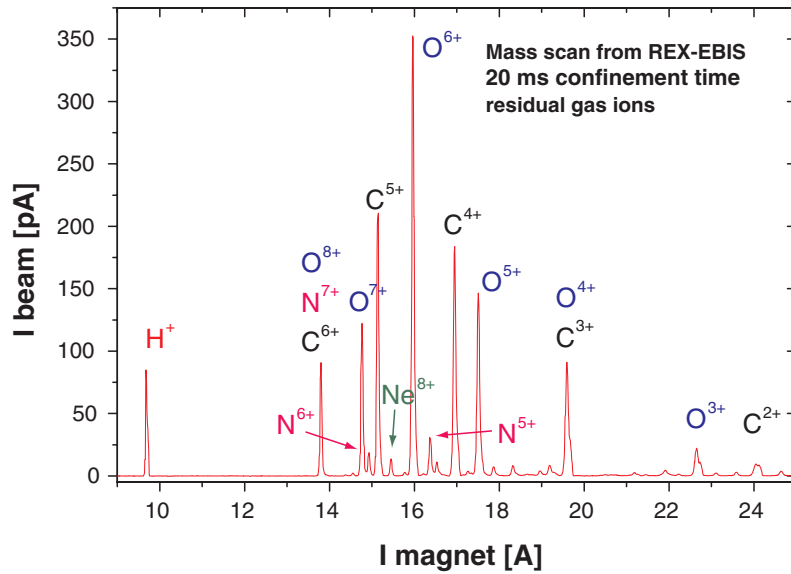


Fig. 7.10: A mass scan of a beam of residual gas ions produced by the REXEBIS after 20 ms breeding.

7.3 REX-ISOLDE Beam Time November 2000

In November 2000 the first beam time for REX-ISOLDE was scheduled. At this time REXTRAP, REXEBIS, the mass separator and the REX-RFQ were operational. The final energy of the linac was therefore 300 keV/u. The IH-structure and the 7-gap resonators were not installed. Nevertheless the injection and ejection of ions into REXEBIS as well as the injection of highly charged ions into the RFQ and their acceleration to 300 keV/u could be tested.

The first issue to be tested was the injection of an ion bunch into the REXEBIS. One major problem which was encountered was the lack of diagnostics elements in front of and inside the EBIS. The last possibility to track the ion bunch is the beam observation box at the upper end of the transfer beam line. The distance from this element to the entrance of the EBIS is about 2.5 m whereas the diameter of the electron beam to be hit is only a few millimeters, *i.e.* the lever arm for the beam steering is too large to achieve a good injection. The first point for the detection of injected ions was after the mass separator. The intensity of the beam of residual gas ions extracted from the REXEBIS was much higher compared to the weak beam coming from REXTRAP. Therefore the diagrams of a mass scan after the mass separator were mainly dominated by the peaks of multiple charged residual gas ions. Due to these problems a successful injection of ion bunches coming from REXTRAP could not be proven. Another problem, which was discovered after the beam time, was the slightly magnetic wire which was mounted at the exit part of REXTRAP (see preceding Section). The effect of this wire produced two semi-circular beams instead of one round beam.

Despite the problems with injecting ions into the EBIS the intensity of the ex-

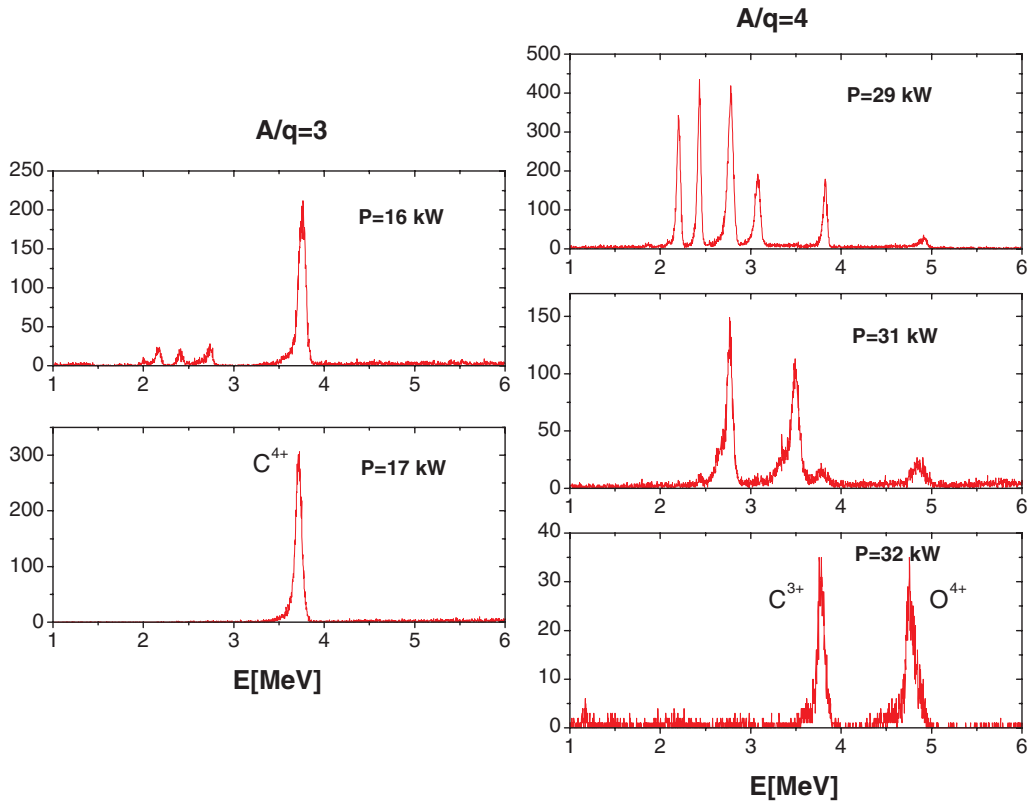


Fig. 7.11: Energy spectra of carbon and oxygen beams accelerated with the RFQ at different rf-power. The left figures were produced with an A/q -ratio of 3 whereas the right ones were produced with an A/q -ratio of 4. The spectra show clearly that a minimum rf-power is needed to achieve a complete acceleration of the ions.

tracted residual gas beam was sufficiently high to prove the functionality of the mass separator and the first stage of the REX–LINAC. Fig. 7.10 shows a mass scan recorded with the diagnostic box after the mass separator. The scan was performed by varying the current for the bending magnet of the mass separator. In this way a scan over different charge-to-mass ratios could be obtained. The diagram shows that a residual gas beam consists mainly of carbon, nitrogen, oxygen and hydrogen atoms. This results from the main parts of the vacuum impurities which are N_2 , O_2 , H_2O and CO_2 . To test the functionality of the REX–RFQ, beams of carbon and oxygen were used.

To perform energy measurements of the beam a detector box was installed after the RFQ. The energy of the accelerated particles was measured by direct implantation in a silicon detector as well as scattering of the particles on a gold foil. The scattering measurements worked in principle but the angle of the gold foil could only be measured to low accuracy. Fig. 7.11 shows energy spectra of the beams accelerated with the RFQ recorded with the silicon detector. The RFQ was tested with beams

with a mass-to-charge ratio of 3 and 4. For A/q of 3 a beam of $^{12}\text{C}^{4+}$ was used (left side of Fig. 7.11). The diagrams show clearly that a minimal rf-power of 17 kW is necessary to accelerate all particles to the final energy. If the power is too low, some particles are out of phase with the rod modulation and are not fully accelerated or even decelerated. This can be seen in the lower energy peaks in the upper diagram. The same effects can be seen for A/q of 4 where beams of $^{12}\text{C}^{3+}$ and $^{16}\text{O}^{4+}$ were used. In this case the minimal required rf-power for full acceleration was 32 kW.

7.4 Using REXTRAP for Conversion Electron Spectroscopy

In the following section a new interesting application of ion traps which was tested with REXTRAP will be presented. This experiment was performed in collaboration with L. Weissman, who also developed the special detector setup [Wei00].

The thickness of radioactive sources is a limiting factor for high-resolution electron spectroscopy, due to scattering in the source material. The detection of conversion electrons from the decay of trapped radioactive ions may provide new possibilities in electron spectroscopy since the trapped ions constitute a source of electrons without energy loss or scattering.

A second important effect comes from the magnetic field. The strong magnetic field inside REXTRAP (up to 3 T in the trap center) will cause the electrons emitted by trapped radioactive ions to be transported within a limited volume. Thus, the major part of the electrons emitted in the forward direction will be directed to the ejection diaphragm. As a result one is able to cover a large solid angle without the need of a large detector.

7.4.1 Setup

The highly efficient electron transportation within the trap makes it possible to use small-area high-resolution Si detectors. A RD EB10GC-500P detector assembly, together with a low noise PA1201 preamplifier of Canberra Semiconductor Technologies, was used for the tests. The detector has a 10 mm^2 sensitive area and $500\text{ }\mu\text{m}$ thickness. It is placed on a Peltier element together with a FET transistor. The small size of the detector and close placement of the FET ensures a low noise performance. A typical spectrum of a ^{241}Am source exhibits a resolution of 1 keV for the 59.5 keV X-ray line with a noise threshold of 2 – 3 keV. The calculated probability for electrons emitted in the forward hemisphere to reach the detector placed after the ejection diaphragm is shown in Fig. 7.12. The source diameter was chosen to be 1 mm in the calculations.

We have performed several tests of the detector assembly in an off-line test chamber using calibrated ^{133}Ba , ^{131}Ba and ^{207}Bi electron sources. A typical electron spec-

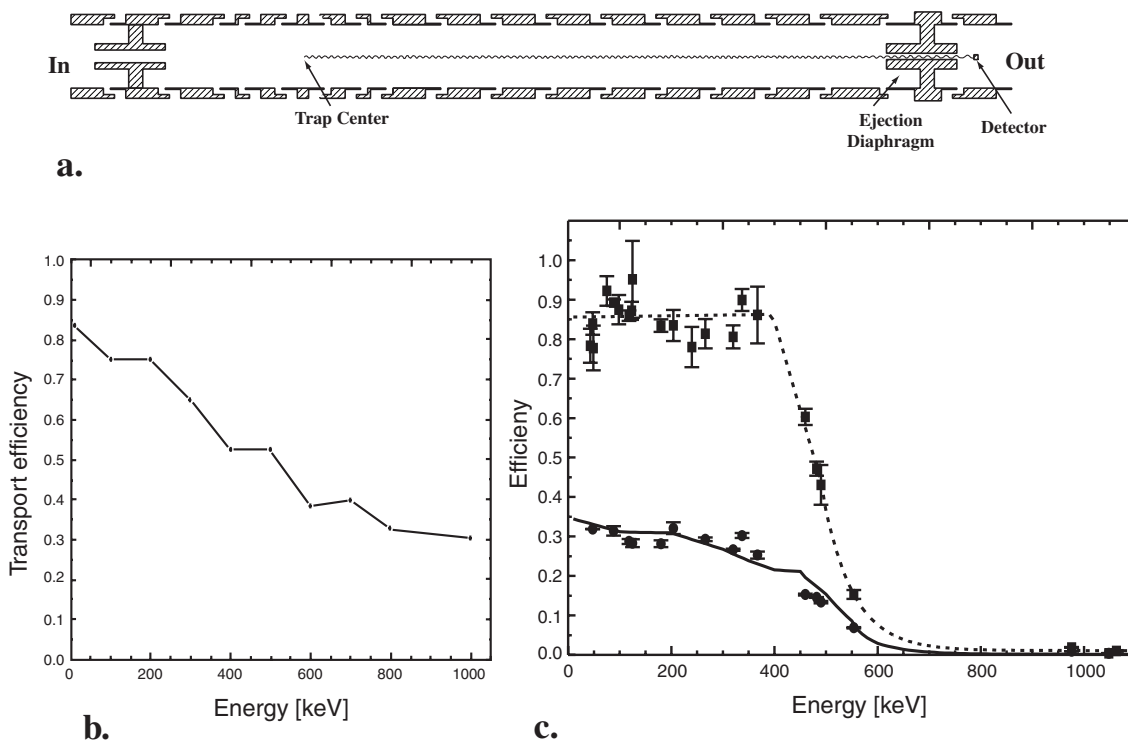


Fig. 7.12: *a. General overview of the inner part of the REXTRAP together with an example of a simulated trajectory for a 400 keV electron. b. Calculated probability for electrons emitted from the trap center to reach the detector (source diameter is 1 mm). c. Experimental (circles) and the calculated (solid line) detection efficiencies for in-trap measurements. The squares and the dashed line represent the experimental intrinsic detector efficiency measured in the test chamber [Wei00].*

trum of the ^{131}Ba source, prepared by implantation at ISOLDE, exhibits a resolution of 1.5 – 2 keV for the electron lines depending on the electron energy (Fig. 7.12). The intrinsic efficiency of the detector measured with the calibrated sources is presented in Fig. 7.12 (full squares).

Several in-trap tests with electron sources were performed. The cylindrical electrode structure and the diaphragms were removed from the trap and a rigid detector-source assembly was introduced in its place. The distance between the detector and the source was chosen to be the same as the distance from the trap center to the diaphragm. The in-trap spectra have almost two times worse energy resolution (Fig. 7.12). This is due to the larger spread in electron energy loss in the source material as the electrons emitted at large angles with respect to the axis of the magnet are also transported to the detector. Moreover during the measurements with high tension applied at the platform we observed a background associated with stray electrons from the external beam line accelerated by the applied high voltage (60 keV) and transported towards the detector (Fig. 7.12).

The measurements with the calibrated sources allow determination of the abso-

lute detection efficiency as a function of electron energy. The results are summarized in Fig. 7.12, where the experimental efficiency (full circles) is compared to a calculated efficiency curve (solid line). To calculate the latter we convoluted the intrinsic efficiency of the detector, as measured in the test chamber (full squares and dashed line), with a calculated transmission probability of electrons from a 1 mm diameter source placed in the center of the trap (Fig. 7.12). The result is corrected for a higher probability of electron backscattering from the detector and a higher probability for electrons to escape in the vicinity of the detector edge in the magnetic field.

7.4.2 Results

$^{116\text{m}}\text{In}$, $^{118\text{m}}\text{In}$ and $^{138\text{m}}\text{Cs}$ fission products produced by proton induced fission in a standard ISOLDE UC target were used for the first tests. All trap parameters were optimized using stable ^{238}U and ^{138}Ba beams. After optimization of the trap parameters the detector assembly was introduced into the trap. We were able to observe conversion electrons emitted from the trapped radioactive nuclei. A typical spectrum of conversion electrons from the $^{116\text{m}}\text{In}$ isomer is shown in Fig. 7.13. One observes a strong 60 keV peak corresponding to the stray electrons from the beam line accelerated by the trap's high tension. The 134.5 and 158.2 keV peaks are also clearly visible. The latter corresponds to the K- and L-lines of the 159 keV isomeric transition of $^{116\text{m}}\text{In}$. The 20.1 keV Auger transition is also seen. Unfortunately this measurement was carried out while another experiment utilized the ISOLDE laser ion source causing a strong electronic noise and hence a worse energy resolution (4 keV). This suggests that there is a possibility to significantly improve the quality of these first in-trap spectra. It is interesting to compare this spectrum to a spectrum of electrons from the thinnest available ^{131}Ba source placed in the trap (Fig. 7.13). Even with a very low energy resolution and with strong background from accelerated stray electrons, the spectrum from the trapped ions exhibits a much better lineshape and peak to background ratio than measurements with an implanted source (see Fig. 7.13).

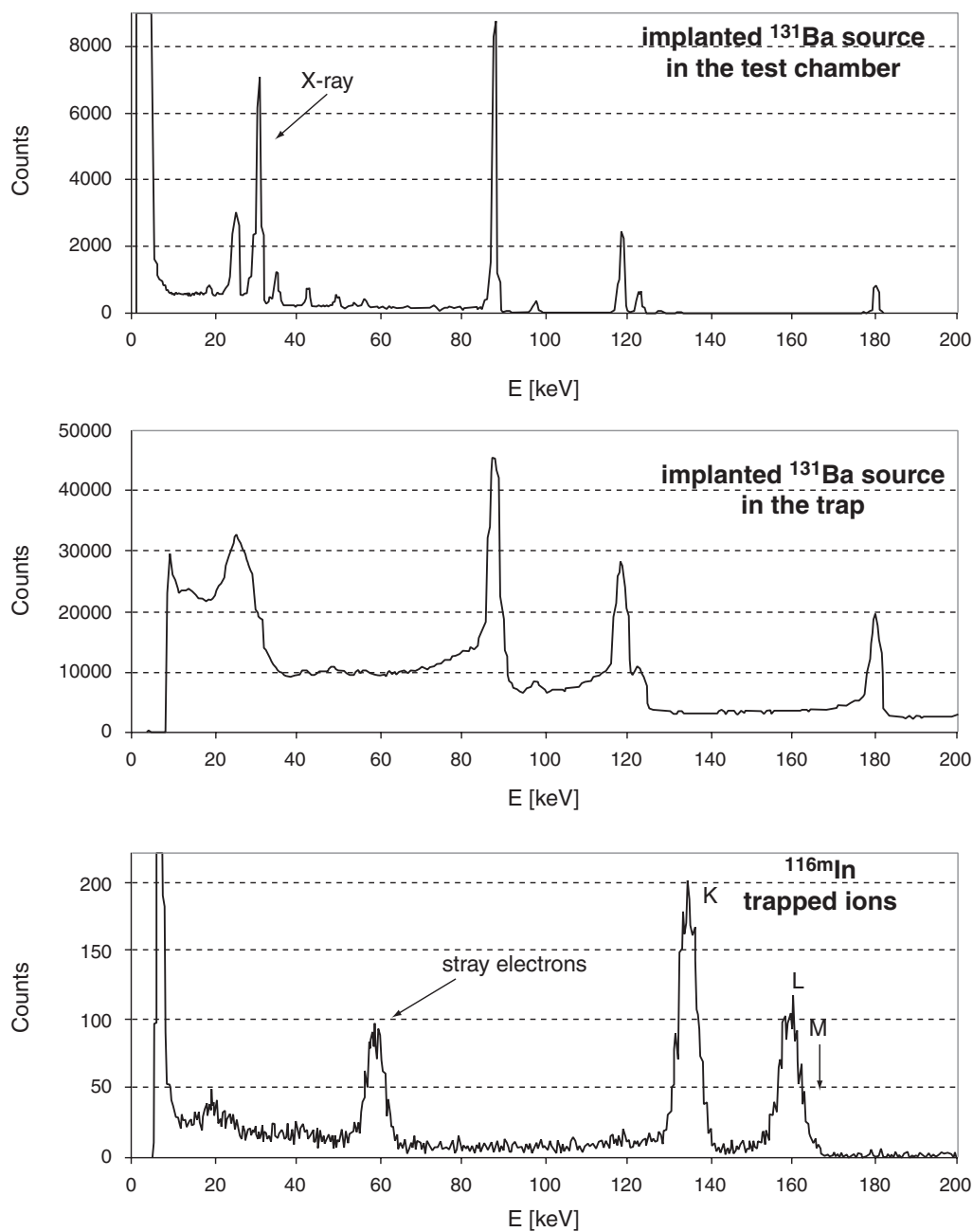


Fig. 7.13: Comparison of the electron spectra of trapped and implanted sources. The upper diagram shows the spectrum of a ^{131}Ba implanted source. The middle diagram shows the same source in the trap. The lower diagram shows a spectrum of trapped ^{116m}In ions [Wei00].

Chapter 8

Conclusion and Outlook

REX-ISOLDE is a pioneering experiment for the new concept of using a Penning trap as a buncher device in combination with an EBIS as a charge breeder for efficient post-acceleration of radioactive ions. To conclude the work described in the present thesis the ability of REXTRAP to operate in the framework of REX-ISOLDE is discussed.

The use of Penning traps as cooler devices and precision mass-spectrometers has a long tradition at ISOLDE. In 1986 the ISOLTRAP experiment was installed at the ISOLDE on-line mass separator. A theoretical prescription of the particle motion inside the Penning trap was derived for excitation with rf-fields and for buffer gas cooling. REXTRAP is a pioneer setup concerning the size of the trap and the number of ions to be stored. The maximum achieved efficiency with the ISOLTRAP cooler trap is 10%. The goal of REXTRAP is to achieve an efficiency as close to 100% as possible.

Shortly after the first successful capture of ions in REXTRAP shifts in the resonance frequencies were observed, which were not compatible with the established theory of the motion in a Penning trap. More systematic studies of these effects led to the conclusion, that the source of the effects probably lies in the Coulomb interaction between the stored particles. This interaction has been neglected until now, because of the low number of stored ions and respectively the low density of the ion cloud in the existing Penning traps. Because of the size of REXTRAP this can no longer be neglected, but has to be included into the theory. The problem is, that the corresponding multiple particle theory has no algebraic solution. Even a numerical solution is difficult to find because of the large number of ions ($> 10^6$). For a complete understanding and quantification of the observed effects more theoretical investigation is required. The question which arises is, how the operation of REXTRAP is affected by these new effects. For most experiments to be performed at REX-ISOLDE the yields for the production of the radioactive ions are smaller than the limits at which Coulomb interaction effects start to influence the trap operation. Problems may arise by the use of REXTRAP as a beam cooler for the WITCH experiment (Section 1.4.1).

For sufficient statistics 10^9 ions per bunch are required. Another problem is the use of stable beams out of REXTRAP as “pilot” beams. To achieve a good injection into the EBIS high beam currents are desired. To achieve 1 nA beam current 10^9 ions per bunch are required, which is also far above the limit of neglectable space-charge effects.

Before any of these tests could be performed, a lot of time was spent to bring REXTRAP into operation. As REXTRAP operates on a high voltage platform an important point in the REXTRAP setup is the control system. Therefore a major part of my work was to adapt the existing control system used at the ISOLTRAP-experiment to the demands of the REXTRAP operation. I continued the work which was started by P. Schmidt [Sch01]. Because of the larger amount of data a complete revision of the network protocol was necessary. Also the user interface programs were adapted to meet the different requirements of REXTRAP compared to ISOLTRAP. After building a reliable control system a reasonable amount of time was spent in the commissioning phase of REXTRAP. This includes showing the functionality of REXTRAP and characterizing the dependencies of all parameters of REXTRAP in order to achieve a maximum performance for a routine operation. Most of these experiments were performed with the off-line ion source of REXTRAP. A few shifts of stable and radioactive ISOLDE beams were taken to ensure the operation of REXTRAP with ion beams from the ISOLDE separator. Besides this, mechanical and electronics work was necessary in order to complete the setup of REXTRAP and the transfer beam line.

In conclusion, the construction of REXTRAP is now completed and its operation has been proven. Although unforeseen effects were observed in the commissioning phase of REXTRAP, its operation inside the framework of REX-ISOLDE is not influenced by these effects. An efficiency of more than 30% for the operation of REXTRAP could be achieved. The setup of the transfer beam line is also completed and recent tests showed that 100% transmission is possible with beams coming from REXTRAP. The injection of the ion bunch into the EBIS has not been possible until now, but the problems are known and with the improvements made at both REXTRAP and at the EBIS in the last year a successful injection will soon be achieved¹. The extraction and acceleration of residual gas ions from the EBIS was already successful. The remaining parts of the LINAC are installed and the commissioning of the complete LINAC is currently in progress. After a successful commissioning of REX-ISOLDE the system is ready for new interesting physics experiments with radioactive ions far from stability.

¹In the end of August 2001 the first successful injection of potassium ions could be achieved — even if the efficiency was very low.

Appendix A

Coulomb Excitation and Neutron-Transfer Reactions

The two major reactions for experiments with REX-ISOLDE are Coulomb excitation and neutron transfer reaction. In the following sections these reactions are explained in detail and important relations for the cross-sections and the required energies are derived.

A.1 Coulomb excitation

Coulomb excitation is an electromagnetic process which is very useful in the study of the nuclear structure and the investigation of deformations of nuclei. It is possible to excite lower lying nuclear states and to investigate their electromagnetic multipole moments. In the following a short description as it may be found in [MK94] is given.

Coulomb excitation is the electromagnetic excitation of a nucleus by a passing charged particle. If the energy is lower than the Coulomb barrier this process is not influenced by nuclear forces. The projectiles describe a trajectory similar to the case of Rutherford scattering. Under certain conditions the process of Coulomb excitation can be described semi-classically. One of the conditions requires the wave-length to be small compared to the smallest distance of the particles. This is the case if the Sommerfeld parameter η is larger than 1. The reactions' process should also be adiabatic, *i.e.* the time the projectile passes in the reaction should be small compared to the period of the excitation. This condition can be formulated as follows: with v the velocity of the projectile and $a = r_{\min}/2$, the passing time is characterised as a/v . This time should be small compared to $1/\omega_{if} = \hbar/(E_f - E_i)$, where E_i and E_f are the initial and final energies of the excited nuclear state. Therefore one can define a parameter ξ which describes whether a process happens adiabatically:

$$\xi = \frac{a}{v} \frac{(E_f - E_i)}{\hbar} = \frac{Z_1 Z_2 e^2}{\hbar v} \cdot \frac{\Delta E}{2T} = \eta \frac{\Delta E}{2T} \ll 1 \quad , \quad (\text{A.1})$$

where a is derived from a central collision, η is the Sommerfeld parameter and T is the kinetic energy of the projectile. For a non-adiabatic impact collision the differential cross-section can be described as a product of Rutherford cross-sections and the excitation probability P ,

$$\frac{d\sigma}{d\Omega} = P \left(\frac{d\sigma}{d\Omega} \right)_{\text{Ruth}} \quad \text{with} \quad P = \sum |b_{\text{if}}|^2 \quad . \quad (\text{A.2})$$

The probability P is the sum over the magnetic states of the squares of the excitation amplitudes b_{if} . These amplitudes can be obtained from first-order perturbation calculations,

$$b_{\text{if}} = -\frac{i}{\hbar} \int_{-\infty}^{+\infty} \langle f | H'(t) | i \rangle e^{i\omega_{\text{if}} t} dt \quad . \quad (\text{A.3})$$

The interaction Hamiltonian $H'(t)$ is the time-dependent operator of the electromagnetic interaction between target and projectile. The cross section is therefore only dependent on the characteristics of the nucleus through the matrix elements of the electric and magnetic multipole momenta. One solution for the total cross section with electrical multipole excitation is

$$\sigma = \left(\frac{Z_1 e}{\hbar v} \right)^2 a^{-2l+2} B(\text{El}) f_l(\xi) \quad . \quad (\text{A.4})$$

The quantity $B(\text{El})$ is the reduced transition probability and $f_l(\xi)$ a function which depends on ξ and the multipolarity l . For an E2-transition at $\xi \ll 1$, the value of $f(\xi)$ is near 1. By the use of Coulomb excitation one can deduce transition probabilities which can be used to determine the deformation of a nucleus. The experimental setup for such an experiment consists of a gamma detector and a particle detector. The γ -spectrum of the Coulomb excitation is measured with the gamma detector in coincidence with the backscattered projectile. In this setup only almost central collisions are of interest. For this type of collision the condition (A.1) was deduced.

The following equation gives an indication of the required energy of the projectile for Coulomb excitation:

$$E_{\text{CM}}^{\text{max}} = \frac{Z_1 Z_2 e^2}{D} \quad (\text{A.5})$$

with the distance:

$$D = R_1 + R_2 + S \quad , \quad (\text{A.6})$$

where R_1 and R_2 are the maximal nuclear radii taking account of the nuclear deformation β , and $S = 6.5$ fm [Wol93] is the minimal distance of the nuclear surfaces. Only for energies with $E_{\text{CM}} \leq E_{\text{CM}}^{\text{max}}$ is the interaction between target and projectile nuclei purely (> 99%) electromagnetic.

The detector setup used at REX-ISOLDE consists of a Ge-detector array called "Miniball" and a particle detector with the shape of a Compact Disc. The detector setup is explained in detail in Section 2.7.

A.2 Neutron Transfer Reactions

A neutron transfer reaction is a nuclear process in which one or more neutrons are picked up from, or stripped to, the target. The cross section for this process can be parametrized as follows

$$\frac{d\sigma_{\text{tr}}}{dD} = (1 - P_{\text{abs}}(D)) P_{\text{tr}}(D) \frac{d\sigma_{\text{Ruth}}}{dD} \quad , \quad (\text{A.7})$$

with the distance of the closest approach D defined as:

$$D(\theta) = a \left(1 + \frac{1}{\sin\left(\frac{\theta}{2}\right)} \right) \quad , \quad (\text{A.8})$$

and

$$\frac{d\sigma_{\text{Ruth}}}{dD} = 2\pi(D - a) \quad . \quad (\text{A.9})$$

The quantity P_{tr} is the transfer probability and $(1 - P_{\text{abs}})$ is a factor describing the absorption from the elastic channel. The transfer cross section should have a maximum at the nuclear interaction radius

$$R_{\text{int}} = C_1 + C_2 + 4.49 - \frac{C_1 + C_2}{6.35} \quad [\text{fm}] \quad , \quad (\text{A.10})$$

where C_i are the nuclear radii taking into account the diffuseness of the mass distribution [Wol93]. The absorption coefficient can be parametrized by

$$1 - P_{\text{abs}}(D) = \exp\left(-\frac{2V(D)D}{\hbar v}\right) \quad (\text{A.11})$$

with the Woods–Saxon potential

$$V(D) = V_0 \cdot \exp\left(-\frac{D - C_1 - C_2}{a_w}\right) \quad . \quad (\text{A.12})$$

It is parametrized by the potential depth V_0 and the diffuseness a_w with typical values in our mass region of $V_0 = -25$ MeV and $a_w = 0.6$ fm. The transfer probability is given by [Bas80]

$$P_{\text{tr}}(D) \propto \frac{a}{D - a} \exp(-2\kappa D) \quad \text{with} \quad \kappa = \sqrt{\left(\frac{2\mu B_{\text{eff}}}{\hbar^2}\right)} \quad (\text{A.13})$$

where μ is the reduced mass of the transferred particle and B_{eff} its binding energy. The total integrated maximum transfer cross section depends on the Q_{gg} -value [Ber87], but for our positive Q_{gg} -values, one expects 100 – 200 mb for the one neutron transfer cross section. For spectroscopic reasons it appears advantageous to use neutron rich targets to limit the Q_{gg} -values to 2 – 3 MeV.

Appendix B

Addendum to the Penning Trap Theory

B.1 Shift of the Resonance Frequencies of the Damped Ion Motions

The resonance frequency of an harmonic oscillator with damping experiences shifts. In the following an estimation for the shift of the eigenfrequencies of the particle motion in a Penning trap with buffer gas is given.

Using the velocity dependent ansatz

$$\vec{F} = -\delta\vec{v} = -km\vec{v} \quad , \quad (\text{B.1})$$

the equations of motion for the Penning trap with buffer gas become:

$$\ddot{x} - \frac{\omega_z^2}{2}x - \omega_c\dot{y} + k\dot{x} = 0 \quad (\text{2.2a})$$

$$\ddot{y} - \frac{\omega_z^2}{2}y + \omega_c\dot{x} + k\dot{y} = 0 \quad (\text{2.2b})$$

$$\ddot{z} + \omega_z^2z + k\dot{z} = 0 \quad . \quad (\text{2.2c})$$

The axial motion is still decoupled and is described by a damped harmonic oscillator with the following solution:

$$z = A_z e^{\frac{k}{2}t} e^{i\omega t} \quad \text{with} \quad \omega = \sqrt{\omega_z^2 - \frac{k^2}{4}} \quad . \quad (\text{B.3})$$

The remaining coupled equations can be solved using the ansatz $u = x + iy$:

$$\ddot{u} - \frac{\omega_z^2}{2}u + (i\omega_c + k)\dot{u} = 0 \quad . \quad (\text{B.4})$$

Using the ansatz $u = e^{i\omega t}$ one gets the following quadratic equation

$$\omega^2 + (\omega_c - ik)\omega + \frac{\omega_z^2}{2} = 0 \quad , \quad (\text{B.5})$$

with the solution

$$\omega_{1,2} = \frac{1}{2} \left(ik - \omega_c \pm \sqrt{(\omega_c - ik)^2 - 2\omega_z^2} \right) . \quad (\text{B.6})$$

The square root can be expanded into a power series and afterwards separated into its real and imaginary parts:

$$\begin{aligned} \sqrt{(\omega_c - ik)^2 - 2\omega_z^2} &= \sqrt{\omega_c^2 - 2\omega_z^2} \cdot \sqrt{1 - \frac{2ik\omega_c + k^2}{\omega_c^2 - 2\omega_z^2}} \\ &\approx \sqrt{\omega_c^2 - 2\omega_z^2} \cdot \left(1 - \frac{2ik\omega_c + k^2}{2(\omega_c^2 - 2\omega_z^2)} - \frac{(2ik\omega_c + k^2)^2}{8(\omega_c^2 - 2\omega_z^2)^2} \right) . \end{aligned} \quad (\text{B.7})$$

For the solution of eq. B.5 one obtains:

$$\begin{aligned} \omega_{1,2} &= \frac{1}{2} \cdot \left[-\omega_c \pm \left(\sqrt{\omega_c^2 - 2\omega_z^2} - \frac{k^2}{8} \cdot \frac{k^2 - 8\omega_z^2}{(\omega_c^2 - 2\omega_z^2)^{3/2}} \right) \right] \\ &\quad + i \cdot \frac{k}{2} \cdot \left[1 \pm \left(-\frac{\omega_c}{\sqrt{\omega_c^2 - 2\omega_z^2}} - \frac{k^2\omega_c}{2(\omega_c^2 - 2\omega_z^2)^{3/2}} \right) \right] , \end{aligned} \quad (\text{B.8})$$

and the solution of eq. B.4 is now:

$$u(t) = A_+ e^{-\sigma_+ t} e^{-i\omega_+ t} + A_- e^{-\sigma_- t} e^{-i\omega_- t} \quad (\text{B.9})$$

$$\begin{aligned} \text{with } \omega_{\pm} &= \frac{1}{2} \cdot \left(\omega_c \pm \sqrt{\omega_c^2 - 2\omega_z^2} \right) \pm \frac{k^2}{16} \cdot \frac{8\omega_z^2 - k^2}{(\omega_c^2 - 2\omega_z^2)^{3/2}} \\ \sigma_{\pm} &= \frac{k}{2} \cdot \left[1 \pm \left(\frac{\omega_c}{\sqrt{\omega_c^2 - 2\omega_z^2}} + \frac{k^2\omega_c}{2(\omega_c^2 - 2\omega_z^2)^{3/2}} \right) \right] . \end{aligned}$$

The terms σ_{\pm} can be expressed in terms of ω_1 , using the relations $\omega_c = \omega_+ + \omega_-$ and $\omega_1 = \omega_+ - \omega_-$ and neglecting the terms $\sim \omega_c^{-2}$:

$$\sigma_+ = \frac{k}{2} \cdot \left(1 + \frac{\omega_+}{\omega_1} + \frac{\omega_-}{\omega_1} \right) \approx \frac{k\omega_+}{\omega_1} \quad (\text{2.10a})$$

$$\sigma_- = \frac{k}{2} \cdot \left(1 - \frac{\omega_+}{\omega_1} - \frac{\omega_-}{\omega_1} \right) = \frac{k}{2} \cdot \left(1 - \frac{\omega_1 + \omega_+}{\omega_1} - \frac{\omega_-}{\omega_1} \right) = -\frac{k\omega_-}{\omega_1} . \quad (\text{2.10b})$$

This result is in good agreement with the solution obtained in Chapter 3.2.1 (eqs. (3.40)). It shows the increase of the magnetron radius and the decrease of the cyclotron radius as a consequence of the frictional damping.

For typical REXTRAP parameters ($k = 1196 \text{ s}^{-1}$ for K in Ne at $4 \cdot 10^{-4} \text{ mbar}$, $\omega_c = 7.37 \cdot 10^6 \text{ s}^{-1}$ and $\omega_z = 3 \cdot 10^5 \text{ s}^{-1}$) the resulting shift of the eigenfrequencies are:

$$\Delta\omega_z = 0.6 \text{ s}^{-1} \quad (\text{B.11})$$

$$\Delta\omega_{\pm} = \pm 1.6 \cdot 10^{-4} \text{ s}^{-1} . \quad (\text{B.12})$$

This result shows that the shifts of the resonance frequencies due to the frictional damping of the buffer gas can be neglected for normal trap conditions ($k \ll \omega_z, \omega_c$).

B.2 Discussion of the Fourier Transformation of the Excitation

The Fourier transformation of the funktion $F(t)$ in eq. (3.48) leads to

$$\tilde{F}(\vec{n} \cdot \vec{\omega}) = \int_{-T/2}^{T/2} F(t) e^{i\vec{n} \cdot \vec{\phi}} dt = e^{i\alpha_{\text{rf}}} \frac{\sin(\omega_{\text{rf}} - \vec{n} \cdot \vec{\omega})}{\omega_{\text{rf}} - \vec{n} \cdot \vec{\omega}} \cdot \frac{T}{2} + e^{i\alpha_{\text{rf}}} \frac{\sin(\omega_{\text{rf}} + \vec{n} \cdot \vec{\omega})}{\omega_{\text{rf}} + \vec{n} \cdot \vec{\omega}} \cdot \frac{T}{2} . \quad (\text{B.13})$$

In case of an excitation near a resonance ($\omega_{\text{rf}} \approx \vec{n} \cdot \vec{\omega}$), the second term can be neglected. Using the relation $\Delta\omega = \omega_{\text{rf}} - \vec{n} \cdot \vec{\omega}$ and neglecting a phase shift between the excitation frequency and the ion motion, *i.e.* $\alpha_{\text{rf}} = 0$, one obtains the following result:

$$\tilde{F}(\Delta\omega) = \frac{\sin(\Delta\omega T/2)}{\Delta\omega} . \quad (\text{B.14})$$

Using the following representation of Dirac's δ -funktion,

$$\delta(x) = \lim_{n \rightarrow \infty} \frac{\sin(nx)}{\pi x} , \quad (\text{B.15})$$

one obtains the results with the following relation:

$$\lim_{T \rightarrow \infty} \tilde{F}(\Delta\omega) = \pi \cdot \delta(x) \quad \text{with} \quad x = \Delta\omega \quad \text{and} \quad n = T/2 . \quad (\text{B.16})$$

For the limit of $\Delta\omega \rightarrow 0$ the result of eq. (B.14) in case of resonance is:

$$\tilde{F}(0) = T/2 . \quad (\text{B.17})$$

For the width of the resonance one has to take into account that the area under the resonance curve stays the same, *i.e.* if the height increases proportional to $T/2$, the width has to decrease proportional to $1/T$. The area of the resonance curve calculated from eq. (B.16) has the value of π . This leads to the following relation:

$$\tilde{F}(0) \cdot \Delta\omega_{\text{FWHM}} = \frac{T}{2} \cdot \Delta\omega_{\text{FWHM}} = \pi \quad \implies \quad \Delta\omega_{\text{FWHM}} = \frac{2\pi}{T} . \quad (\text{B.18})$$

Bibliography

- [Bas80] R. Bass, *Nuclear Reactions with Heavy Ions*, Springer Verlag, Berlin, 1980.
- [Bau93] G. Baumann, *Mathematica in der Theoretischen Physik*, Springer-Verlag, Berlin, Heidelberg, 1993.
- [Bec99] D. Beck, M. Beck, T. Phalet, P. Schuurmans, N. Severijns, A. van Geert, B. Vereecke, S. Versyck, J. Deutsch, R. Prieels, G. Bollen, O. Forstner, J. Dilling, W. Quint, F. Ames and P. Schmidt, Proposal to the ISOLDE scientific committee: search for new physics in β -neutrino correlations using trapped ions and a retardation spectrometer, CERN/ISC 99-13/P111, 1999.
- [Bec00] D. Beck, F. Ames, M. Beck, G. Bollen, B. Delauré, J. Deutsch, J. Dilling, O. Forstner, T. Phalet, R. Prieels, W. Quint, P. Schmidt, P. Schuurmans, N. Severijns, B. Vereecke and S. Versyck, Search for new physics in beta-neutrino correlations with the WITCH spectrometer, *Hyp. Int.*, 2000, submitted for publication.
- [Bec01] D. Beck, F. Ames, M. Beck, G. Bollen, B. Delauré, P. Schuurmans, S. Schwarz, P. Schmidt, N. Severijns and O. Forstner, Space charge effects in a gas filled Penning trap, *Hyp. Int.*, 2001, in press.
- [Ber87] A. M. van den Berg, K. E. Rehm, D. G. Kovar, W. Kutschera and G. S. F. Stephans, Systematics of quasi-elastic neutron transfer cross sections for heavy-ion induced reactions, *Phys. Lett. B*, vol. 194, p. 334, 1987.
- [Bol96] G. Bollen, S. Becker, H.-J. Kluge, M. König, R. Moore, T. Otto, H. Raimbault-Hartmann, G. Savard, L. Schweikhard, H. Stolzenberg and the ISOLDE Collaboration, ISOLTRAP: a tandem Penning trap system for accurate on-line mass determination of short-lived isotopes, *Nucl. Inst. & Meth. in Phys. Res.*, vol. A368, p. 675, 1996.
- [Bru] R. Brun, F. Rademakers and other, The ROOT Object Oriented Framework. URL <http://root.cern.ch/>
- [Cam97] L. Campajola et al., Letter of Intent to the ISOLDE scientific committee: Measurement of the ${}^7\text{Be}(p,\gamma){}^8\text{B}$ absolute cross section in inverse kinematics, CERN/ISC 97-1/I20, Jan. 1997.

- [Cub00] J. Cub, C. Gund, D. Pansegrau, G. Schrieder and H. Stelzer, A position sensitive parallel plate avalanche counter for single-particle and current read-out, *Nucl. Inst. & Meth. in Phys. Res.*, vol. A453, p. 522, 2000.
- [Dob94] J. Dobaczewski et al., Nuclear Shell Structure at Particle Drip Lines, *Phys. Rev. Lett.*, vol. 72, p. 981, 1994.
- [Dub99] D. H. E. Dubin and T. M. O'Neil, Trapped nonneutral plasmas, liquids, and crystals (the thermal equilibrium states), *Rev. Mod. Phys.*, vol. 71, p. 87, 1999.
- [Ebe96] J. Eberth, H. G. Thomas, P. von Brentano, R. M. Lieder, H. M. Jäger, H. Kämmerling, M. Berst, D. Gutknecht and R. Henck, Encapsulated Ge detectors: development and first tests, *Nucl. Inst. & Meth. in Phys. Res.*, vol. A369, p. 135, 1996.
- [Ell76] H. W. Ellis, R. Y. Pai, E. W. McDaniel, E. A. Mason and L. A. Viehland, Transport properties of gaseous ions over a wide energy range, *Atomic Data and Nuclear Data Tables*, vol. 17, p. 177, 1976.
- [Ell78] H. W. Ellis, E. W. McDaniel, D. L. Albritton, L. A. Viehland, S. L. Lin and E. A. Mason, Transport properties of gaseous ions over a wide energy range Part II, *Atomic Data and Nuclear Data Tables*, vol. 22, p. 197, 1978.
- [Ell84] H. W. Ellis, M. G. Thackston, E. W. McDaniel and E. A. Mason, Transport properties of gaseous ions over a wide energy range Part III, *Atomic Data and Nuclear Data Tables*, vol. 31, p. 113, 1984.
- [Emh99] S. Emhofer, *Aufbau und Vermessung der HF-Eigenschaften des REX-ISOLDE-IH-Beschleunigers*, Master's thesis, Ludwig-Maximilians-Universität München, Dec. 1999.
- [Ess] H. Essel, N. Kurz et al., The GSI Multi Branch System.
URL <http://www-gsi-vms.gsi.de/daq/home.html>
- [Fri91] J. Friedrich et al., Properties of the GSI HLI-RFQ structure, *Proceedings of the IEEE PAC 1991*, p. 3044, 1991.
- [FW94] D. Forkel-Wirth et al., Energetic radioactive ion beam studies of hydrogen in semiconductors, CERN/ISC 94-27/I13, 1994.
- [Gha96] A. M. Ghalambor Dezfuli, R. B. Moore and P. Varfalvy, A compact 65 keV stable ion gun for radioactive beam experiments., *Nucl. Inst. & Meth. in Phys. Res.*, vol. A368, p. 611, 1996.
- [Gla97] T. Glasmacher et al., Collectivity in ^{44}S , *Phys. Lett. B*, vol. 395, p. 163, 1997.

- [Hab97] D. Habs et al., The REX–ISOLDE Project, *Nucl. Phys. A*, vol. 616, p. 29c, 1997.
- [Hab00] D. Habs et al., The REX–ISOLDE Project, *Hyp. Int.*, vol. 129, p. 43, 2000.
- [Ibb98] R. Ibbotson et al., Quadrupole Collectivity in $^{32,34,36,38}\text{Si}$ and the $N = 20$ Shell Closure, *Phys. Rev. Lett.*, vol. 80, p. 2081, 1998.
- [Kei97] B. Keil, *Untersuchung der Resonatoreigenschaften des REX–ISOLDE IH–Struktur Modells*, Master’s thesis, Ludwig–Maximilians–Universität München, 1997.
- [Kle92] C.-M. Kleffner et al., The RFQ–accelerator for the high current injector of the TSR, *Proceedings of the EPAC 1992*, p. 1340, 1992.
- [Koh99] A. Kohl, *Direkte Massenbestimmung in der Bleigegend und Untersuchung eines Starkeffekts in der Penningfalle*, Ph.D. thesis, Universität Heidelberg, 1999.
- [Kön95] M. König, G. Bollen, H.-J. Kluge, T. Otto and J. Szerypo, Quadrupole excitation of stored ion motion at the true cyclotron frequency, *Int. J. Mass Spectrom. Ion Processes*, vol. 142, p. 95, 1995.
- [Kre92a] M. Kretzschmar, Single Particle Motion in a Penning Trap, *Phys. Scripta*, vol. 46, p. 544, 1992.
- [Kre92b] M. Kretzschmar, Excitation of Particle Motions in a Penning Trap, *Phys. Scripta*, vol. 46, p. 555, 1992.
- [Kug00] E. Kugler, The ISOLDE facility, *Hyp. Int.*, vol. 129, p. 23, 2000.
- [Kug01] E. Kugler, 2001, private communication.
- [MK94] T. Mayer-Kuckuk, *Kernphysik*, B.G. Teubner, Stuttgart, 1994.
- [Mot95] T. Motobayashi et al., Large deformation of the very neutron–rich nucleus ^{32}Mg from intermediate–energy Coulomb excitation, *Phys. Lett. B*, vol. 346, p. 9, 1995.
- [Nie49] A. O. Nier, T. R. Roberts and F. J. Franklin, A Double Focusing Mass Spectrometer, *Phys. Rev.*, vol. 75, p. 346, 1949.
- [Obe93] H. Oberhummer, *Kerne und Sterne*, Verlag Johann Ambrosius Barth, Leipzig, 1993.
- [Pod98] H. Podlech, M. Grieser, R. von Hahn, S. Papureanu, R. Repnow and D. Schwalm, The 7–gap–resonator–accelerator for the REX–ISOLDE–experiment at CERN, *Nucl. Inst. & Meth. in Phys. Res.*, vol. B139, 1998.

- [Pod99a] H. Podlech, *Entwicklung eines 7-Spalt Resonatorbeschleunigers für das REX-ISOLDE Projekt am CERN*, Ph.D. thesis, University of Heidelberg, 1999.
- [Pod99b] H. Podlech, M. Grieser, R. von Hahn, R. Repnow and D. Schwalm, The 7-gap-resonator-accelerator for the REX-ISOLDE-linac, in I. A. Luccio and W. MacKey, eds., *Proceedings of the 1999 Particle Accelerator Conference*, vol. 5, p. 3543, 1999.
- [Pri99] B. Pritychenko et al., Role of intruder configurations in $^{26,28}\text{Ne}$ and $^{30,32}\text{Mg}$, *Phys. Lett. B*, vol. 461, p. 322, 1999.
- [PRO] Homepage of PROFIBUS International.
URL <http://www.profibus.com/>
- [REX94] Proposal to the ISOLDE scientific committee: Radioactive beam EXperiment at ISOLDE: Coulomb excitation and neutron transfer reactions of exotic nuclei, CERN/ISC 94-25/P68, Nov. 1994.
- [RNB00] Radioactive Nuclear Beam Facilities, *NuPECC Report*, Apr. 2000.
- [Sch96] H. Scheit et al., New Region of Deformation: The Neutron-Rich Sulfur Isotopes, *Phys. Rev. Lett.*, vol. 77, p. 3967, 1996.
- [Sch01] P. Schmidt, *REXTRAP — Ion Accumulation, Cooling and Bunching for REX-ISOLDE*, Ph.D. thesis, Johannes Gutenberg-Universität Mainz, 2001.
- [Sel91] P. J. Sellin, P. J. Woods, D. Branford, T. Davinson, N. J. Davis, D. G. Ireland, K. Livingston, R. D. Page, A. C. Shotter, S. Hofmann and A. N. James, A strip detector system for proton radioactivity studies on the Daresbury recoil separator, in I. I. K. and Y. Suzuki, eds., *Proceedings of the International Symposium on Structure and Reactions of Unstable Nuclei, Niigata, Japan*, p. 70, World Scientific, Singapore, 1991.
- [Sie01] T. Sieber, *Entwicklung von 4-rod und IH-Radiofrequenz-Quadrupol-(RFQ)-Beschleuniger für radioaktive Ionenstrahlen bei REX-ISOLDE und MAFF*, Ph.D. thesis, Ludwig-Maximilians-Universität München, May 2001.
- [Vie95] L. A. Viehland and E. A. Mason, Transport properties of gaseous ions over a wide energy range Part IV, *Atomic Data and Nuclear Data Tables*, vol. 60, p. 37, 1995.
- [Wei00] L. Weissman, F. Ames, J. Äystö, O. Forstner, S. Rinta-Antila and P. Schmidt, Feasibility of in-trap conversion electron spectroscopy., *Hyp. Int.*, 2000, submitted for publication.

-
- [Wen01] F. Wenander, *REXEBIS, an Electron Beam Ion Source for the REX-ISOLDE project*, Ph.D. thesis, Chalmers University of Technology, Sweden, 2001.
- [Wie94] M. Wiescher, F. K. Thielemann, K. L. Kratz et al., Letter of Intent to the ISOLDE scientific committee: A radioactive-ion beam experiment for the study of the astrophysical rp-process at CERN-ISOLDE, CERN/ISC 94-21/I11, 1994.
- [Wol87] H. Wollnik, J. Brezina and M. Berz, GIOS-BEAMTRACE — A program package to determine optical properties of intense ion beams, *Nucl. Inst. & Meth. in Phys. Res.*, vol. A258, p. 408, 1987.
- [Wol93] Wollersheim, *GSI Report*, vol. 93-22, 1993.
- [Woo92] J. L. Wood, K. Heyde, W. Nazarewicz, M. Huyse and P. van Duppen, Coexistence in even-mass nuclei, *Phys. Rep.*, vol. 215, p. 101, 1992.

Acknowledgements

At this point I want to thank all the people who helped me in successfully managing this thesis.

My sincere thanks go to my supervisor Heinz Oberhummer, my first CERN supervisor Georg Bollen and my second CERN supervisor Juha Äystö who found a project giving me the opportunity to prepare this thesis at ISOLDE.

Special thanks go to my colleagues from REX–ISOLDE Friedhelm Ames, Oliver Kester, Pit Schmidt and Fredrik Wenander for their help and for their willingness to discuss every problem or question which arose.

My thanks go to all the collaborators of ISOLDE, which are far too many to give a comprehensive list, for their friendship and for the nice atmosphere which helped me overcome the fact of being away from friends at home.

Moreover, I want to thank Claire Fynbo for reading this thesis and correcting most of the spelling and grammar errors I made.

I owe my thanks to my parents, who supported me in the best possible ways, for encouraging me on my way through life.

August 2001

Oliver Forstner

Curriculum Vitae

Dipl.–Ing. Oliver Forstner
geb. 20.06.1973 in Wien / Österreich

Schulbildung:

1979–1983 Volksschule Wittelsbachstrasse, Wien II

1983–1987 Gymnasium Radetzkystrasse, Wien III

1987–1992 Besuch der Höheren Technischen Lehranstalt TGM, Wien XX. Absolvierung der Ausbildung zum Kunststofftechniker.

1992 Erlangung der Hochschulreife

Studium:

1992–1998 Studium der Technischen Physik an der Technischen Universität Wien

1997–1998 Diplomarbeit am Institut für Kernphysik, TU–Wien, Thema: “Protoneneinfang von Kernen im rp–Prozeß”

Juni 1998 Erlangung des akademischen Grades eines Diplom Ingenieurs an der TU–Wien

seit 10/1998 Wissenschaftlicher Mitarbeiter am Europäischen Kernforschungszentrum (CERN) in Genf/Schweiz